Evolutionary Debris Modeling of LEO and Cis-Lunar Space

by

Celina Pasiecznik

HBS, University of Toronto (2020)
MSc, University of Oxford (2021)

Submitted to the Department of Aeronautics and Astronautics
in partial fulfillment of the requirements for the degree of

MASTER OF SCIENCE IN AERONAUTICS AND ASTRONAUTICS

at the

MASSACHUSETTS INSTITUTE OF TECHNOLOGY

June 2023

Authored by: Celina Pasiecznik
Department of Aeronautics and Astronautics
May 23, 2023

Certified by: Richard Linares
Rockwell International Career Development Professor
Associate Professor of Aeronautics and Astronautics
Thesis Supervisor

Accepted by: Jonathan P. How
R. C. Maclaurin Professor of Aeronautics and Astronautics
Chair, Graduate Program Committee

Evolutionary Debris Modeling of LEO and Cis-Lunar Space

by

Celina Pasiecznik

Submitted to the Department of Aeronautics and Astronautics
on May 23, 2023, in partial fulfillment of the
requirements for the degree of
MASTER OF SCIENCE IN AERONAUTICS AND ASTRONAUTICS

Abstract

Space debris can be detrimental to missions in any orbital regime. With the advent of large satellite constellations in Low Earth Orbit (LEO) and planned return missions to the Moon, the risk created by fragmentation events in both LEO and cis-lunar space motivates an analysis of space debris evolution in these regions. Source-sink models allow for the study of debris evolution by considering various sources and sinks of debris, including atmospheric drag and fragmentation events. In this thesis, the evolution of the LEO environment is studied using a source-sink model with a variety of launch cases, including static and dynamic launch rates. A dynamical systems analysis is applied to the model to assess the stability of the LEO environment, finding stable equilibrium points for certain launch rates. Additionally, perturbations to the equilibrium state of the source-sink model are studied to determine the population of objects that trigger Kessler syndrome, and a new measure for orbital capacity is proposed. A calibrated explosion model is implemented in the source-sink model and an improved post-mission disposal model for satellites and rocket bodies is proposed. Possible improvements and current limitations of the source-sink model are explored, and the model's predictions are validated against ESA's DELTA model using 200 year-long simulations with a No-Further-Launch Case and an extrapolated launch case. The fragmentation analysis of orbiting objects that was conducted for the LEO environment is extended to a case study in cis-lunar space. The explosion model is implemented for a spacecraft in a Near-Rectilinear Halo Orbit around the Moon. The evolution of debris is studied in the Circular-Restricted Three-Body Problem, providing insight into the danger space debris poses to future missions.

Thesis Supervisor: Richard Linares
Title: Rockwell International Career Development Professor
Associate Professor of Aeronautics and Astronautics

Acknowledgments

I would like to thank my family for their unwavering support. Thank you to my mom Sylvia, my dad Eugene and my twin sister Julia for always being there for me. I also wish to thank Guillem and my friends for making this masters so memorable.

Special thanks to the MIT community and my colleagues in ARClab for their support, especially Daniel Jang, Andrea D'Ambrosio, Pablo Machuca and Thomas Roberts. I would like to sincerely thank Professor Richard Linares for his guidance and support during my masters degree. I am also grateful to my research collaborators at ESA in the European Space Operations Center with whom I had the honor of working with.

Contents

List of Figures

List of Tables

Chapter 1

Introduction

Space Debris Definition: "All human made objects including fragments and elements thereof, in Earth orbit or re-entering the atmosphere, that are non functional" [1].

1.1 Motivation

The amount of debris in orbit continues to increase leading to a greater density of non-functional objects that pose a threat to current and future space missions. The evolution of the amount of orbital debris over time is shown in Figure 1-1. Over the years, numerous research efforts have attempted to tackle the issue of accurately modeling the evolution of space debris and estimating future debris populations. The number of satellites launched into orbit over the past 2 years is historically unprecedented due to the advent of mega-constellations. The increased congestion in LEO causes satellite operators to perform collision avoidance maneuvers at much higher rates, which in turn takes away time and fuel that could have been allocated towards the mission. Moreover, planned return missions to the lunar surface in the near-future, means the analysis of fragmentation events in cis-lunar space is more critical than ever. Fragmentation events in cis-lunar space can have detrimental effects on other orbital regions. Thus, an analysis of the creation, dispersion, and evolution of debris fragments in regions beyond GEO is critical. Overall, launches and missions in LEO and cis-lunar space will be more numerous in the coming decades..

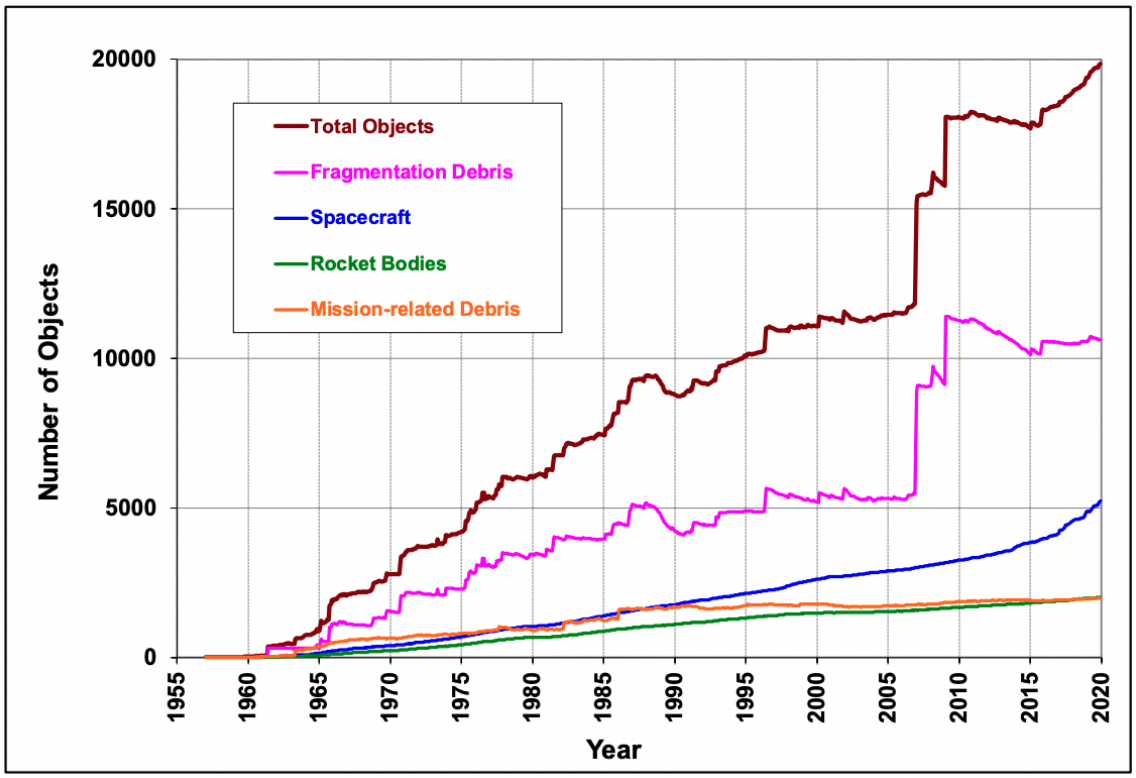

Figure 1-1: Evolution of orbital debris by object type [49]

In response to these planned activities, the demand for a debris analysis of LEO and cis-lunar space motivated the work of this thesis.

1.1.1 Fragmentation Events

Fragmentation events are the main source of debris generation. The two types of fragmentation events are collision events and explosion events. Figure 1-2 shows the predicted trends in fragmentation events for various causes including explosions and collisions. Collisions between spacecraft or between spacecraft and debris fragments can generate copious amounts of new debris. For instance, the accidental collision between Iridium 33, a U.S. operational communications satellite, and Cosmos 2251, a Russian decommissioned communications satellite that occurred on February 10th 2009 created, as of June 2012, at least 2200 trackable debris fragments [33]. This accidental collision occurred in a region that had a higher density of orbiting objects

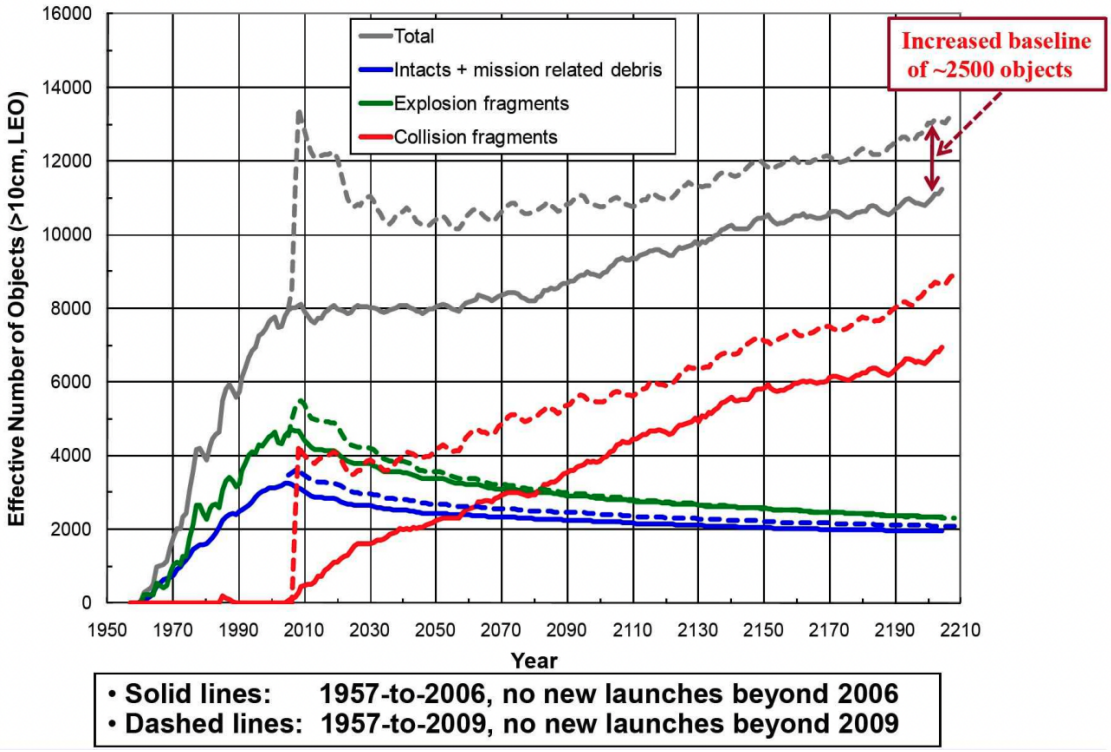

Figure 1-2: Projected number of objects caused by various debris generating mechanisms for no future launches as predicted by LEGEND, a space debris model [43].

with a higher probability of collision events[42]. The collision occurred at an altitude of 790 km creating debris fragments that will affect space missions for decades [13]. Intentional collision events have also occurred as a result of anti-satellite weapon system testing such as the ballistic missile launched by China on January 11^{th} hitting its own decommissioned meteorological satellite system, the Fengyun 1 (FY-1), and creating over 3000 debris fragments [62]. To help mitigate such fragmentation events, the Inter-Agency Space Debris Coordination Committee (IADC) publishes recommendations for preventing on-orbit collisions to minimize the number of fragments produced in accidental collisions [1].

Explosion events, such as due to residual propellant leaks from rocket bodies or battery explosions, have also created large amounts of debris. For instance, the accidental explosion of the STEP 2 Rocket Body produced over 750 trackable debris at an altitude of 625 km [4]. Many explosions are caused by residual fuel left on board a satellite or rocket body stage. The most numerous types of fragmentation events have been due to propulsion systems causing accidental explosions [18]. To prevent such explosions, the IADC guidelines state that all remaining energy stored on a spacecraft or rocket body should be depleted; this process is referred to as 'passivation' [63]. Electrical failures, such as due to overcharged batteries, can also lead to explosions making up 6.4% of the historical fragmentation events [18]. The IADC also published recommendations for minimizing the potential of on-orbit break-up events during mission operations and after the end of the mission [1]. Such guidelines need to be adopted by satellite operating agencies to ensure the long-term sustainability of the orbital environment.

1.1.2 Risk to Space Missions

With increased congestion in LEO, satellites have had to make an unprecedented number of collision avoidance maneuvers, using up time that could be spent on the mission's objective. For instance, a collision avoidance maneuver performed by CryoSat in July 2018, caused the polar ice-monitoring satellite to be raised to an altitude where it could not satisfy its scientific goals without a second maneuver that placed

it back into its optimal orbit [50]. Moreover, the mega-constellation Starlink has had to make thousands of avoidance maneuvers within a two-year period from 2020 to 2022 [2]. Collision avoidance maneuvers are performed to keep the risk of collision very low. As more satellites are launched, accurate collision detection systems and debris modeling are necessary to minimize the number of collisions in orbit.

Additionally, the growing amount of debris in LEO is becoming an increasing concern for human spaceflight missions. For example, in November 2021, astronauts and cosmonauts aboard the International Space Station had to take extra precautions and remain inside their capsules due to a close encounter with passing space debris [54]. Earlier that year, on May 12^{th} 2021, high-velocity debris created a hole in the Canadarm2 robotic arm that is attached to the International Space Station but did not cause any significant damage to its operations [40]. The number of such debris collisions with the International Space Station is expected to increase over the next decade, posing a risk to humans and science missions on board.

Furthermore, debris that can reach the lunar surface from fragmentation events in cis-lunar orbits also poses a risk to space missions. Impacts on the lunar surface can create ejecta of regolith from the lunar surface that can pose a threat to lunar operations, including to the lives of astronauts [16]. Thus, any debris in cis-lunar space that has a chance of impacting the Moon can be a threat to lunar operations. Impacts from lunar orbital debris to the lunar surface are important to study in order to set mitigation guidelines [3, 23]. For example, disposal strategies in cis-lunar space need to be studied to ensure a successful post-mission disposal is achieved for future missions, as done in [22]. Overall, understanding the evolution of space debris in areas of high congestion or high risk is a key step to determining sustainable practices and guidelines for the space community.

1.2 Thesis Outline

This thesis presents a space debris analysis of LEO with a case study of debris evolution in cis-lunar space. The motivation for the work of the thesis was given in

this chapter. Chapter 2 provides the background on evolutionary models and debris analysis required for the remainder of the thesis. Chapter 3 provides a dynamical systems analysis of the effects of various launch rate distributions using a source-sink evolutionary debris model. Chapter 4 covers improvements made to MIT's source-sink evolutionary model and presents simulations used in validating the model against other debris models. Chapter 5 explores a case study of cis-lunar space debris evolution. Chapter 6 summarizes the findings of the thesis and provides some avenues for future research.

Chapter 2

Background

2.1 Space Debris Models

Debris models describe the current debris environment and allow for predictions of the future orbital environment. These models help researchers make risk assessments for debris and evaluate mitigation practices. There are two main types of evolutionary debris models found in the literature: Monte-Carlo (MC) based models and source-sink or Particle-in-a-Box models. MC evolutionary models propagate individual Resonant Space Objects (RSOs) requiring a high computational cost. MC models are considered higher fidelity models since they also incorporate dynamics such as perturbation effects and space weather. Examples of Monte-Carlo evolutionary models include: LEGEND [44], ADEPT [29], DAMAGE [39] and DELTA [60]. These evolutionary debris models have been used to analyze the effects of various mitigation measures [61, 45].

Source-sink or Particle-in-a-Box models categorize RSOs into species and simulate the space environment using various sources and sinks. This methodology allows for fast computations of simulations with different initial conditions and scenario properties. Various analytic models of the orbital environment have been proposed in the literature that make use of differential equations to represent the evolution of the number of objects in space and their interactions. Such models are given in works by Lewis et al. [38], Kebschull et al. [32], Trozzi et al. [58], and Rossi et al. [53].

Some of these models have also been used to test the LEO environment's sensitivity to run-away debris growth. This run-away debris growth is known as Kessler syndrome wherein the congestion of the orbital environment is large enough to cause a chain reaction of debris generation. To study such debris growth caused by collisions, Kessler and Cour-Palais developed a source-sink model to predict detrimental debris population growth [34]. Furthermore, Talent [57] used one ordinary differential equation (ODE) to represent the total number of objects in space and studied various evolutionary cases for different launch rates to look for catastrophic behavior. Zhang et al. [65] developed a model using partial differential equations and solved the equations numerically to study the long-term evolution of the space debris environment. A dynamical systems analysis was conducted by Drmola and Hubik [14] in which three different classes of debris were used to study various debris accumulation scenarios and whether they lead to Kessler syndrome.

MIT's Orbital Capacity Assessment Tool (MOCAT) is a space debris evolutionary model developed by the Astrodynamics, space Robotics, and Controls Lab (ARClab) at MIT. Two versions of the model are the MC-based approach referred to as MOCAT-MC and the probabilistic source-sink model approach referred to as MOCAT-SSEM. MIT's Orbital Capacity Assessment Tool - Source-Sink Evolutionary Model, or MOCAT-SSEM, has been used to make predictions about the future Low Earth Orbit (LEO) environment using a capacity analysis [15, 11, 10] and a dynamical systems analysis [48, 27]. The next section provides a more detailed overview of the source-sink model used in the thesis analysis.

2.2 MOCAT-SSEM

2.2.1 MOCAT-3

The MOCAT-3 model was developed in reference [11]. Reference [15] contains a detailed description of each model parameter and all model assumptions for MOCAT-4N, a 4-species model, that hold for MOCAT-3. The MOCAT-3 model has been used

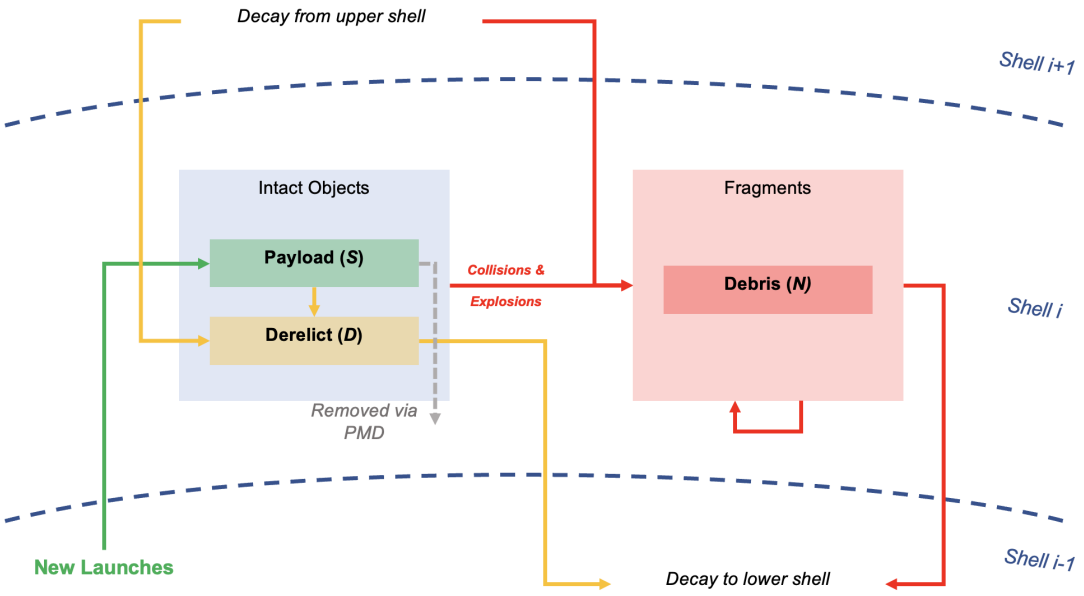

Figure 2-1: A depiction of the species interactions and dynamics in the MOCAT-3 model.

to calculate the risk-based capacity of LEO [11]. The model was extended to include a differentiation between slotted and unslotted satellites which made use of the intrinsic capacity of LEO as a constraint on the optimal launch rate for the risk-based capacity estimate [41]. Here a brief overview of the model depicted in Figure 2-1 is provided along with the key equations describing the evolution of each species.

Model Parameters and Equations

MOCAT-3 is a source-sink model with three species: active satellites (S), derelict satellites (D), and debris (N). Active satellites are objects that are able to perform collision avoidance maneuvers and maintain their current orbits in the presence of drag. Derelict objects are active satellites that have reached their end-of-life and can no longer maneuver. Debris objects are smaller fragments such as those produced in collisions. The orbital environment within the altitude range of 200-900 km is divided into 20 spherical orbital shells with a shell thickness of 35 km, represented by the variable d. The evolution of each species is represented by a set of differential equations per shell $\{\dot{S}(h),\ \dot{D}(h),\ \dot{N}(h)\}$, where h is a value from 1 to 20 indicating the shell number. Shell $h = 1$ is the lowest shell for the altitude range 200-235 km

Table 2.1: MOCAT-3 equation terms per species.

	Species	S	D	N
$\dot{\Lambda}$	-	λ_S	0	0
$\dot{C}_{PMD}$	-	$-\frac{S}{\Delta t}$	$\frac{(1-P_m)}{\Delta t}S$	0
$\dot{F}$	-	0	$\dot{F}_{d,D}$	$\dot{F}_{d,N}$
$\dot{C}$	S	$-\alpha_a \phi_{S,S} S^2$	$\phi_{S,D}\delta DS$ $+\phi_{S,N}\delta NS$	$n_{f,SS}\alpha_a\phi_{S,S}S^2$ $+n_{f,SD}\phi_{S,D}\alpha SD$ $+n_{f,SN}\phi_{S,N}\alpha SN$
	D	$-\phi_{S,D}(\delta+\alpha)SD$	$-\phi_{D,D}D^2$	$n_{f,DD}\phi_{D,D}D^2$ $+n_{f,DN}\phi_{D,N}DN$
	N	$-\phi_{S,N}(\delta+\alpha)SN$	$-\phi_{D,N}DN$	$+n_{f,NN}\phi_{N,N}N^2$

and shell $h = 20$ is the highest shell for the altitude range 865-900 km. Each object is assumed to have a near-circular orbit. The launch rate per year is represented by $\lambda(h)$ and only appears as a source for S. New active satellites appear instantly in their orbital shell h and do not cross through lower shells. Dropping the explicit dependence on shell number and time, each species population $P = \{S, D, N\}$ evolves according to the equation:

$$\dot{P} = \dot{\Lambda} + \dot{C}_{PMD} + \dot{C} + \dot{F} \tag{2.1}$$

where the species-dependent components are shown in Table 2.1. Active satellites S can become derelict D or debris N through collisions but no species can become an active satellite S for which the only source is λ. Furthermore, active satellites directly exit the environment at a rate of $1/\Delta t$ with a success probability of P, the rest becoming derelict satellites. The lifetime of each active satellite is taken as $\Delta t = 5$ years, whereas the probability of successful Post-Mission Disposal (PMD) is $P = 0.95$.

Drag Flux

The drag effects are represented by

$$\dot{F}_{d,Q} = -\frac{Q_+ v_+}{d} + \frac{Qv}{d} \tag{2.2}$$

where Q is the species and the change in the semi-major axis due to drag is $v = -\rho B_c \sqrt{\mu R}$. Here B_c is the ballistic coefficient that depends on the species' area to mass ration since $B_c = c_D \frac{A}{m}$. In this analysis, the drag coefficient is $c_D = 2.2$. Here Q_+ refers to the species population in the shell directly above the current shell, namely $Q_+ = Q(h+1)$. For the highest shells, this parameter is taken to represent the current shell $Q_+ = Q(h)$ for reasons given in Section 3.2. According to our assumptions, once an object is in orbit it can only move into lower altitude shells and not into higher shells as orbit-raising maneuvers into higher shells are not considered. The natural de-orbiting of objects from higher shells to lower shells is dictated by a static exponential model for the atmospheric density described in reference [11]. Only derelict and debris objects are assumed to de-orbit from atmospheric drag effects as active satellites are assumed to have station-keeping capabilities that counter-act these drag effects.

Collisions

The number of fragments created during collisions between the species is determined by the NASA standard break-up model [37] which gives:

$$n_f = \begin{cases} 0.1 L_C^{-1.71} \left(M_i + M_j\right)^{0.75} & \text{catastrophic} \\ 0.1 L_C^{-1.71} \left(M_p \cdot v_{imp}^2\right)^{0.75} & \text{non-catastrophic} \end{cases} \tag{2.3}$$

where M_i and M_j are the masses of the two species colliding and $M_p = \min\left(M_i, M_j\right)$. The impact velocity is assumed to be $v_{imp} = 10$ km/s and the characteristic length of the smallest size of debris is $L_C = 0.1$ m. The probability of collision between two objects i and j is:

$$\phi_{i,j} = \pi \frac{v_{imp} \sigma_{i,j}}{V(h)} \tag{2.4}$$

where $V(h)$ is the volume of shell h and the impact parameter is given with respect to the objects' radii r as $\sigma_{i,j} = (r_i + r_j)^2$. For the collision model, the average mass, area, and diameter values used for each species were taken from reference [55], and are shown in Table 2.3. The variables δ, α, α_a set the proportionality of collisions that create debris objects. Specifically, $\delta = 10$ gives the ratio of collisions that produce disabling versus lethal debris, $\alpha = 0.2$ is the fraction of derelict and debris objects that an active satellite fails to avoid, and $\alpha_a = 0.01$ is the fraction of active satellites that another active satellite fails to avoid. This completes an overview of the MOCAT-3 model.

2.2.2 MOCAT-4B

The MOCAT-4B Model is a 4-species model as proposed in [25]. The 4 species considered are: active satellites (S), derelict satellites (D), debris (N), and rocket bodies. All of the assumptions used in the MOCAT-3 model hold for MOCAT-4B and the characteristics of the active, derelict, and debris species are unchanged. The new species of rocket bodies has its own collision probability with the other species and is affected by atmospheric drag forces. The species characteristics for rocket bodies are given in Table 2.3. Differing from the proposed model in reference [25], this thesis considers a launch rate for rocket bodies as well as a probability of successful post-mission disposal. MOCAT-4B is schematically shown in Figure 2-2. Each species population $P = \{S, D, N, B\}$ evolves again according to the equation 2.1 and the species-dependent components are shown in Table 2.2.

2.3 Launch Analysis

The unprecedented launch rate of satellites in LEO can have severe consequences on the stability of the orbital environment for decades to come. In the 200-900 km altitude range alone, the number of satellites launched per year has increased over the last decade as shown in Figure 2-3. Companies such as Amazon and SpaceX, have announced plans to launch constellations of thousands of satellites into LEO over the

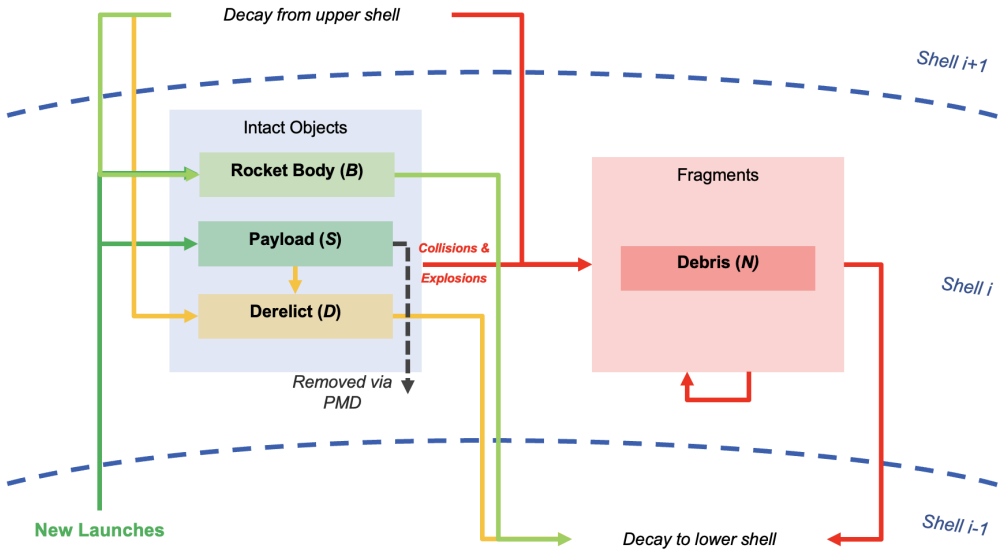

Figure 2-2: A depiction of the species interactions and dynamics in the MOCAT-4B model.

Table 2.2: MOCAT-4B equation terms per species.

	Species	S	D	N	B
$\dot{\Lambda}$	-	λ_S	0	0	λ_B
$\dot{C}_{PMD}$	-	$-\frac{S}{\Delta t}$	$\frac{(1-P_m)}{\Delta t}S$	0	$-P_m B$
$\dot{F}$	-	0	$\dot{F}_{d,D}$	$\dot{F}_{d,N}$	$\dot{F}_{d,B}$
$\dot{C}$	S	$-\alpha_a \phi_{S,S} S^2$	$\phi_{S,D}\delta DS$ $+\phi_{S,N}\delta NS$ $+\phi_{S,B}BS$	$n_{f,SS}\alpha_a\phi_{S,S}S^2$ $+n_{f,SD}\phi_{S,D}\alpha SD$ $+n_{f,SN}\phi_{S,N}\alpha SN$ $+n_{f,SB}\phi_{S,B}\alpha SB$	$-\phi_{S,B}\alpha\frac{B^2 S}{B+S}$
	D	$-\phi_{S,D}(\delta+\alpha)SD$	$-\phi_{D,D}D^2$	$n_{f,DD}\phi_{D,D}D^2$ $+n_{f,DN}\phi_{D,N}DN$ $+n_{f,DB}\phi_{D,B}DB$	$-\phi_{D,B}BD$
	N	$-\phi_{S,N}(\delta+\alpha)SN$	$-\phi_{D,N}DN$	$+n_{f,NN}\phi_{N,N}N^2$	$-\phi_{N,B}BN$
	B	$-\phi_{S,B}\alpha\frac{S^2 B}{B+S}$	$\phi_{D,B}DB$ $+\phi_{N,B}NB$ $+\phi_{B,B}B^2$	$n_{f,NB}\phi_{N,B}NB$ $+n_{f,BB}\phi_{B,B}B^2$	$-\phi_{B,B}B^2$

Table 2.3: Physical characteristics of each species in MOCAT-4B.

	Active, S	Derelict, D	Debris, N	Rocket Body, B
Mass (kg)	223	223	0.640	1421
Area (m^2)	1.741	1.741	0.020	7.419
Diameter (m)	1.490	1.490	0.180	3.070

next decade [12] with hundreds of satellites already launched. A rising launch rate will increase orbital congestion which in turn raises the chance of debris-generating collisions. A growing debris population can have catastrophic consequences on space missions. It is important to study how increased launch activities affect the evolution of the orbital environment and the production of debris, as well as how increased debris populations affect the stability of LEO. Percent increases in launch activities have been considered in reference [57], however, recent years have seen unprecedented launch activities that exceed fixed percent increments. The response of the orbital environment to the introduction of a mega-constellation has also been analyzed in reference [60]. However, with several mega-constellations planned, it is important to analyze the effect of the introduction of multiple constellations with various launch cases.

2.4 Cis-Lunar Space Debris Analysis

Analysis of fragmentation events and debris mitigation in cis-lunar space is increasingly important as humanity looks towards a long-term presence in this region with upcoming lunar missions. Exploring the consequences of such fragmentation events includes analyzing the risk that the resulting fragments have on space exploration missions, satellite operations, and possible future lunar habitats. The trajectories of cis-lunar debris involve more complicated dynamics to account for the Earth-Moon system. Furthermore, unlike in LEO, there is no atmospheric drag effect to remove debris. Thus, researchers have been studying the evolution of cis-lunar debris to compute the long-term effects of debris and define sustainable practices for cis-lunar space debris mitigation such as in reference [21]. Studies of fragmentation events

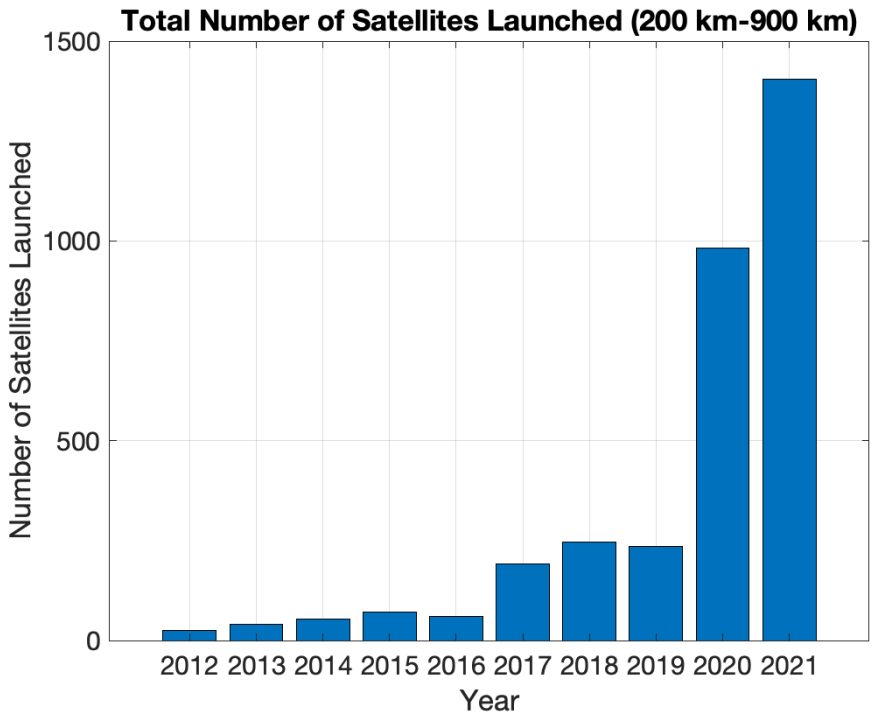

Figure 2-3: Number of objects launched to 200-900 km altitudes over the past decade [59].

in cis-lunar space have been done for specific cases and missions such as along the Apollo transfer trajectory in reference [5]. Cis-lunar situational awareness focuses on situational awareness and traffic management beyond the near-Earth region and has gained interest recently with upcoming cis-lunar missions as explored in [19]. The evolutionary debris models in cis-lunar space found in the literature, typically analyze the trajectories of debris from fragmentation events occurring on specific orbits and compute whether the fragments have impacts with Earth or the lunar surface, as done in [24]. Continued analysis of the effects of fragmentation events in cis-lunar space is important to set mitigation guidelines and decrease the chances of mission failure.

Chapter 3

Dynamical Systems Analysis of Debris in LEO

In this chapter, multiple launch rates are computed and used in the MOCAT-3 model to study the evolution of debris in LEO. Equilibrium solutions are computed for the model and perturbations to these solutions are analyzed to study the reaction of the orbital environment to increases in the debris population. A new definition of capacity based on the population of debris is given.

3.1 Launch Rate Distributions

Launch Rate Distribution Definition: The distribution across altitudes of the number of active satellites launched per year.

Several launch rate distributions were studied to analyze the stability of the LEO environment. These launch rate distributions were categorized into two types of distributions: *static* and *dynamic* launch rates. A static launch rate distribution consists of a constant yearly launch of active satellites for each altitude shell for a set number of years.

A dynamic launch rate represents a variable launch rate per year for each altitude shell. For a given launch rate distribution, a unique set of equilibrium solutions is found. Thus, a static launch rate is necessary to study the behavior of the system of

equations with respect to the equilibrium solutions. However, a dynamic launch rate represents a more realistic scenario since the number of satellites launched per year has changed drastically over the past few decades. Hence, a dynamic launch rate was studied as a separate case for which the equilibrium solutions were not computed as these changed for each year of the launch traffic.

3.1.1 Static Launch Rate

Two cases of static launch rates were studied. For the first case, the maximum number of satellites launched in one year per altitude shell over the past ten years was used. In the second case, the 'As Received' filings database from the International Communications Union (ITU) was used.

Case 1: Past Launch Rates

The maximum number of satellites launched within one year over the past ten years (2012-2022) for each altitude shell was used. The maximum historic launch rate per shell was used instead of using the launch rate from a specific year because particular years have a low number of launches to certain shells that don't represent the general behavior of the historical launch traffic. This launch rate distribution allowed for a stability analysis of the current LEO environment to see if current launch activities are sustainable or if there already is a danger of run-away debris growth. The maximum number of satellites launched into each altitude shell over the chosen decade was computed from the Union of Concerned Scientists database [59], and is displayed in Figure 3-1.

Case 2: ITU Filings

The 'As Received' ITU filings database [46], is a list of satellite notices filed with the ITU that have not yet been reviewed or published by the ITU. It should be noted that the ITU states this database is not regulated. However, this database allows for some forecasting of satellite launches over the next few years. In particular, the ITU filings

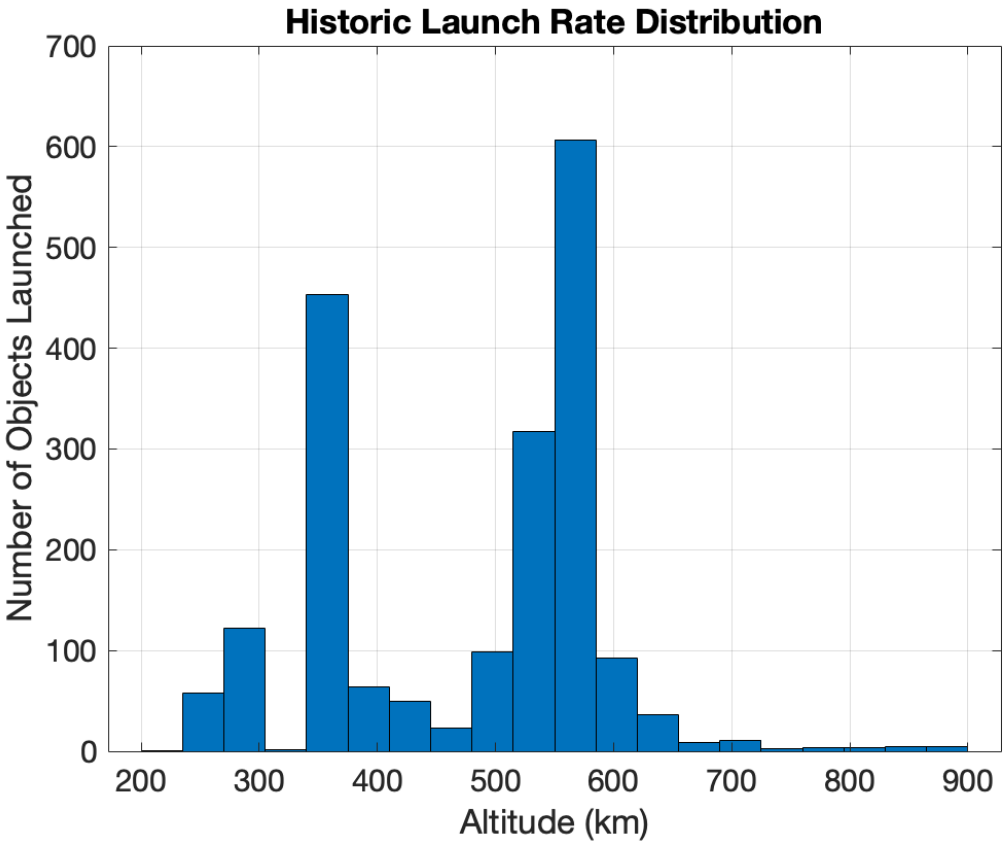

Figure 3-1: Maximum number of satellites launched within a year per altitude shell from 2011 to 2021 [59].

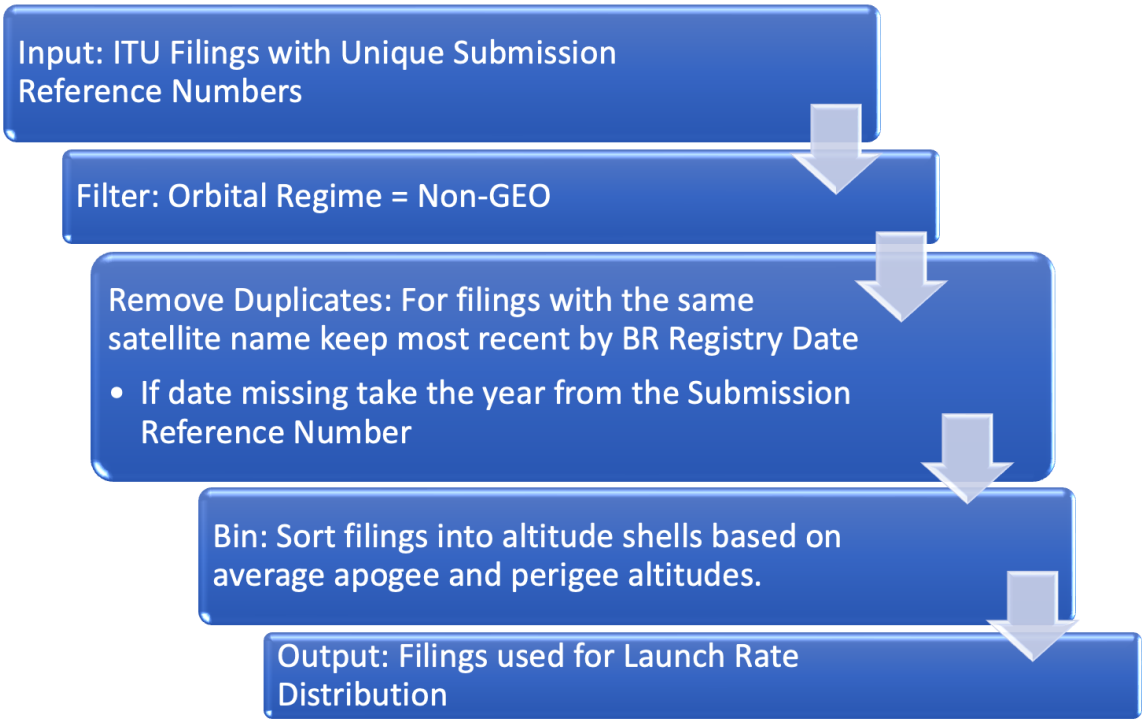

Figure 3-2: Logic for creating the launch rate distribution from the ITU 'As Received' database.

offer a depiction of which altitude shells are the most desirable by operating agencies and thus represents which altitude shells are expected to have the greatest density of objects. Each filing includes the altitude and number of satellites that an organization intends to launch. This database was filtered to eliminate duplicate filings made by the same organization. These include, for example, when an operating agency files with the submission type 'Advanced Publication Information' and then files the same constellation name and characteristics with the submission type 'Coordination Request.' The filings were processed according to the logic given in Figure 3-2. In filtering out duplicate filings, the most recent filing were retained as they were assumed to be the most accurate. Again, near-circular orbits were assumed for the binning process. The number of satellites forecast to be launched into each altitude shell is shown in Figure 3-3.

These filings are valid for several years and the deployment of a satellite or constellation of satellites into orbit can take several years. Furthermore, the total number of satellites for all LEO constellation filings in the 'As Received' ITU database is

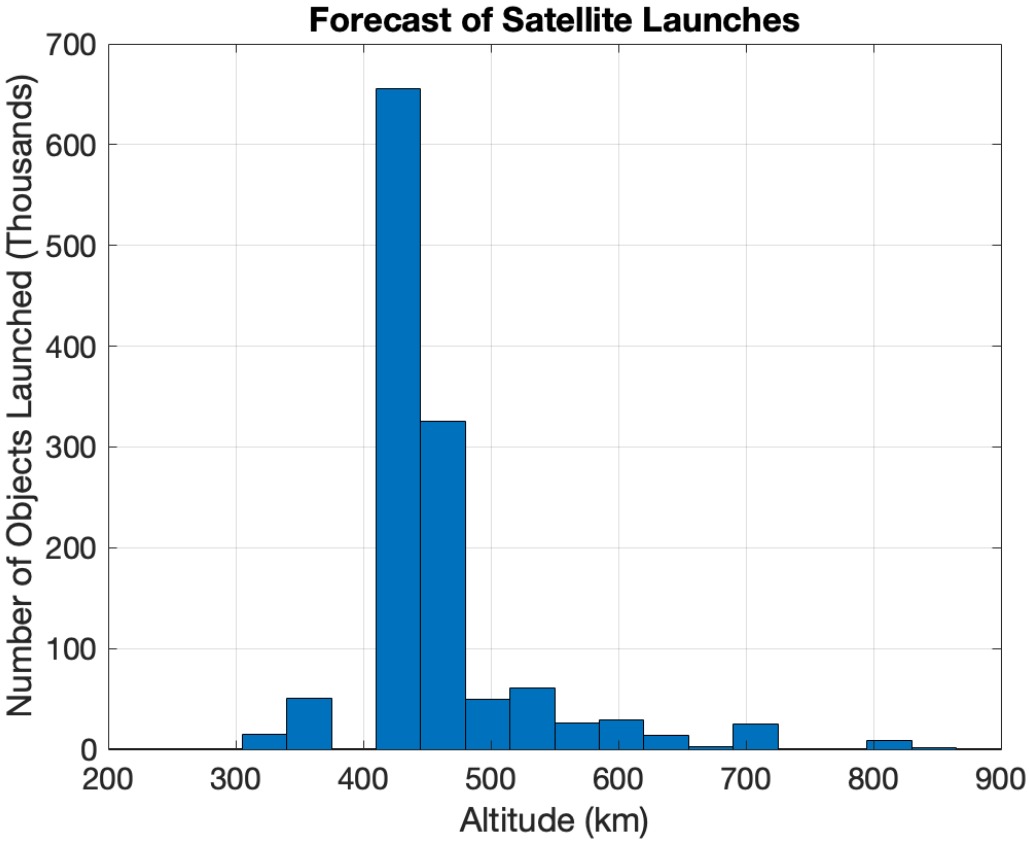

Figure 3-3: 'As Received' ITU filings of satellite notices [46].

1,264,322. Using this launch rate as an input into the source-sink model causes no equilibrium solutions to be found. However, the number of satellites launched in 2021 was a total of 1,674 according to the UCS database [59]. While it is believed the number of launches will continue to increase as more mega-constellations are deployed, only 1/6th of the number of satellites given in the ITU filings is kept as the launch traffic when conducting this analysis over the next 200 years. This factor of 1/6th is referred to as the confidence level in the ITU filings. This assumption still leads to a launch rate of 42,144 satellites per year if the deployment rate of each satellite constellation is assumed to be 5 years. As done in other studies of large constellations such as in reference [52], the lifetime of each satellite is set to 5 years and thus the replenishment rate for each satellite constellation is also set to 5 years. Overall, a fraction of the ITU filings was used to create a launch rate distribution case for future satellite constellations.

3.1.2 Dynamic Launch Rate

A dynamic launch rate was studied as a third launch rate distribution. As shown in Figure 2-3, the number of objects launched into orbit each year has not remained constant. By using a dynamic launch rate, it is possible to represent such a change in launch rate per year.

Case 3: Variable Launch Rate per Year

A similar approach as reference [57] was used in modeling a dynamic launch rate. The launch rate displayed in Figure 3-1 was taken as the base rate and then increased this launch rate by 0%,1%,3%,5%, and 7% each year for 50 years. Then the launch rate was set to be constant at the rate calculated at the end of the 50-year period. The environment was allowed evolve for another 800 years at this constant launch rate. The total number of objects per year for each incremental launch rate is displayed in Figure 3-4. The total number of launched satellites and species populations at the end of the 800 years for each incremental launch rate is given in Table 3.1. As

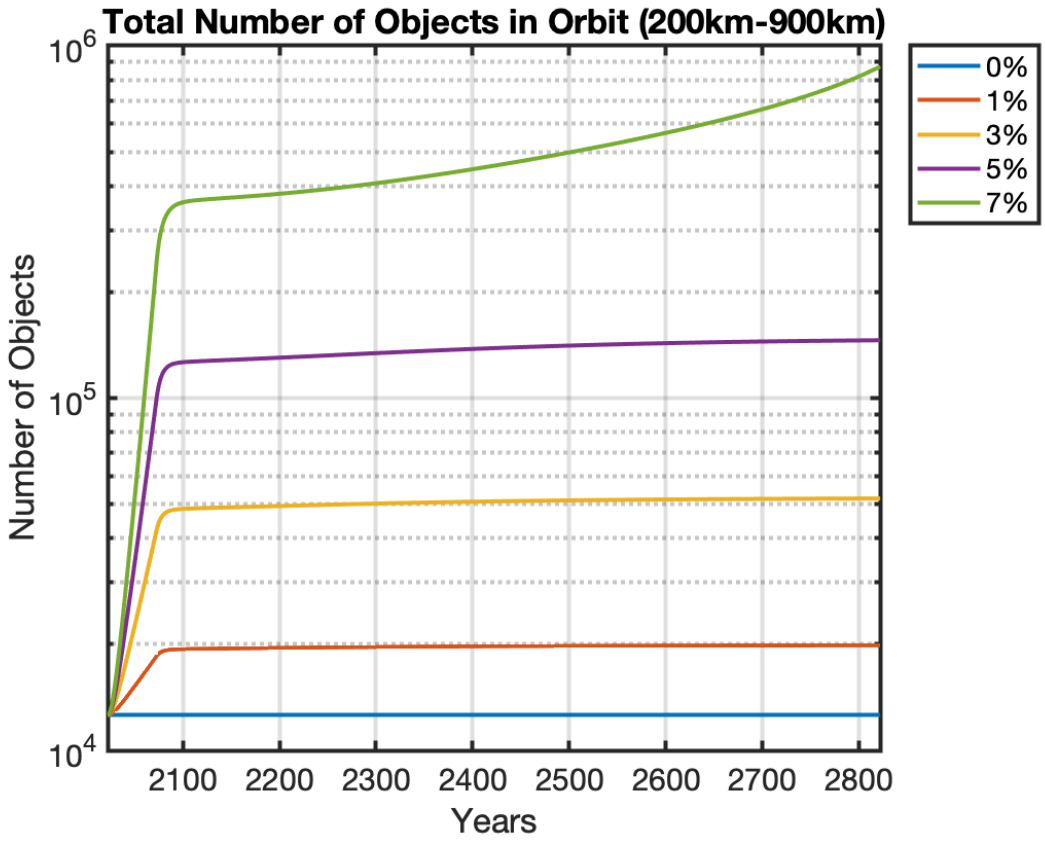

Figure 3-4: Total number of objects in orbit for launch rates growing by 0-7% per year for 50 years and then remaining constant for 800 years.

shown in the table, the various percentage increases in launch rate for the first 50 years produce a drastically different total number of objects in the environment at the end of the simulation. For example, a 7% increase in launch rate produces a total number of objects at the end of the 800-year simulation that is about two orders of magnitude larger than the total produced by a 1% increase in launch rate. This numerical analysis shows how a few percent difference in increasing launch rate per year creates large differences in the population of each species when propagated over time.

Table 3.1: Population of each species and the total number of objects in orbit at the end of a period of constant growth rate in the launch rate as shown in Figure 3-4.

%	λ	S	D	N	Total
0%	1965	9820	1383	1402	12605
1%	3232	16146	1984	1743	19873
3%	8614	42976	4621	4317	51914
5%	22533	111830	12387	22061	146270
7%	57883	270980	60571	741220	1072800

3.2 Stability Analysis

The equilibrium states for the set of coupled differential equations 2.1 were solved for each shell by finding the population of each type of species $\{S_{eq}(h), D_{eq}(h), N_{eq}(h)\}$ for which the differential equations equal zero:

$$\dot{S} = 0,\ \dot{D} = 0,\ \dot{N} = 0.$$

For this set of values $\{S_{eq}(h), D_{eq}(h), N_{eq}(h)\}$, the sources and sinks in the orbital environment balance each other and the system is in equilibrium. A change in the launch rate generates a new set of equilibrium solutions because the launch rate is a major source of the active satellite population.

Since each differential equation in 2.1 has degree 2, the set of 3 coupled equations has $2^3 = 8$ equilibrium solutions per shell. Solutions that are purely imaginary or that contain a real negative part were eliminated, as these are considered non-physical solutions for the species' populations. For the launch rate cases studied, it was found that each shell has two sets of positive, real-valued equilibrium solutions $\{S_1(h), D_1(h), N_1(h)\}$ and $\{S_2(h), D_2(h), N_2(h)\}$, with one solution set having a larger number of active satellites than the other: $S_1 > S_2$. This solution set $\{S_1(h), D_1(h), N_1(h)\}$ was used as the influx populations to the next lower shell $\{S_1(h-1), D_1(h-1), N_1(h-1)\}$. For the highest shell, it was assumed that the influx of objects from higher altitudes equaled the outflow of objects from that shell. This assumption may differ from reality as there are many objects located above 900

km but it is difficult to measure how many of these objects would de-orbit due to atmospheric drag at such high altitudes per year. By finding the equilibrium solutions $\{S, D, N\}$ per shell starting with the highest altitude shell and ending with the lowest altitude shell, the equilibrium of the entire orbital environment in the 200-900 km altitude range was guaranteed because each shell depends only on the species population within that shell and the one directly above it. This model does not contain any flows from lower shells into higher shells which signify the lower shells do not affect the equilibrium of the higher shells.

To calculate the stability of the equilibrium solutions, the Jacobian matrix was computed and the eigenvalues at equilibrium were found. An equilibrium solution set of active, derelict, and debris objects is classified as stable if the set had negative eigenvalues.

For a given launch rate and set of initial conditions $\{S_i, D_i, N_i\}$, the differential equations 2.1 were integrated with respect to time to find the number of years required for the source-sink model to reach equilibrium. The initial conditions used were based on Two Line Element data from space-track.org[1]. The process of reference [41] was used to classify each object as an active satellite, derelict satellite, or as debris according to its mass, diameter, and area. Note that unlike reference [41], slotted and unslotted satellites are not differentiated and thus these two populations are combined into the active satellite population. The initial populations of each species are displayed per altitude shell in Figure 3-5.

3.2.1 Equilibrium Solutions

For each launch rate, the set of equilibrium solutions were determined. The equilibrium solutions per shell were computed for the business as usual case 3.1.1 that was calculated from the historic launch rates; the results for which are presented in Figure 3-6. It is shown in Figure 3-13 that given the current initial population of each species, the system will evolve to an equilibrium state. Thus, if launch rates remain at these levels they could be sustainable for the 200-900 km altitude range without run-

[1]The TLE catalog was downloaded from space-track.org, accessed on August 18th, 2022.

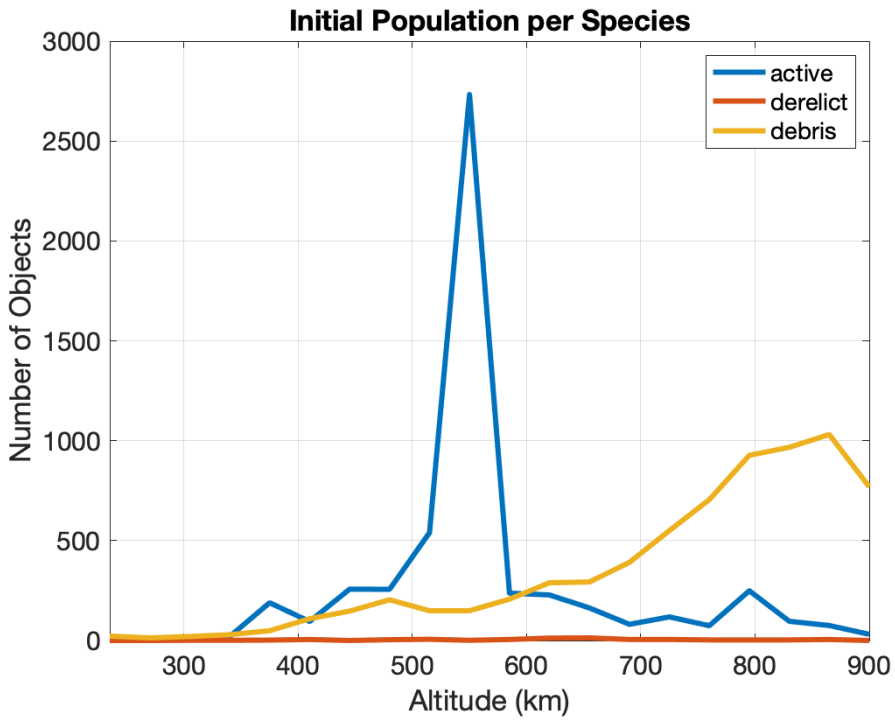

Figure 3-5: Population of each species from TLE data as of August 2022.

Table 3.2: Total population of each species at equilibrium for various launch rate distributions.

Rate	Yearly Launch λ	Total Active S	Total Derelict D	Total Debris N	Total All
Case 1	1965	9820	1383	1402	12605
Case 2	42144	209142	18138	77010	304290
Case 3: 1%	3232	16145	2292	4281	22718

away debris growth occurring. However, the simplifications of the source-sink model must be acknowledged such as the absence of rocket bodies, non-trackable debris, and explosions that could affect the evolution of the species populations.

The equilibrium solutions for Case 2 (3.1.1) were computed and a set of equilibrium points for each shell were found as shown in Figure 3-7. For the dynamic launch Case 3 (3.1.2), positive, real-valued equilibrium solutions could only be found for the 1% increase in launch rate per year. A summary of the total population of each species at equilibrium for each launch case is given in Table 3.2.

Overall, the number of active satellites S at equilibrium is proportional to the

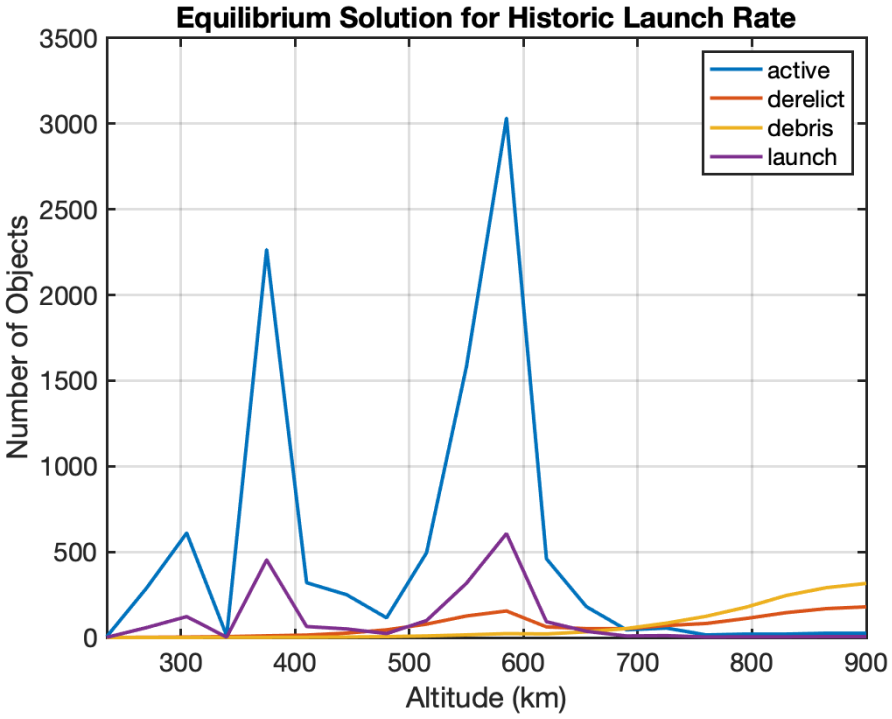

Figure 3-6: Equilibrium solutions per species for the constant launch rate Case 1 (3.1.1).

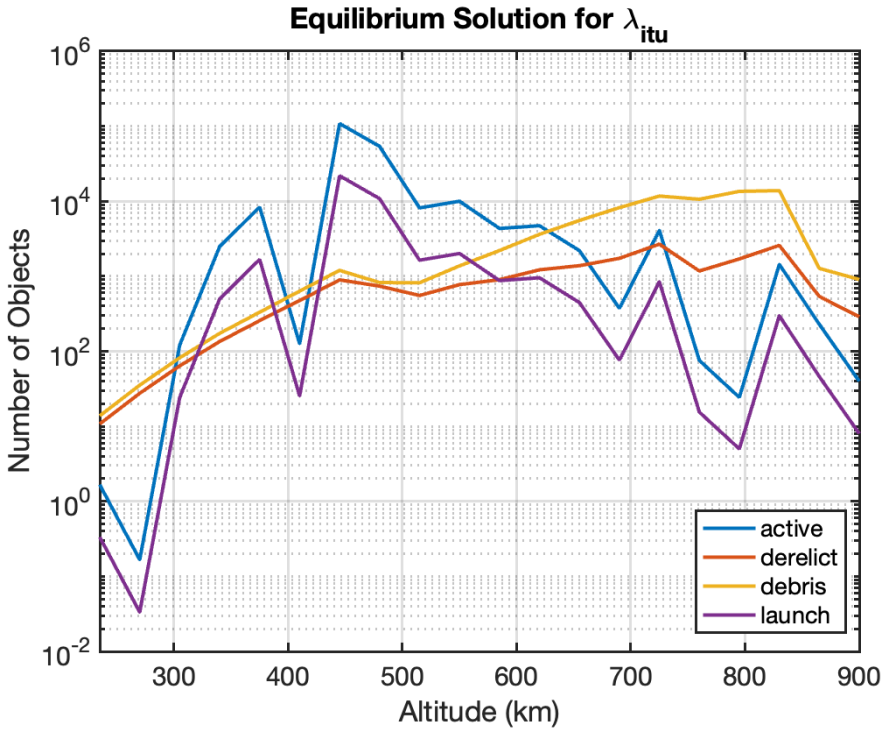

Figure 3-7: Equilibrium solutions per species for a constant launch rate proportional to ITU filings given in Case 2 (3.1.1).

number of satellites launched. The amount of debris N and derelict satellites D, however, vary with respect to the number of active satellites, with higher shells acquiring a larger number of derelict and debris objects because the sink caused by atmospheric drag removes fewer objects per year at higher altitudes due to the lower atmospheric density.

3.2.2 Basin of Attraction

Basin of Attraction Definition: "The set of points in the space of system variables such that initial conditions chosen in this set dynamically evolve to a particular attractor" [8].

In this model, an attractor is a stable equilibrium point. Once the source-sink model is at a steady equilibrium state, the model's reaction to perturbations in $\{S, D, N\}$ from equilibrium was studied. In particular, how a sudden increase in debris N alters the orbital environment was studied by looking at how the system evolved after the perturbation and whether or not it tended back toward equilibrium. The basin of attraction about the stable equilibrium point was found for various perturbations. One of the reasons this work focuses on analyzing the stability of the orbital environment with respect to changes in the species of debris rather than changes in active or derelict satellites, is the exact amount of debris currently in LEO is unknown. Another reason is to study the instability threshold for debris creation known as 'Kessler syndrome' in which the amount of debris in the orbital environment is numerous enough that it continues to generate more and more debris, creating a chain reaction. To visualize the basin of attraction, phase space diagrams were plotted.

Stability of Equilibrium Points

The stability of the equilibrium solutions found for Case 1 (3.1.1), Case 2 (3.1.1) and Case 3 (3.1.2) at 1% increment only, was determined by computing the eigenvalues of the solutions. All eigenvalues were found to be negative indicating all of these

Table 3.3: The eigenvalues of each population for the equilibrium solutions displayed in Figure 3-7.

Active S	Derelict D	Debris N
-0.200	-1.030	-0.214
-221.167	-0.593	-0.205
-885.271	-0.437	-0.205
-345.598	-0.353	-0.205
-149.086	-0.254	-0.200
-86.341	-0.088	-0.200
-37.246	-0.083	-0.202
-70.472	-0.056	-0.204
-36.782	-0.052	-0.204
-17.604	-0.001	-0.202
-19.148	-0.006	-0.200
-10.045	-0.004	-0.202
-9.182	-0.008	-0.202
-5.541	-0.016	-0.200
-4.784	-0.023	-0.202
-3.129	-0.032	-0.201
-2.414	-0.028	-0.201
-1.337	-0.028	-0.201
-0.775	-0.126	-0.201
-1.780	-0.146	-0.201

equilibrium solutions are stable. As an example, Table 3.3 displays the eigenvalues for the launch rate Case 2 (3.1.1).

Phase Portraits

Additionally, phase portraits were used to depict the phase space about the stable equilibrium point per shell. The phase portraits for the equilibrium points of the Case 1 (3.1.1) launch rate, shown in Figure 3-6, are displayed for two altitude shells in Figure 3-8.

3.2.3 Evolution Analysis

The number of years needed for the orbital environment to settle into its equilibrium state was analyzed for the launch rate Case 2 (3.1.1) assuming the initial conditions

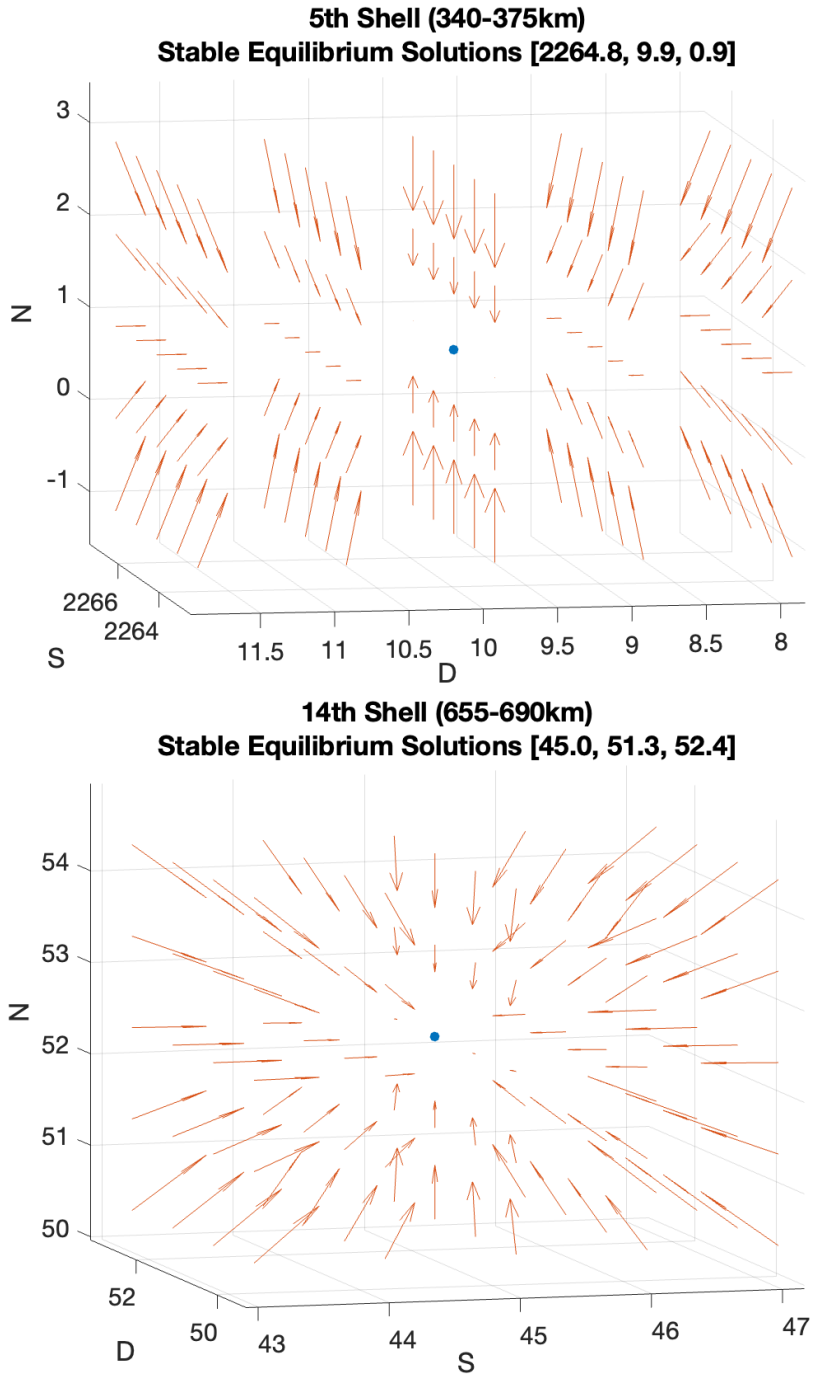

Figure 3-8: Phase portraits about the stable equilibrium state at different altitudes.

are given by Figure 3-5. The set of differential equations was integrated using these initial conditions. The results are shown for active satellites, derelict satellites, and debris in Figures 3-9, 3-10, 3-11, respectively, for each altitude shell. The population of active satellites settles into equilibrium across all shells within 10 years. The populations of derelict satellites and debris require greater than 50 years to reach equilibrium for particular altitude shells. This can be seen clearly in Figure 3-12 where the total species population is plotted over time along with the corresponding equilibrium value. The active satellite species reaches its equilibrium state faster than the other species because the launch rate is a direct source of active satellites as given in 2.1. The debris species takes the most amount of years to reach equilibrium as its population is determined by fragments that are produced through collisions between the species which is directly proportional to the species' population size. Thus, the debris population can only reach equilibrium once the populations of the other species reach their equilibrium state.

This analysis was repeated for the historic launch rate Case 1 (3.1.1) and the current populations of active, derelict, and debris objects in LEO, to see if the space environment has already triggered Kessler syndrome. The evolution of each species population is displayed in Figure 3-13. It can be seen that although the debris population begins above its equilibrium state, the evolution over time causes the debris population to converge toward equilibrium.

Sensitivity to PMD Probability

The sensitivity of the equilibrium solutions found for the Case 1 (3.1.1) launch rate to the probability of Post-Mission Disposal was analyzed. The equilibrium solutions for various PMD probabilities are plotted in Figure 3-14. No equilibrium solutions were found for successful PMD rates of 0.75 or lower. This analysis shows the importance of ensuring a high PMD probability is upheld by organizations in order for a stable state to exist in the orbital environment.

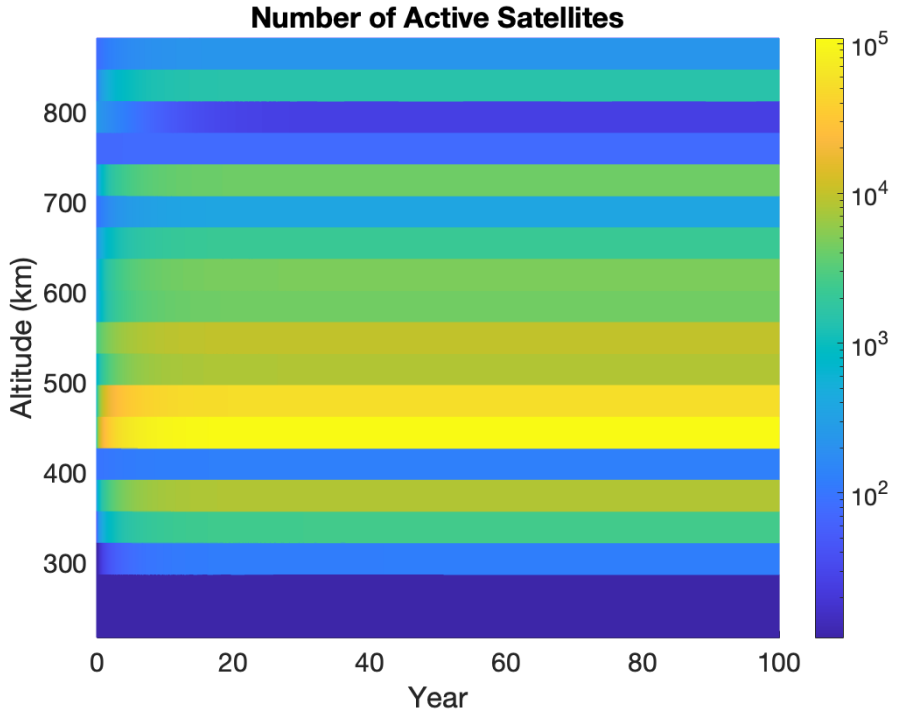

Figure 3-9: Evolution of the active satellite species population over time for the launch rate given in Section 3.1.1.

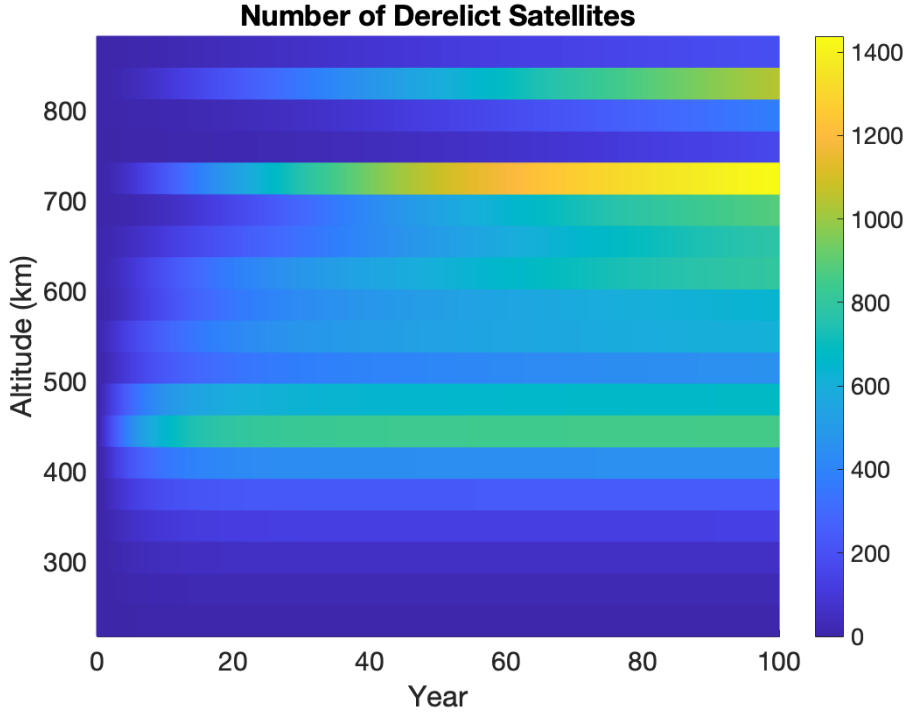

Figure 3-10: Evolution of the debris satellite species population over time for the launch rate given in Section 3.1.1.

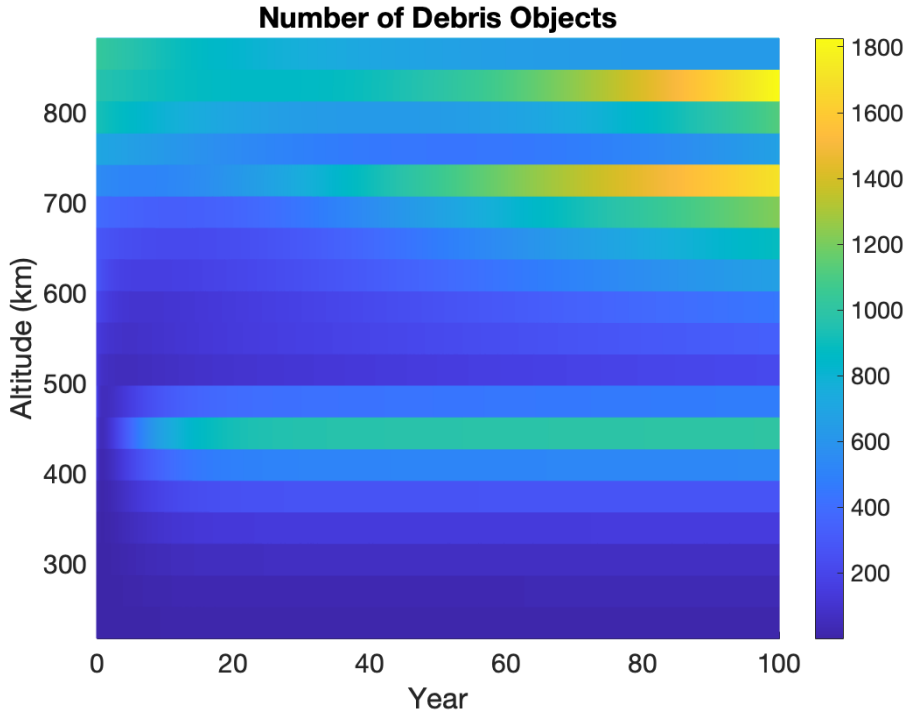

Figure 3-11: Evolution of the debris species population over time for the launch rate given in Section 3.1.1.

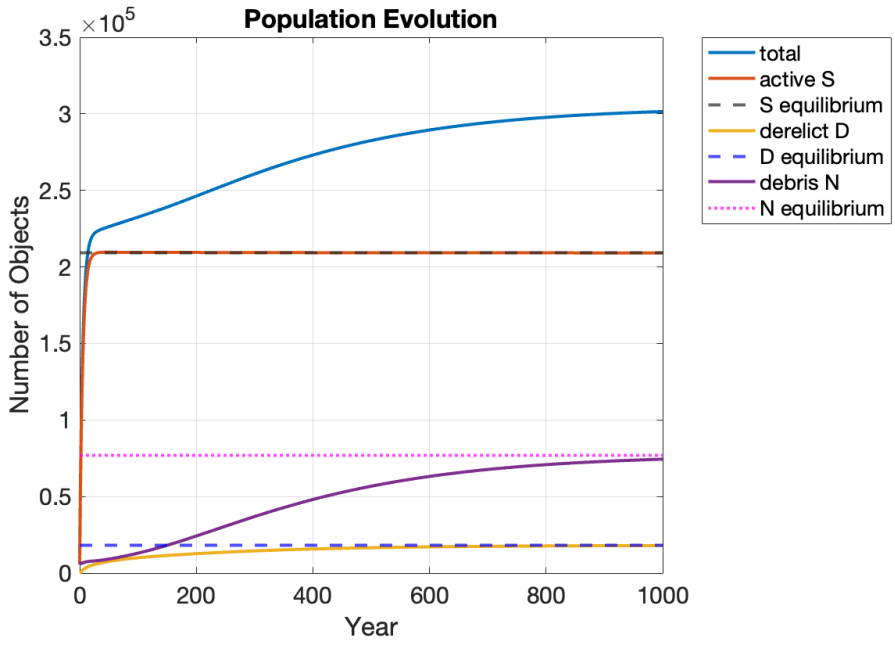

Figure 3-12: Evolution of species population towards equilibrium for Case 2 launch rate.

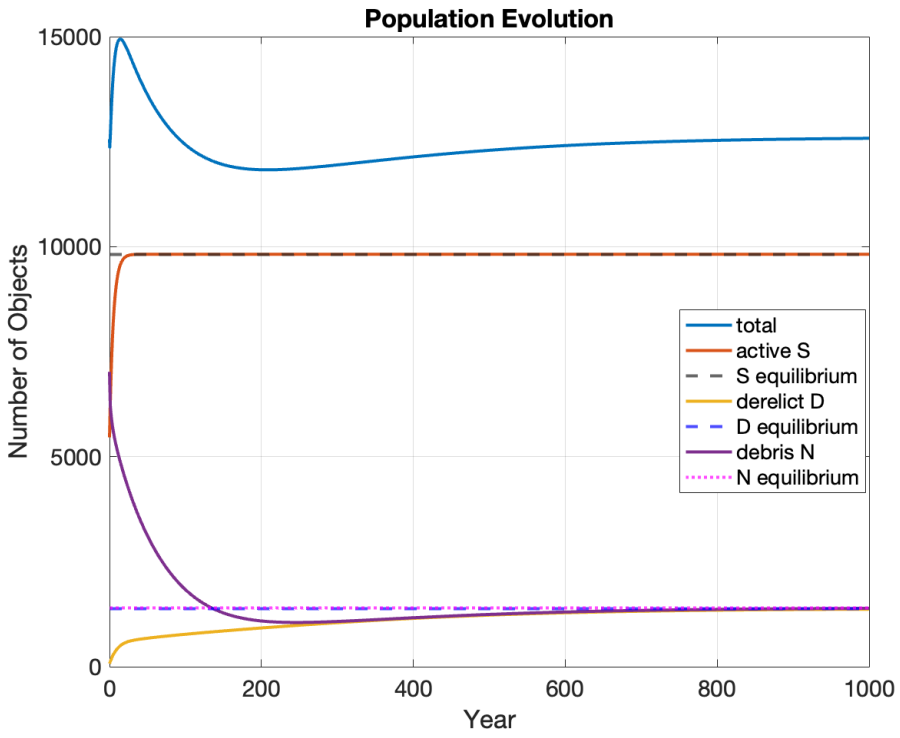

Figure 3-13: Evolution of species population towards equilibrium for Case 1 launch rate.

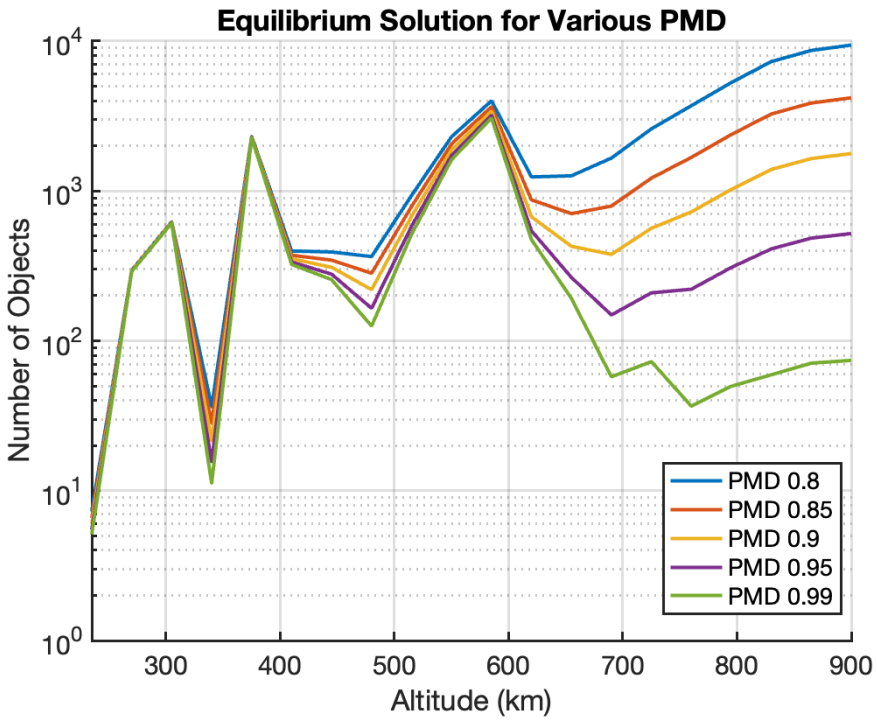

Figure 3-14: Equilibrium solutions for various probability of success of Post-Mission Disposal.

3.3 Perturbation Analysis

3.3.1 Perturbation in Launch Rate

The orbital environment's reaction to a one-time drastic increase in the launch profile was studied. This perturbation in launch rate allows for all ITU filings displayed in Figure 3-3 to be launched in one year. The utility of this approach is it is possible to study how the orbital environment reacts to a launch rate for which no equilibrium solutions exist as stated in Section 3.1.1. The model simulation was started in the equilibrium state computed in Section 3.2.1 for the Case 2 (3.1.1) launch rate. The system of equations was allowed to evolve for 20 years at this constant launch rate and then the launch rate was increased for one year.

After this one-year increase in launch activity, the launch rate was decreased back to the rate given by Case 2 (3.1.1) and allowed the system to evolve for another 20 years. The results are shown in Figure 3-15 for the evolution of each species

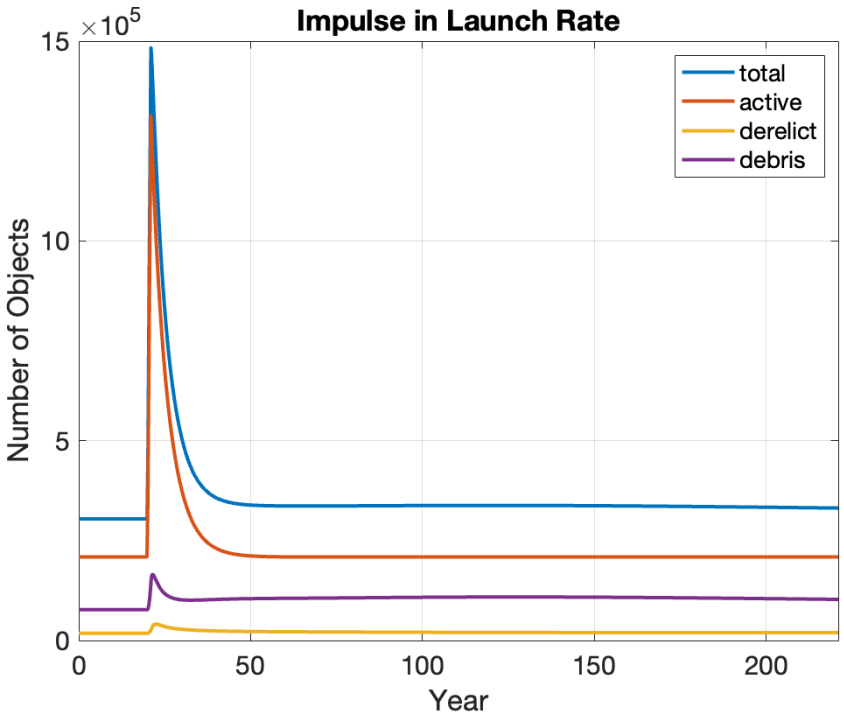

Figure 3-15: Species evolution with an impulse in launch rate at 20 years, perturbing the system away from equilibrium.

population. Overall, the system evolved back toward the stable equilibrium solution given in Figure 3-7 following the perturbation in launch rate. A change in the launch rate in effect perturbs the population of each species away from equilibrium. Once the launch rate is restored, the system recovers to its equilibrium state because the equilibrium solution for this launch rate is stable as computed in Section 3.2.3.

3.3.2 Perturbations of Equilibrium Solutions

The orbital environment's reaction to the event of a sudden increase in debris was studied. Two cases were analyzed: the first case depicts the effect of a uniform increase in debris across all shells, and the second case depicts the effect of debris increase in individual shells and compares a perturbation in debris at a high altitude vs. at a low altitude in LEO.

Table 3.4: Population of each species before and after a sudden increase in debris across all shells.

Species	Initial	At Event	After 200 Years	Δ
S	209142	-	209038	-104
D	18138	-	19057	+919
N	77010	277010	100145	+23136

Debris Perturbation Across all Shells

Starting with the system at equilibrium depicted in Figure 3-7 for the constant launch rate given by Case 2 (3.1.1), the amount of debris in each shell was perturbed by $10,000$ objects at $t = 20$ years and allowed the system to evolve for 200 years. The change in the amount of debris is shown in Figure 3-16. Table 3.4 summarizes these results by displaying the total amount of each species before the increase in debris, at the time of the event, and 200 years after. When there is an impulsive increase in debris, the number of active satellites decreases as more satellites are susceptible to collisions with debris. From Figure 3-16, it is evident that such an event creates a minimal effect in lower altitude shells with each species returning back to its equilibrium state within a few years. However, for higher altitude shells the scenario is drastically different with the system remaining out of equilibrium for at least 200 years. This analysis shows how an explosion type of event that produces a large amount of debris across all shells, greatly affects the amount of debris present at higher altitudes for many years following the event. Thus, any debris-generating event is more dangerous if it occurs at higher altitudes in LEO.

Debris Perturbations in High Shell vs Low Shell

From the equilibrium states displayed in Figure 3-7, the amount of debris was increased by 94,000 objects in the second-highest shell (830km-865km) and in the shell with an altitude range (410km-445km). The second highest altitude shell was chosen rather than the highest shell since it contained significantly more active satellites. For the lower altitude shell, the shell chosen was one that contained the greatest amount

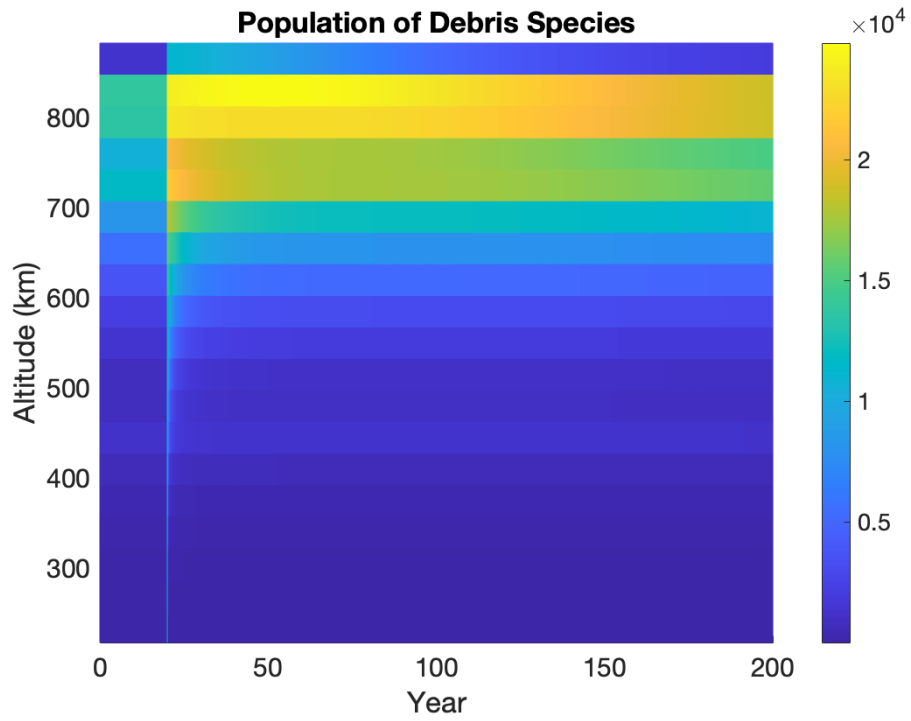

Figure 3-16: Debris population over time with an impulsive increase in debris by 10,000 fragments at 20 years.

of active satellites overall since this shell is the most sensitive to collisions between debris and active satellites. The orbital environment was set to equilibrium and then the perturbation of 94,000 objects in debris was added at $t = 20$ years. After this perturbation, the system was allowed to evolve for 200 years. The results are displayed in Figure 3-17. Increasing the amount of debris by 94,000 objects in a high-altitude shell has a much more significant impact on the overall LEO environment than increasing the debris in a lower-altitude shell. In Figure 3-17a it is evident that the environment quickly returns to its near-equilibrium state after the perturbation occurs, whereas the environment does not recover to equilibrium if such a perturbation occurs at a high altitude shell as shown in Figure 3-17b. Rather than returning to its equilibrium state, a large perturbation of the debris population at a high altitude causes the population of debris to keep growing across multiple shells over the course of 200 years. It could be that for a longer period of time $t > 200$ years, the system will return to its equilibrium state or it could be the case that the population of debris has reached

an amount that causes collisions to continuously occur and debris to grow without end. This behavior was studied in more detail next in Section 3.4.

3.4 Instability Threshold: Kessler Syndrome

Instability Threshold Definition: The maximum perturbation in the species population away from equilibrium for which the population continues to increase over 1,000 years.

Using the Case 2 (3.1.1) launch rate, the instability threshold was calculated for the debris species. The two types of perturbations used were perturbing the debris population in all shells simultaneously as done in Section 3.3.2 and perturbing the debris population in each shell individually similar to the approach used in Section 3.3.2. The system does not necessarily need to return to its equilibrium solution within 1,000 years of the perturbation but for the perturbation to be considered a part of the stable manifold, the populations of debris and derelict satellites need to be decreasing at the end of the 1,000 years. In other words, at $t = 1000$ years the set of $\{S, D, N\}$ must satisfy:

$$\dot{D} \leq 0, \ \dot{N} \leq 0$$

for all shells. The number of active satellites can be decreasing or increasing at the end of the simulation. In this way, the threshold at which run-away debris growth occurs, referred to as Kessler syndrome, was calculated.

3.4.1 Perturbing All Shells Simultaneously

To the nearest thousandth, the largest perturbation to the debris population across all shells for which the system reverted toward the equilibrium state after 1,000 years was found to be 40,000 debris objects. Perturbing the debris population by 41,000 objects was found to cause runaway debris growth. These two cases are displayed in Figure 3-18. In the left of Figure 3-18 it is clear that the perturbation in debris causes debris growth for about 400 years but the system begins to return to equilibrium as

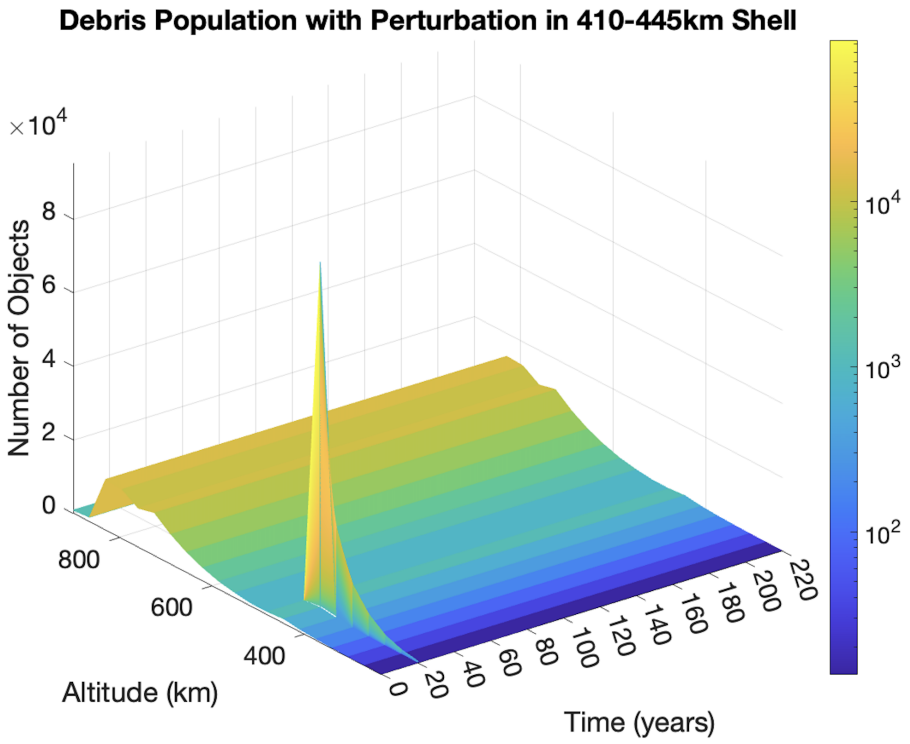

(a) A perturbation in debris in a low altitude shell.

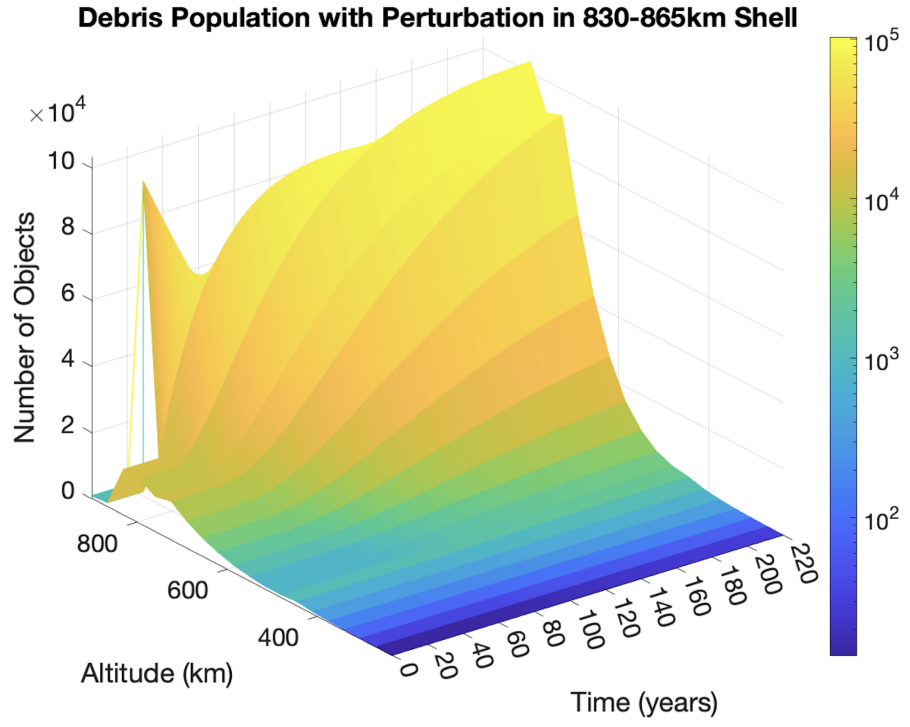

(b) A perturbation in debris in a high altitude shell.

Figure 3-17: A comparison of the evolution of the debris population after a sudden increase in debris at $t = 20$ years in two different shells.

it evolves for the remaining 600 years. This is not true for a perturbation of 41,000 debris objects as displayed in the right side of Figure 3-18, wherein the population of debris continues to grow to reach a couple of quintillions before the integration fails at $t = 600$ years. Such run-away debris growth displays Kessler syndrome as the orbital environment is unstable and continues to diverge away from its equilibrium state. Through increased collisions with active satellites, a perturbation in debris also causes a change in the population of derelict satellites. The evolution of the derelict population for a perturbation of 40,000 and 41,000 debris objects is displayed in Figure 3-19. Overall, the runaway debris growth occurred in higher altitude shells, but the instability threshold of lower altitude shells is also of interest. Thus, rather than simultaneously perturbing all shells away from equilibrium, the instability threshold of each altitude shell was studied in the next section.

3.4.2 Perturbing Shells Individually

By perturbing the amount of debris in each shell individually, the sensitivity of each altitude shell to a sudden increase in debris was studied. The maximum perturbation in the debris population away from equilibrium was calculated to the nearest thousandth for which the system evolved back toward equilibrium within 1000 years. The instability threshold hence exists at this maximum perturbation amount. The results are presented in Table 3.5. Altitudes below 410 km are not included in the table because these shells could withstand a perturbation of debris equal to 10^8 objects. In conclusion, the stability of the orbital environment at lower altitude shells is much more resilient to perturbations in debris than in higher altitude shells. This result concurs with the result of Section 3.3.2. The reasoning for this behavior is the sink of the model, namely atmospheric drag, is much greater at lower altitude shells, which removes debris from the environment preventing collisions with active and derelict satellites that would create more debris. It is worth noting that this analysis was done for a particular launch rate taken as a fraction of the ITU filings as shown in Figure 3-7. Debris creation is directly affected by the launch rate since launch activity is the source of active satellites per shell, and a higher density of active satellites per

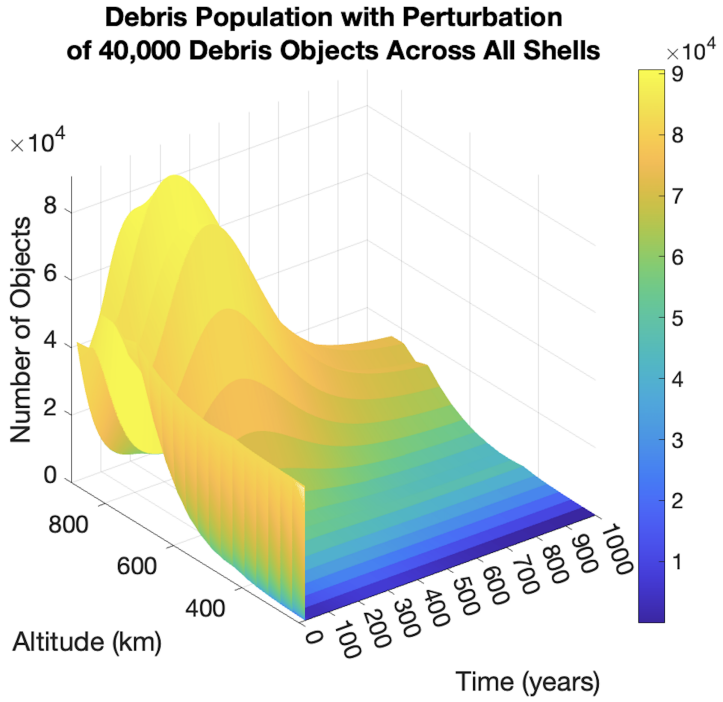

(a) The maximum perturbation in debris, to the closest thousandth of objects, within the basin of attraction of the equilibrium solution.

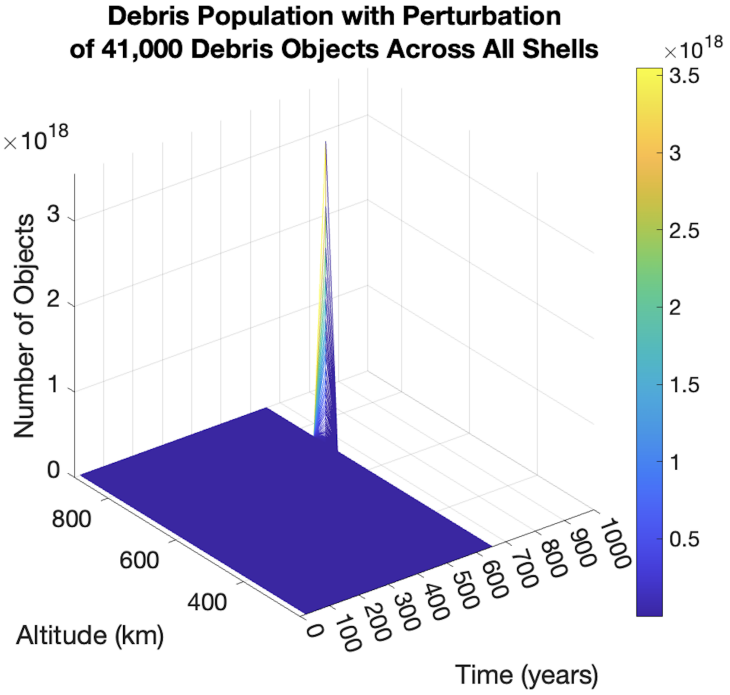

(b) A perturbation in debris outside of the basin of attraction, leading to run-away debris growth.

Figure 3-18: A comparison of the evolution of the debris population after a stable and unstable perturbation in debris occurs across all shells.

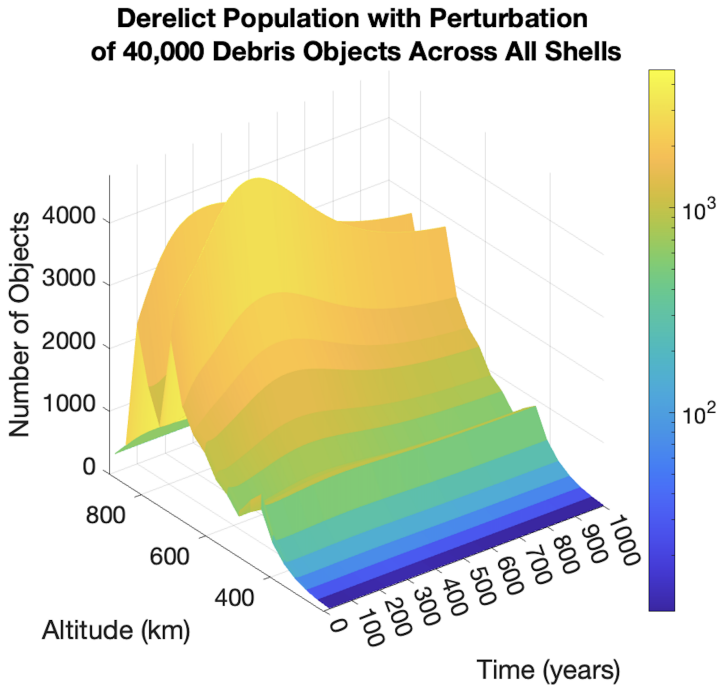

(a) The evolution of the derelict species for the maximum stable perturbation in debris shown in Figure 3-18a.

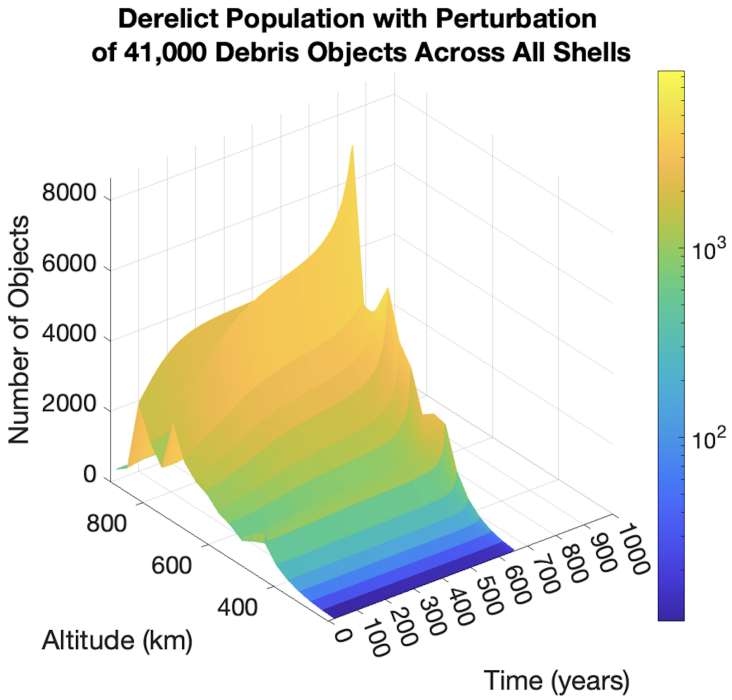

(b) The evolution of the derelict species for the unstable perturbation in debris shown in Figure 3-18b.

Figure 3-19: A comparison of the evolution of the derelict population after a stable and unstable perturbation in debris across all shells.

Table 3.5: Maximum perturbation in debris per shell before Kessler Syndrome occurs.

Altitude Shell (km)	Debris at Equilibrium	Max. Perturbation in Debris
410-445	1198	54070000
445-480	825	30123000
480-515	819	17331000
515-550	1376	9911000
550-585	2203	5791000
585-620	3623	3342000
620-655	5545	1999000
655-690	8224	1224000
690-725	11720	648000
725-760	10631	438000
760-795	13544	282000
795-830	13851	120000
830-865	1274	95000
865-900	907	80000

shell creates a greater likelihood of collisions with debris. Thus, different evolution of the debris population would occur for a different launch rate, but the conclusions about the sensitivity to run-away debris growth at higher altitudes compared to lower altitudes would remain the same.

3.5 Debris Capacity

Debris Capacity Definition: For a given launch rate, the maximum debris population that can exist in a given orbital volume before Kessler Syndrome occurs as given by the instability threshold for that volume.

The debris-based orbital capacity C is defined as

$$C(\lambda) = P_{equil} + P_m \tag{3.1}$$

where λ is the launch rate, P_{equil} is the debris population at equilibrium, and P_m is the maximum perturbation in debris away from equilibrium in the stable region. Any increase in debris beyond this amount would cause the system to enter the

unstable region where Kessler Syndrome occurs. Perturbations of the type given in Section 3.4.1 are used to calculate the debris capacity of the 200-900 km LEO environment for a fixed perturbation in debris across all altitudes. For instance, for the ITU derived launch rate λ_{itu} in Case 2 (3.1.1), $P_{equil} = 304,290$ as given in Table 3.2 and $P_m = 41,000 \cdot 20 = 820,000$ where the maximum perturbation found in 3.4.1 was multiplied by the number of shells since the 200-900 km region was considered. The capacity was found to be

$$C(\lambda_{itu}) = 1,124,290$$

Debris perturbations of individual shells as given in Section 3.4.2 are used to calculate the debris capacity per altitude shell. A debris capacity per altitude shell h was defined as

$$C(\lambda, h) = P_{equil}(h) + P_m(h) \tag{3.2}$$

For the same launch rate λ_{itu} the debris capacity of each altitude shell was computed by adding the two columns of Table 3.5 corresponding to equilibrium and perturbation populations. The result is displayed in Figure 3-20.

The debris capacity of the 200-900 km region of LEO was found without considering non-trackable debris objects which may change the population inputs in equation 3.2. The exact capacity values depend on the model's input parameters and assumptions and thus could change if the model is calibrated against other models.

3.6 Discussion of Results

Given a constant launch rate distribution that is based on historic launch activities (3.1.1) and the current species' populations, the current orbital environment will evolve to a stable equilibrium state given the assumptions of this model. In such a state, the sources of the model, namely due to launch and collisions, balance the sinks of the model, namely post-mission disposal and atmospheric drag. Thus if launch activities remain at current levels, Kessler syndrome will not occur in the

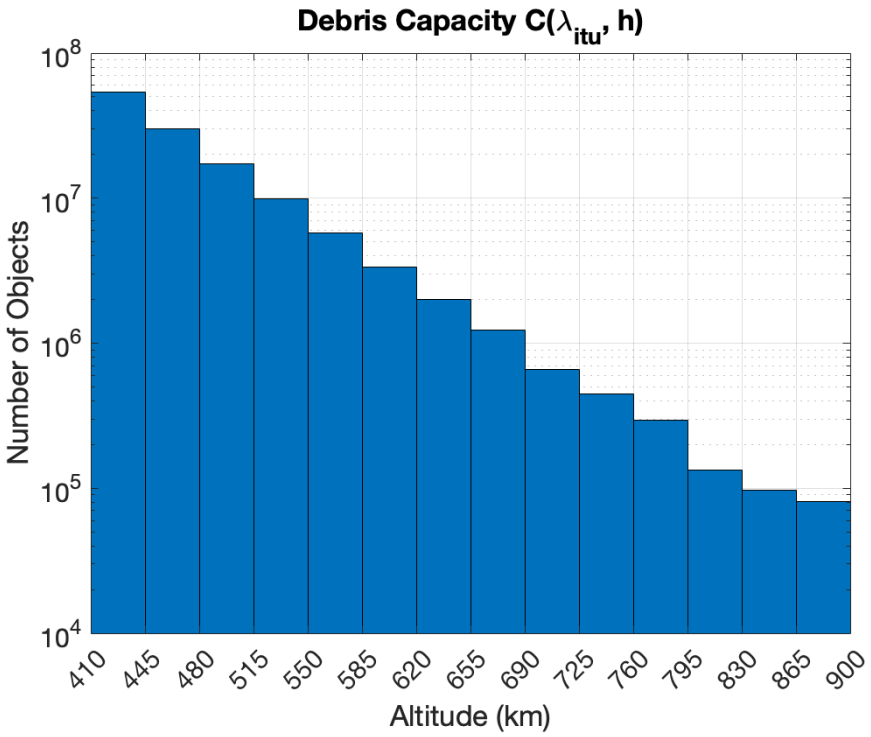

Figure 3-20: Debris capacity calculated per altitude shell.

200-900 km altitude range of the orbital environment, given the assumptions of this model. This is also true for an increased but constant launch rate (3.1.1) for which a stable equilibrium state exists. The evolution of the environment from the current populations of active, derelict, and debris objects to this equilibrium state would take decades. Given a dynamic launch rate distribution, an ever-increasing launch rate entails the system will not reach an equilibrium state. However, if the launch rate becomes constant after a period of continuous growth then the system may evolve toward the equilibrium state if the growth rate was small enough. In this analysis, only a growth rate of 1% in launch rate per year over 50 years leads to a stable equilibrium state. Larger growth rates in launch rate entailed no equilibrium state would be reached with each species population ever-increasing.

Perturbations in the debris population away from equilibrium showed how sensitive the environment is to an increase in debris. In general, perturbations in the debris populations in higher altitude shells had more drastic consequences than perturbations in lower altitude shells due to increased atmospheric drag forces existing

at lower altitudes. Run-away debris growth is more common at high altitudes, with Kessler syndrome resulting from significantly smaller perturbations in debris than at lower altitudes. Thus a debris-generating event occurring at a high altitude is more dangerous than one occurring at a low altitude since at higher altitudes such an event can more easily trigger Kessler syndrome to occur.

Chapter 4

Improvements to the Source-Sink Model

In this chapter, a data analysis of the objects in orbit cataloged in DISCOS[1] is presented wherein with updated species parameters and initial species populations. Then the MOCAT source-sink model is compared to other models in the literature, namely the Model for Investigating control Strategies for Space Debris (MISSD) proposed by Somma [55] and ESA's DELTA model [60] to assess the model's capabilities. Two functionalities missing from the MOCAT source-sink model were deemed as necessary additions, namely a calibrated explosion model and an improved Post-Mission Disposal model. This chapter covers how these two functionalities are added to the existing source-sink model. Then the dispersion of fragments in explosion events is studied to test the shell binning method used in the model. The chapter concludes with a comparison of several simulations computed using the improved source-sink model against simulations computed using ESA's DELTA model to validate the source-sink model's predictions.

[1]DISCOS data was provided by ESA's European Space Operations Centre (ESOC) https://discosweb.esoc.esa.int/.

4.1 Species Characteristics

Source-sink models rely on accurate species parameters to represent the orbiting population of spacecraft and debris. The physical characteristics of each species were determined from DISCOS data. The DISCOS database categorizes objects into 11 categories as displayed in Figure 4-1. The plots of the mass and area values of each object according to category type are shown in Figures 4-2 and 4-3, along with the median mass (kg) and the median area (m^2). These values, along with the number of objects per category and the number of missing mass values, are presented for all 11 categories in Figure 4-1. The objects in the DISCOS data set were binned into 1 of 4 species types to fit in the MOCAT model framework and a small fraction of the objects were ignored. The 4 types of species considered in the binning process were: Active satellites (S), Derelict satellites (D), Debris (N), and Rocket Bodies (B). The reason that a fraction of the objects in the data set were ignored was because they made up a small number of objects, which is true for the 'Other Debris' and 'Other Mission Related Objects' categories, and their properties were not well represented by any of the 4 species characteristics. The latter being true for the 'Payload Mission Related Objects' and the 'Rocket Mission Related Objects' as these objects were much larger than the median debris masses and sizes but these objects do not fit in with the description of active, derelict, or rocket body objects as described in Section 2.2.1.

The species characteristics for active satellites and rocket bodies were calculated from the binned objects. Derelict species characteristics were taken to match the characteristics of the active species because active satellites become derelict objects at the end of their lifetime. Since $11,257$ out of the $11,209$ mass values were missing for the objects binned into the debris species, the characteristic mass and area values were taken from Somma's species parameters [55]. The species characteristics are displayed in Table 4.1. These can be compared to the species characteristics used in Somma's source-sink model [55] given in Table 2.3.

Table 4.1: Species Characteristics used in MOCAT-4B.

	Active	Derelict	Debris	Rocket Body
Mass (kg)	260	260	0.640	1421.21
Area (m^2)	2.885	2.885	0.020	10.603
Diameter (m)	1.9166	1.9166	0.180	3.6742

	Other Debris	Other Mission Related Objects	Payload	Payload Debris	Payload Frag. Debris	Payload Mission Related Objects	Rocket Body	Rocket Debris	Rocket Frag. Debris	Rocket Mission Related Objects
Num. of Objects	2	4	6095	113	7427	306	1437	164	3553	906
Num. of Missing Mass Values	2	0	48	113	7386	244	7	164	3546	475
Median Mass (kg)	-	5280.82	260	-	1	51.01	1421.21	-	1	55.50
Median Area (m^2)	0.0334	0.1625	2.885	0.019	0.0097	0.0506	10.603	0.1	0.057	0.0851

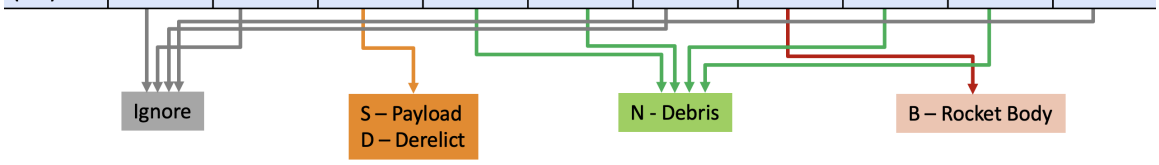

Figure 4-1: DISCOS 2022 reference population characteristics and species categorization.

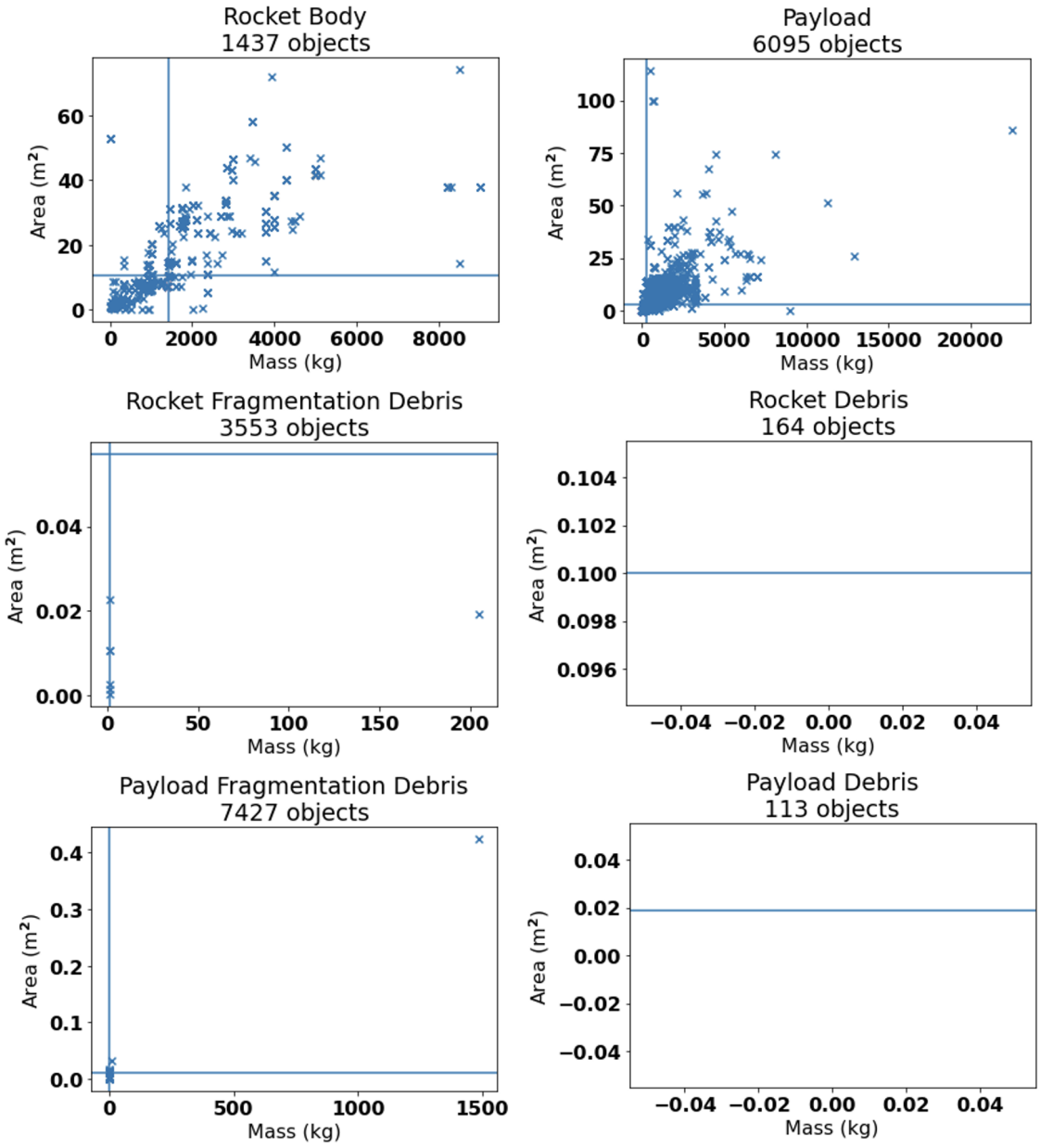

Figure 4-2: DISCOS 2022 reference population characteristics for objects included in MOCAT-4 categorization.

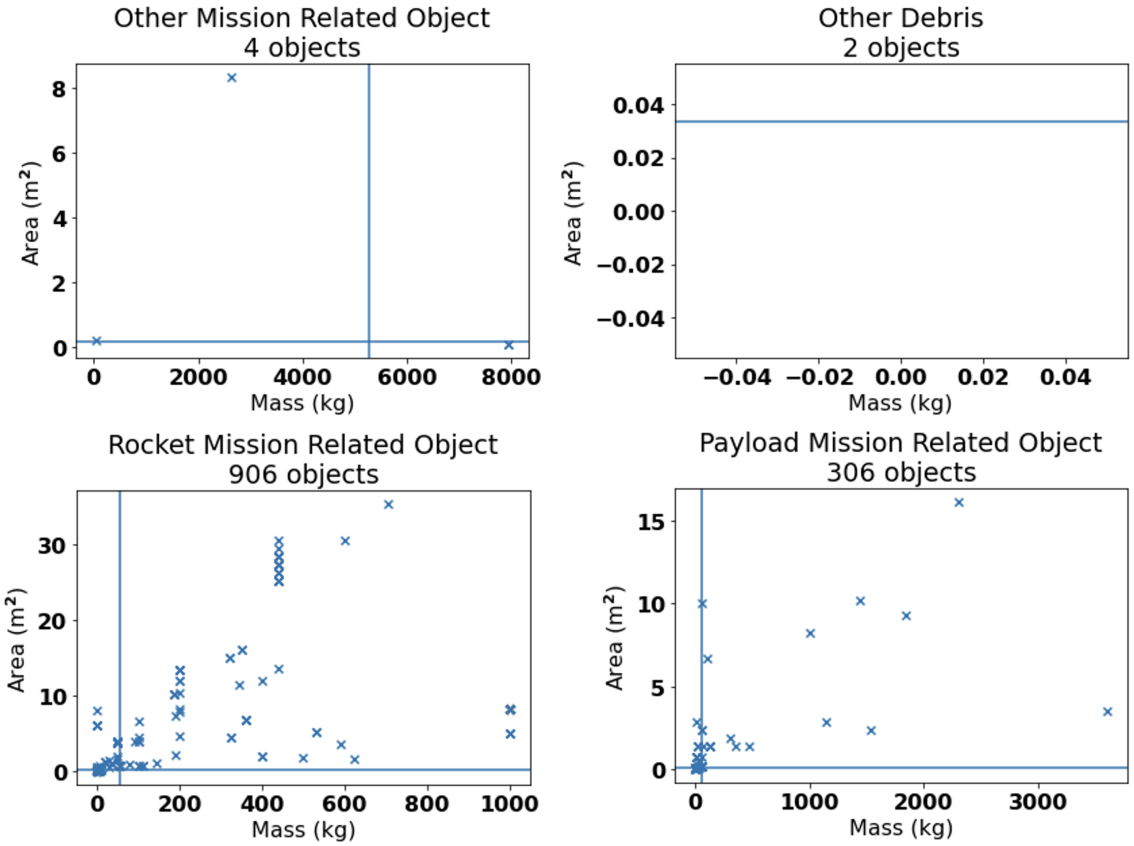

Figure 4-3: DISCOS 2022 reference population characteristics for objects not included in MOCAT-4 categorization.

4.2 Explosion Model

Including explosion events as a debris-generating mechanism in the source-sink model framework is important to accurately model the future orbital environment. An explosion model was implemented to include fragmentation events that occur without collisions when an object in orbit breaks up and creates debris. Although researchers believe that with improved passivation guidelines and technological developments the probability of an explosion event occurring will decrease with time [17], explosion events create large clouds of debris and should be included in debris modeling. Thus, an explosion model was developed and added to MOCAT-SSEM.

Since MOCAT-SSEM models the evolution of each species population, the explosion model implemented contains an explosion rate per species as proposed by Somma [55]. This differs from DELTA's explosion rate given as a probability of explosion per RSO based on the number of years the RSO has been in orbit, with a nearly zero chance of explosion after 18 years [17]. The explosion model depicting fragment generation developed by Somma [55] is:

$$\dot{E}_{EX} = \dot{E}_{IP} n_{E,IP} + \dot{E}_{RB} n_{E,RB} \tag{4.1}$$

where the explosion rate is $\dot{E}$ and n is the number of fragments produced per explosion event. Here IP refers to Inactive Payloads and RB refers to Rocket Bodies, while EX refers to explosions causing debris. Somma's model sets the explosion rate of all other space objects to 0 as these were considered to either be lacking components that could cause explosions such as mission-related objects with no fuel tanks, or because Somma assumed future technological development would eliminate battery failure as a source of explosions in active satellites. Here, a more conservative approach was taken where each species type was assigned an explosion rate. The rate is independent of the shell altitude but dependent on the number of objects in the shell. The explosion model per species is:

Explosion	S	D	N	B
$\dot{E}$	$-\dot{E}_S S$	$-\dot{E}_D D$	$\dot{E}_S n_{E,S} S + \dot{E}_D n_{E,D} D + \dot{E}_B n_{E,B} B$	$-\dot{E}_B B$

The explosion terms represent the change in each species population, thus explosions remove active, derelict, and rocket body objects and add new fragments to the debris population. In the model, n is given by the NASA standard breakup model [30] as:

$$n\left(L_c\right) = c_Q 6 L_c^{-1.6} \tag{4.2}$$

where c_Q is a type-specific factor and L_c is the characteristic length of the debris objects. DELTA's explosion rate per object is based on historical fragmentation data from the last 18 years [17]. Analogously, historical fragmentation events were used to calibrate the explosion rate per species for MOCAT-SSEM using the DISCOS database for explosions occurring within the last 18 years. This calibration is discussed in 4.2.1. The number of explosions per species type for the 2022 reference population is shown in Figure 4-4. An assumption adopted from DELTA's explosion model was to consider only non-systematic explosions in calibrating the explosion rate as ESA argues that system-related events are not representative of the orbital environment [17].

4.2.1 Fragmentation Data Analysis

The following steps were taken to process the DISCOS database of fragmentation events per epoch to find the explosion rate $\dot{E}$ per species object:

1. System-related events were discarded.
2. Only explosion events in LEO were considered.
3. The type of object that exploded was retrieved.
4. The sum of the number of exploding objects of each type was calculated.
5. The sum was divided by the total number of objects of that type in orbit for the given epoch.

The last step was taken to compute a rate per object for each species type rather than a rate per species. In this way, the number of explosions will scale with the number

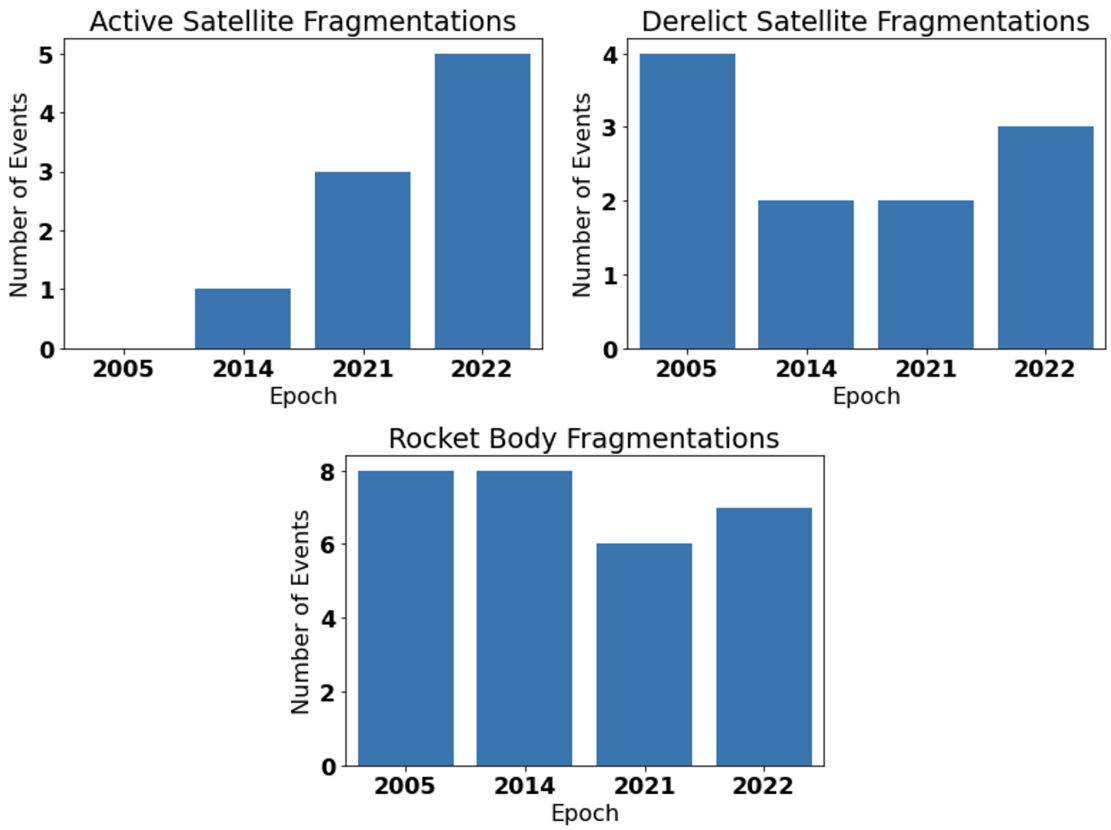

Figure 4-4: Number of explosion events per species type and epoch of DISCOS data.

of objects of that type of species in orbit. This more accurately depicts how the orbital environment was to evolve if the population of RSOs is to drastically increase or decrease over time as compared to having a fixed explosion rate per year.

Two additional checks were performed on the fragmentation data: checking the eccentricity and altitude of the exploding objects. These checks ensured that there was no direct correlation between a particular altitude band or orbit type in LEO and explosion events. Analyzing the eccentricity of the exploding objects also ensured the assumption of modeling these exploding objects within spherical shells on nearly circular orbits is accurate. The eccentricity of the exploding objects was plotted for all events per epoch in Figure 4-5. In the analysis done in this chapter, a shell width of 50km was assumed. The 2022 epoch data set is considered in which all fragmentation events occurred at or below the $1550-1600$km altitude shell. Assuming an orbit with radius at apoapsis (R_a) and periapsis (R_p) to be at the edges of the shell, then the shell tolerates a maximum eccentricity of:

$$e = \frac{R_a - R_p}{R_a + R_p} = \frac{35}{1550 + 1600} = 0.0158$$

which allows for most exploding objects in the 2022 data set of Figure 4-5. This highlights a limitation of the circular shell approximation. However, none of the exploding objects were highly eccentric.

Furthermore, the altitudes of the exploding objects was studied. The aim was to ascertain whether an explosion traffic per altitude shell should be implemented rather than an explosion rate per object. For the 2022 epoch data set that includes explosion events from the previous 18 years, the number of fragments produced versus the altitude was plotted in Figure 4-6. No correlation with specific altitude shells was found. Thus, an explosion rate per object was implemented.

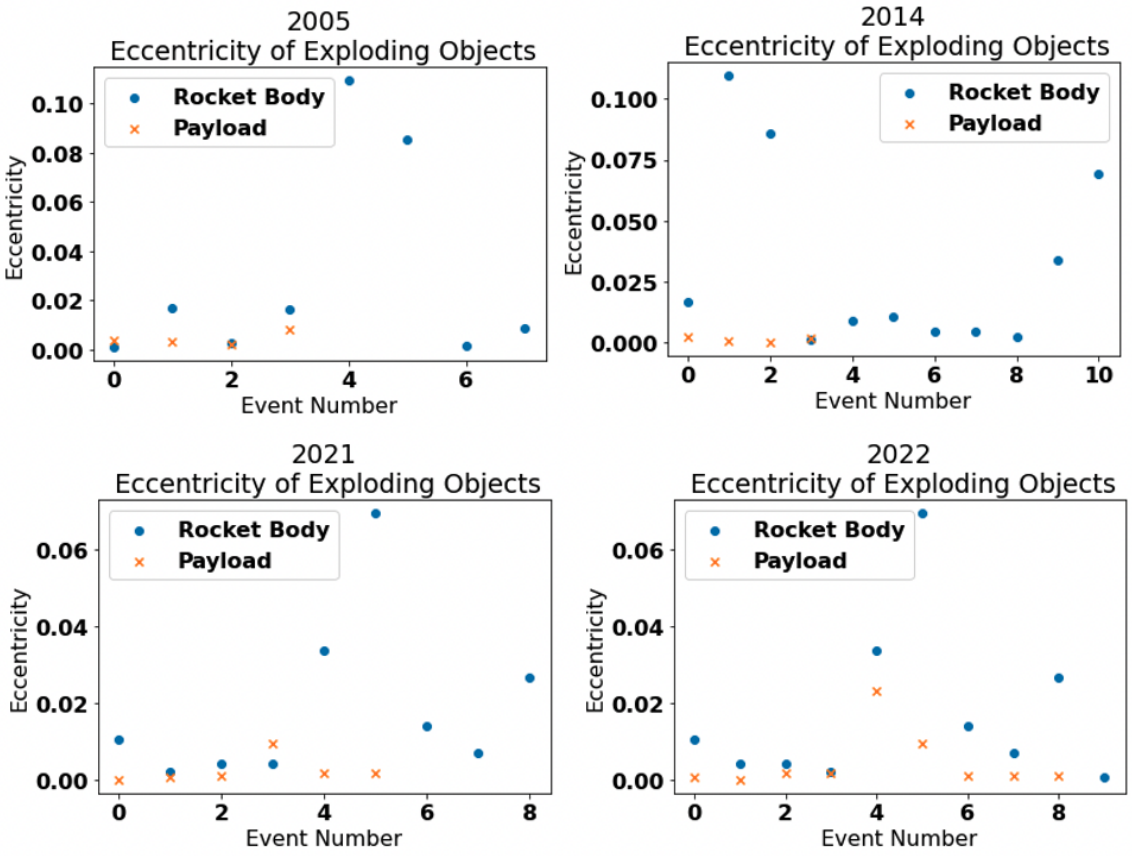

Figure 4-5: Eccentricity of the objects exploding per epoch.

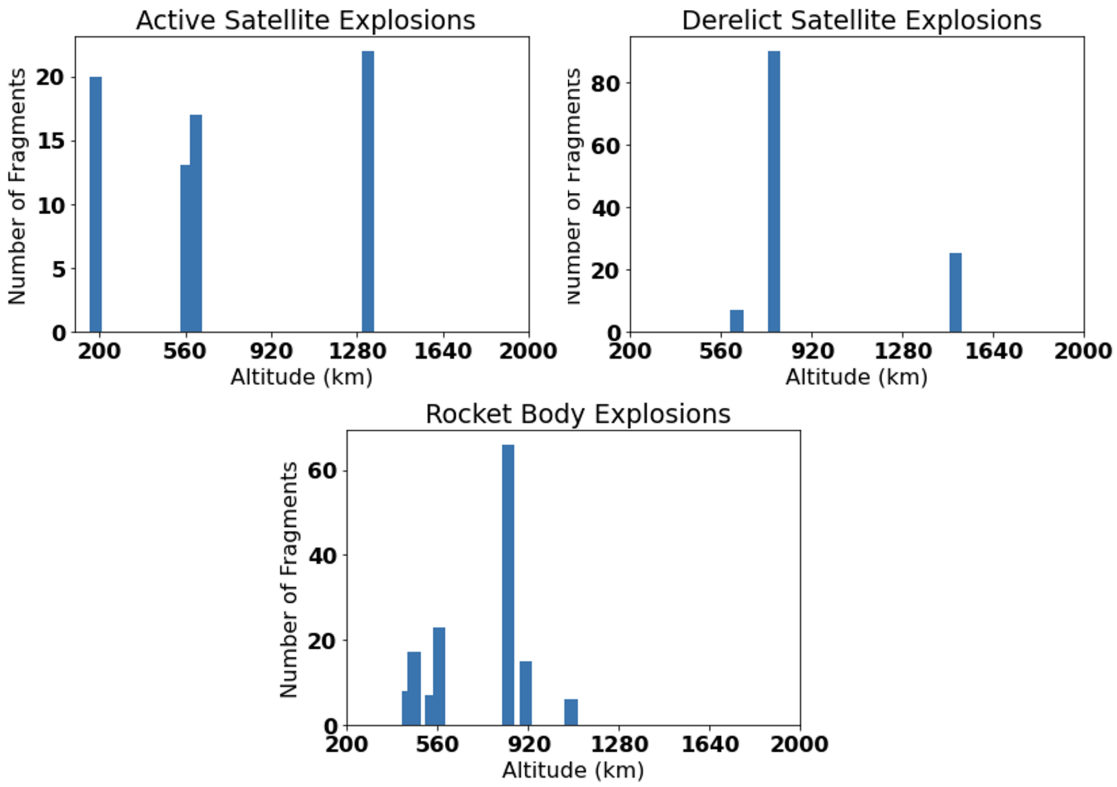

Figure 4-6: Number of fragments produced at various altitudes for explosions occurring in the 2022 epoch data set.

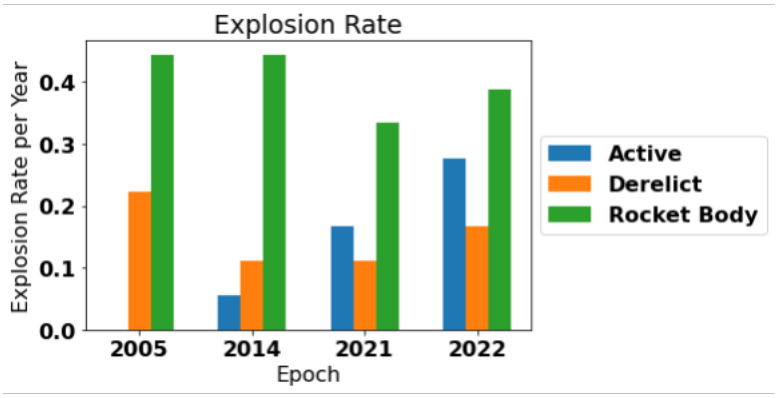

Figure 4-7: Explosion rate per species type and epoch of DISCOS data.

Table 4.2: Computation of the explosion rate per object for each species.

Epoch	Species	Explosion Rate per Year	Species Population	Explosion Rate $\dot{E}$
2022	S	0.277	3861	0.000071743
	D	0.166	412	0.00040291
	B	0.388	247	0.0015709

4.2.2 Explosion Parameters

Assuming the species type is represented by Q then the explosion rate per species object was computed as:

$$\dot{E}_Q = \frac{N_{\text{exp},Q}}{18} \frac{1}{Q_{\text{t=epoch}}} \tag{4.3}$$

where $N_{\text{exp},Q}$ is the number of explosion events in that epoch data set and $Q_{\text{t=epoch}}$ is the population of the species at that epoch time. A factor of 1/18 is included to calculate the average number of explosion events per year since the epoch data set includes the number of explosion events for the last 18 years before the epoch date. The calibrated explosion rates for all objects in a species for each epoch are shown in Figure 4-7. The explosion rates per object for each species was computed by dividing the explosion rate per species by the population of the species; this rate is shown in Table 4.2 for the 2022 epoch data set.

The factor c_Q was calibrated by computing the median number of fragments produced per species shown in Figure 4-8. Assuming a characteristic length of debris of

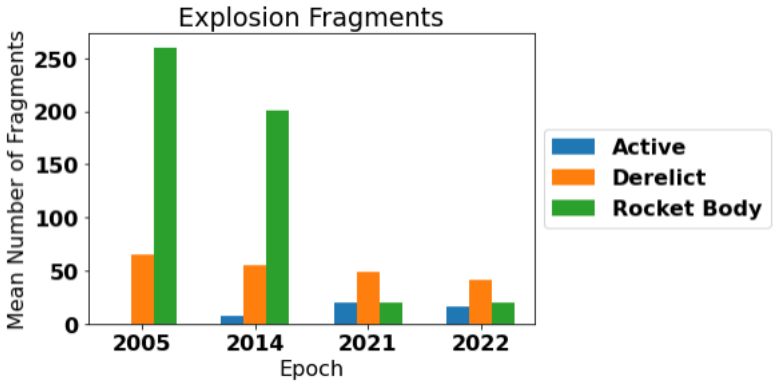

Figure 4-8: Mean number of fragments produced by explosions of each species type per epoch.

10 cm then the mean number of fragments was computed per species as:

$$n(L_c) = \frac{\Sigma N_{\text{frag},i}}{N_{\text{exp},i}} \tag{4.4}$$

where $N_{\text{exp},i}$ is the number of explosion events, $N_{\text{frag},i}$ is the number of fragments produced in explosion event i and the sum is over all the explosion events of that species within the specified epoch. The mean number of fragments produced per species type per epoch is displayed in Figure 4-8. As stated in [26], $n(L_c)$ represents the mean cumulative number of fragments of length greater than the characteristic length of 0.1 m. However, since all debris fragments are represented by the same characteristic size and mass as members of the debris species, $n(L_c)$ is taken as a source of debris in equation 2.1.

The characteristic scaling factor is calculated by rearranging Equation 4.2 to get:

$$c_Q = \frac{1}{6}\frac{\Sigma N_{\text{frag},i}}{N_{\text{exp},Q}} L_c^{1.6} \tag{4.5}$$

where the summation is over number of explosion events. The calibrated characteristic factors per species are displayed in Figure 4-9, which also displays the variation in c_Q per epoch. Simulations with the new explosion model implemented are provided in Section 4.5.

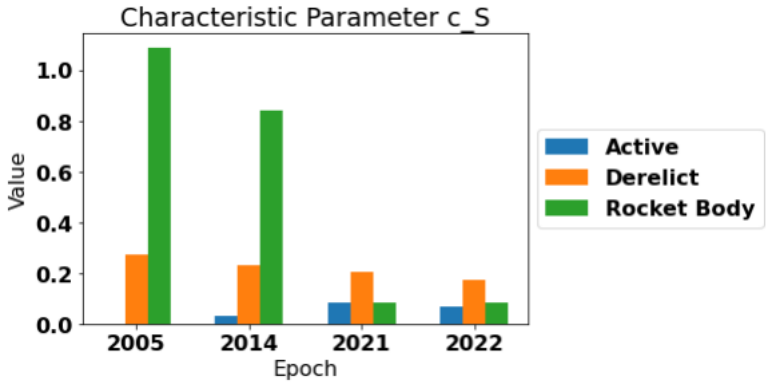

Figure 4-9: Calibrated type dependent factor c_Q used in Equation 4.2.

4.3 Improved PMD Model

An improved PMD model was implemented for the active satellites that have reached their end-of-life and for rocket bodies as depicted in Figures 4-10 and 4-11. Active satellites become derelict satellites after their specified lifetime duration has passed, typically 8 years. The probability of successful post-mission disposal dictates what fraction of active satellites remain in their current shell as derelict satellites that do not undergo PMD and what fraction of active satellites become derelict satellites injected at a lower altitude shell. The original PMD model used in MOCAT-SSEM removed active satellites from the simulation at a rate proportional to the probability of successful PMD at their end-of-life. The lower altitude shell used in the new PMD model corresponds to an altitude where derelict satellites will de-orbit due to atmospheric drag effects within the chosen PMD duration, typically given as 25 years. Rocket bodies in MOCAT-4B were originally modeled as undergoing de-orbiting movements only due to atmospheric drag effects. A PMD model for rocket bodies was implemented, in which the rocket body is removed from the orbital environment within one year of launch at a specified probability of success rate. Simulations with the new PMD model implemented are provided in Section 4.5.

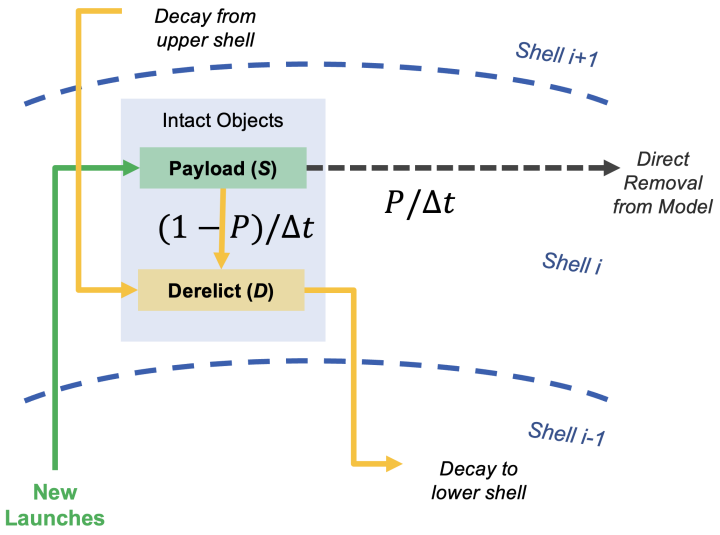

(a) Old PMD model for active satellites.

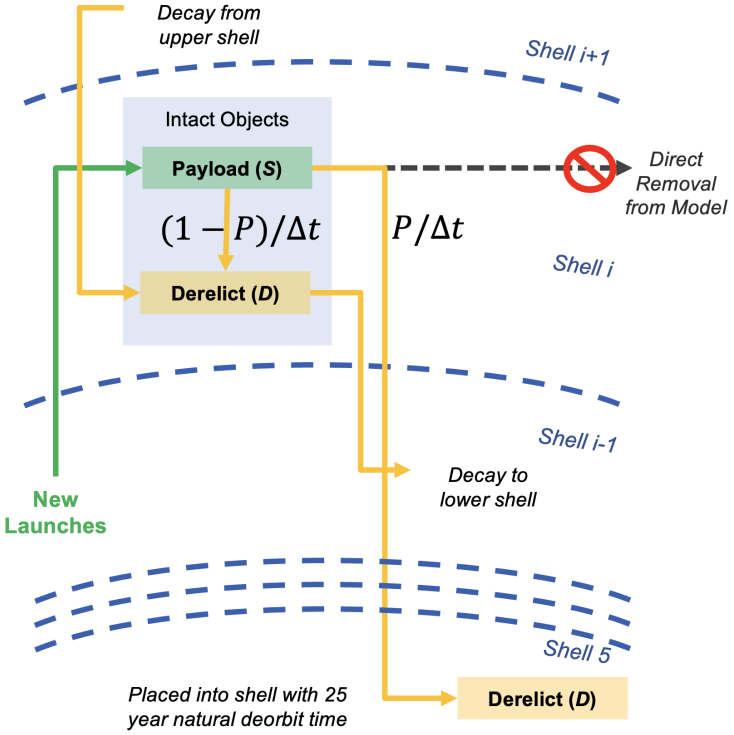

(b) New PMD model for active satellites.

Figure 4-10: Post-Mission Disposal model for active satellites where P is the probability of successful PMD and Δt is the satellite lifetime.

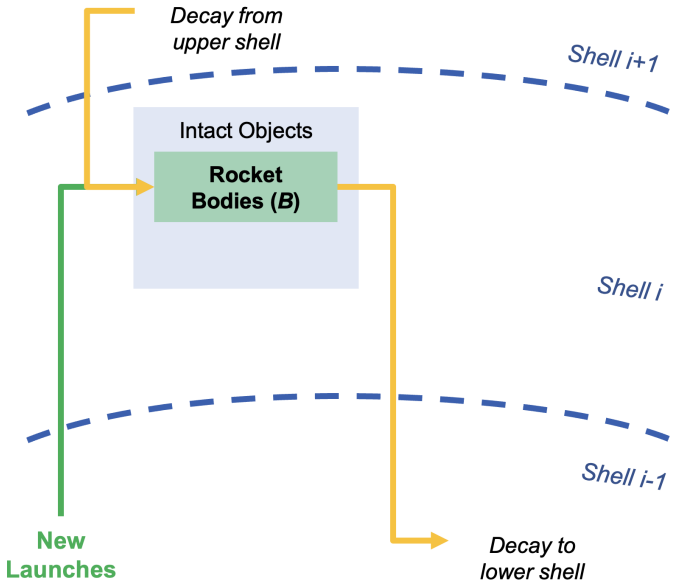

(a) Old PMD model for rocket bodies.

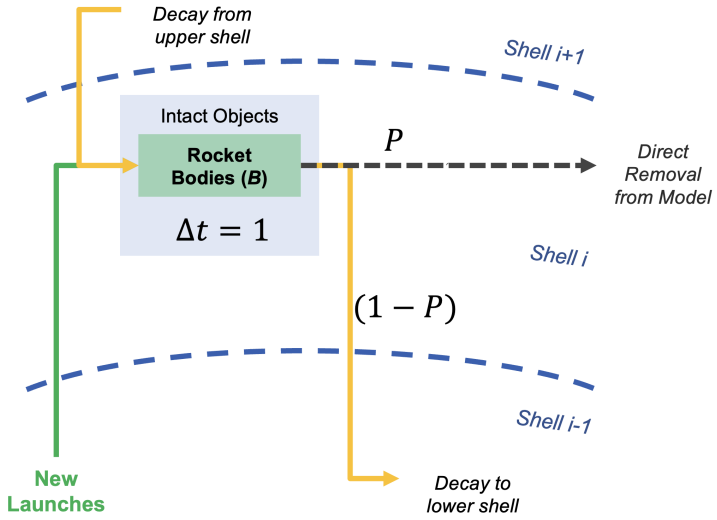

(b) New PMD model for rocket bodies.

Figure 4-11: Post-Mission Disposal model for rocket bodies where P is the probability of successful PMD and Δt is the satellite lifetime.

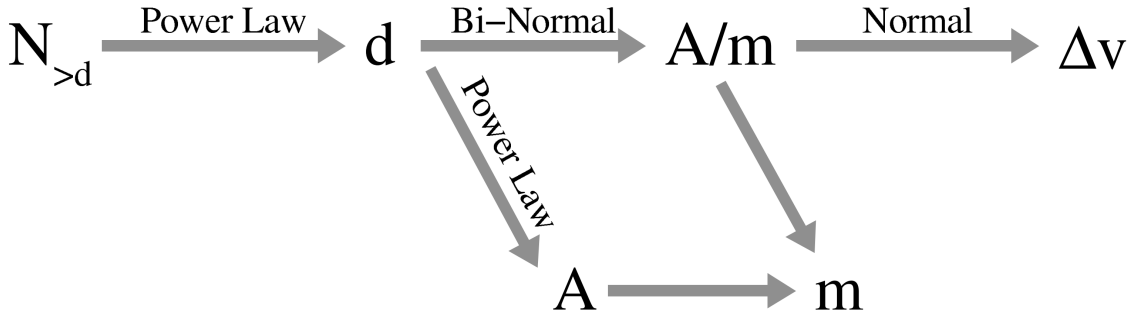

Figure 4-12: Derivation of the cross-sectional area, mass and imparted velocity for explosion events [35].

4.4 Dispersion of Fragments

The dispersion of fragments was analyzed in the context of the source-sink model.

4.4.1 Theory of Fragment Dispersion

In this section, the theory behind fragment dispersion from an explosion event is reviewed. The assumption of Section 4.2.2 wherein all fragments produced in an explosion take on the characteristic sizes of the debris species is no longer employed. The NASA Standard Breakup model was used to determine the area-to-mass ratio and imparted velocity of the debris fragments produced in explosion events as described in reference [35]. An outline of the derivation is given in Figure 4-12. The bi-modal probability density function used to assign area-to-mass ration values to fragments larger than 0.1m, as implemented in EVOLVE 4.0 and given in reference [26], is:

$$\begin{aligned} \rho(\chi,\delta) &= \alpha(\delta)\rho_1(\chi) + (1-\alpha(\delta))\rho_2(\chi) \\ \rho_i(\chi) &= \frac{1}{\sigma_i\sqrt{2\pi}} e^{-(\chi-\mu_i)^2/(2\sigma_i)} \\ \chi &= \lg(A/m) \end{aligned} \tag{4.6}$$

where $\mu_i, \sigma_i = f(\delta)$ and $\delta = \lg \hat{d}$. Here $\hat{d}$ is the normalized fragment diameter. The weighting factor α, mean value μ_i, and standard deviation σ_i of the normal distribution differ for rocket bodies and satellites. As stated in reference [26], for

rocket bodies these parameters are:

$$
\begin{aligned}
\alpha &= \begin{cases} 1 & \forall \delta \leq -1.4 \\ 1 - 0.3571(\delta + 1.4) & \forall -1.4 < \delta < 0 \\ 0.5 & \forall \delta \geq 0 \end{cases} \\
\mu_1 &= \begin{cases} -0.45 & \forall \delta \leq -0.5 \\ -0.45 - 0.9(\delta + 0.5) & \forall -0.5 < \delta < 0 \\ -0.9 & \forall \delta \geq 0 \end{cases} \\
\sigma_1 &= 0.55 \\
\mu_2 &= -0.9 \\
\sigma_2 &= \begin{cases} 0.28 & \forall \delta \leq -1 \\ 0.28 - 0.1636(\delta + 1) & \forall -1 < \delta < 0.1 \\ 0.1 & \forall \delta \geq 0.1 \end{cases}
\end{aligned}
\tag{4.7}
$$

These functions were implemented by the MIT MOCAT team as:

$$\frac{A}{m} = 10^{\alpha x_1 + (1-\alpha) x_2} \tag{4.8}$$

$$x_1 = \mu_1 + \sigma_1 * \text{randn}(n) \tag{4.9}$$

$$x_2 = \mu_2 + \sigma_2 * \text{randn}(n) \tag{4.10}$$

where randn(n) is MATLAB's random number generator. Then the effective area of the fragments is taken proportionally to the fragment diameter as [26]:

$$
\begin{aligned}
A_{\text{eff}} &= \begin{cases} 0.540424\, d^2 & \forall d < 1.67 \text{ mm} \\ 0.556945\, \hat{d}^{\,2.0047077} & \forall d \geq 1.67 \text{ mm} \end{cases} \\
\hat{d} &= d/1 \text{ m}
\end{aligned}
\tag{4.11}
$$

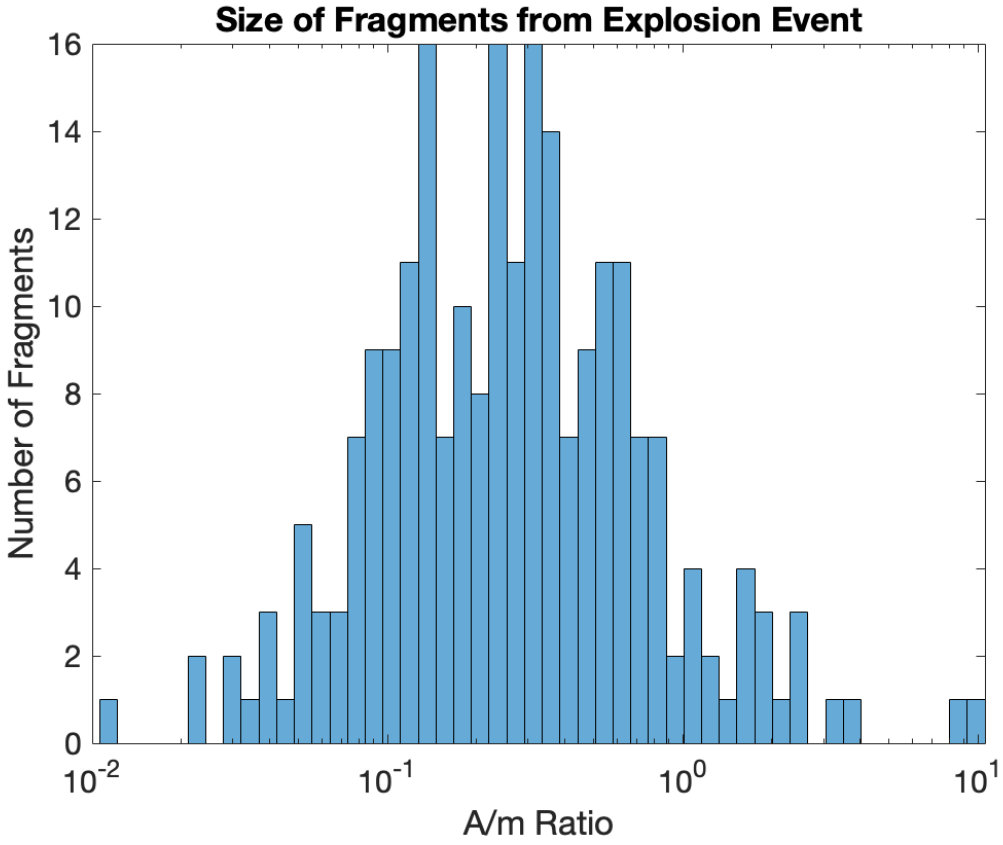

Figure 4-13: Area (m^2) to mass (kg) ratio of fragments after an explosion of a rocket body with 233 debris fragments generated.

and the mass is derived from this effective area as $m = \frac{A_{\text{eff}}}{A/m}$. This method to calculate the area-to-mass ratio was implemented in reference [28]. A rocket body explosion with mass and area given by the species characteristics described in Section 4.1 is considered. Using the methods described above, the computed area-to-mass ratios of the produced fragments are displayed in Figure 4-13. The mean area-to-mass ratio is 0.508 m^2/kg whereas Section 4.1 gives an area-to-mass ratio of 0.03 m^2/kg for the debris species. The source-sink model assumes all fragments produced in the explosion are members of the debris species. It is important to note that the mean area-to-mass ratio of fragments produced from a rocket body explosion differs from explosions of other species. However, representing all such fragments by one set of characteristics for the debris species marks a limitation of the simplified MOCAT-3 or MOCAT-4B model.

The imparted fragmentation velocities are computed using the NASA Standard Breakup model following a normal distribution [26]:

$$\rho(\nu) = \frac{1}{\sigma\sqrt{2\pi}} e^{-(\nu-\mu)^2/(2\sigma)} \tag{4.12}$$

where $\chi = \lg(A/m)$ and $\nu = \lg \Delta v$. The mean value μ_ν and standard deviation σ_ν depend on whether the fragmentation event is a collision or explosion. For explosions, the parameters are:

$$\mu_v = 0.2\chi + 1.85 \tag{4.13}$$

$$\sigma_v = 0.4 \tag{4.14}$$

The MOCAT team at MIT implemented the calculation for the imparted velocity as:

$$\Delta v = 10^{\mu+\sigma*\mathrm{randn}(n)} \tag{4.15}$$

where randn(n) is MATLAB's random number generator. These functions are applied to each area-to-mass ratio of the debris to find the magnitude of the imparted velocity resulting from the explosion. Since only debris fragments larger than 0.1 m are considered for this analysis, the NASA Breakup Model for fragments below 1 mm was not used.

The direction of the imparted velocity is randomly sampled on the unit sphere. An example of the magnitude of the imparted velocity and the dispersion of 233 fragments for a rocket body with species characteristics given in Section 4.1 is shown in Figures 4-14 and 4-15. This is the dispersion of fragments in the reference frame of the rocket body. The imparted velocity is added to the velocity of the rocket body. Since the distributions use a random number generator, the exact dispersion of fragments varies for each explosion; however, the magnitude of the velocity follows the normal distribution described above.

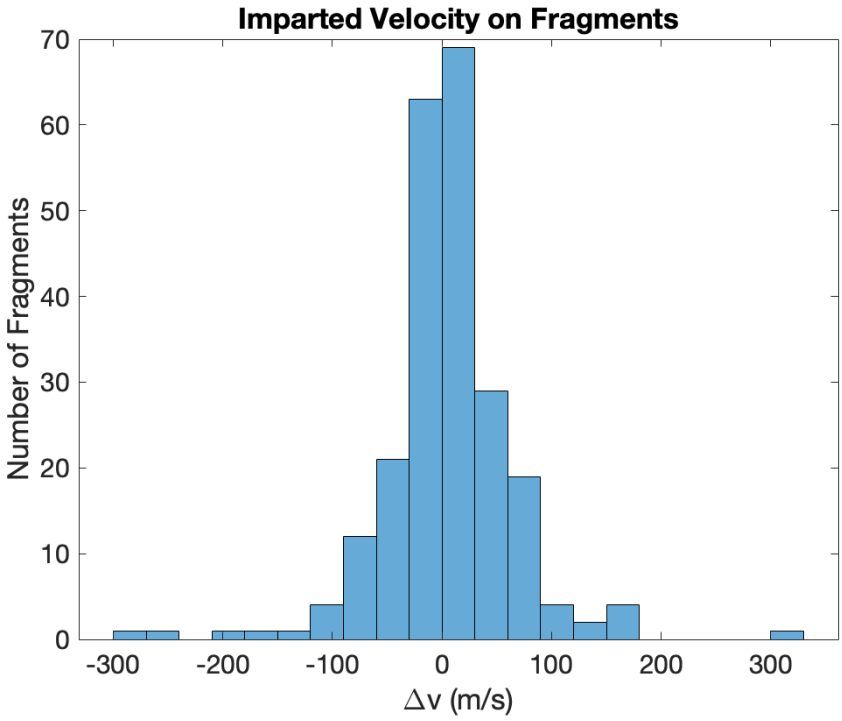

Figure 4-14: Imparted velocity distribution after an explosion of a rocket body with 233 debris fragments generated.

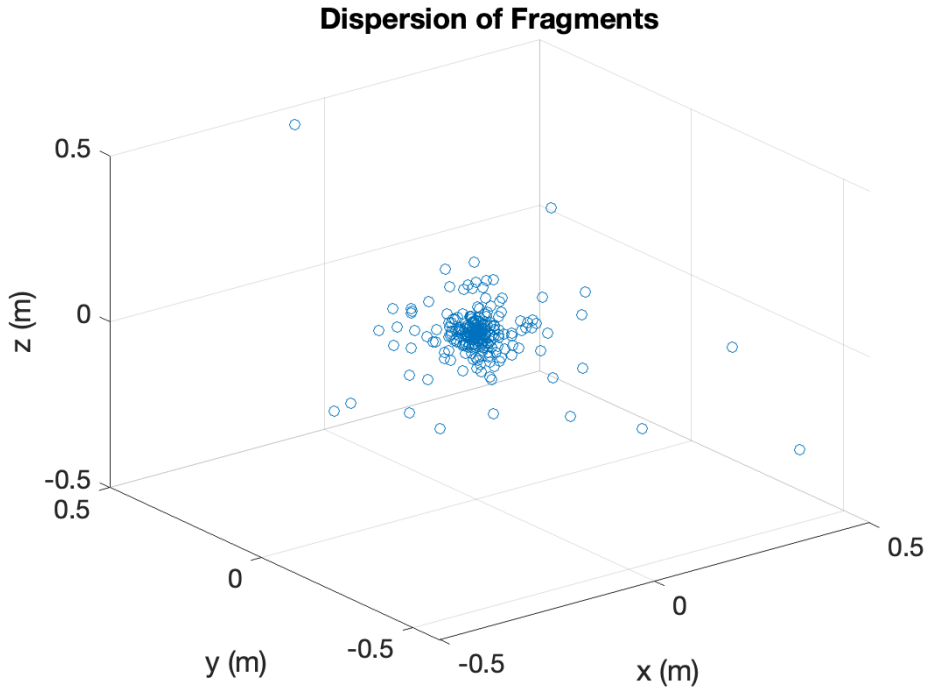

Figure 4-15: Fragment distribution 1 second after an explosion of a rocket body with 233 debris fragments generated.

4.4.2 Evaluating Assumption of Shell-Bound Fragmentation Events

Here the methodology is given for testing the source-sink model's assumption that all fragments remain in the same shell where the original object existed before an explosion occurred. A simulation was constructed to mimic a rocket body explosion event in LEO. The rocket body took on the species characteristics given in Section 4.1. The explosion was assumed to occur while the rocket body was in a circular equatorial orbit at an altitude of 525 km, positioning the rocket body in the center of the $500-550$km shell in the source-sink model. A shell width of 50 km is a commonly used width for MIT's source-sink model [15]. The dispersion model covered in Section 4.4.1 was implemented with the SGP4 propagator to simulate the evolution of fragments. The fragments were not bounded to reside within the shells. Atmospheric drag effects on the debris fragments were included in the propagation. The simulation was run for various lengths of time. Then the fragments were binned into the 50km wide shells to assess what fraction of fragments remain in the same shell as the rocket body. Figure 4-16a shows the fragments 10 minutes after the explosion event. Figure 4-16b shows fragments 10 days after the explosion event. A total of 33.9% of fragments resided outside of the shell where the rocket body exploded after just 10 minutes, whereas after 10 days 53.2% of fragments reside outside of the original shell. Within the 10 day simulation, 8 fragments de-orbited. The trajectories of the dispersed fragments depend on their eccentricities. Compared to the circular trajectory of the rocket body with eccentricity 0, the fragments have a range of eccentricity values as shown in Figure 4-17.

Through this analysis, it can be seen how a cloud of debris evolves for an explosion of an object of the rocket body species. This is one example of the limitation of the source-sink model using shell binning. A possible adaptation that could be made to the model is to disperse the fragments into neighboring shells. More simulations would need to be set up to compute the share of fragments in neighboring shells after an explosion event, including simulations in which the exploding object is placed at

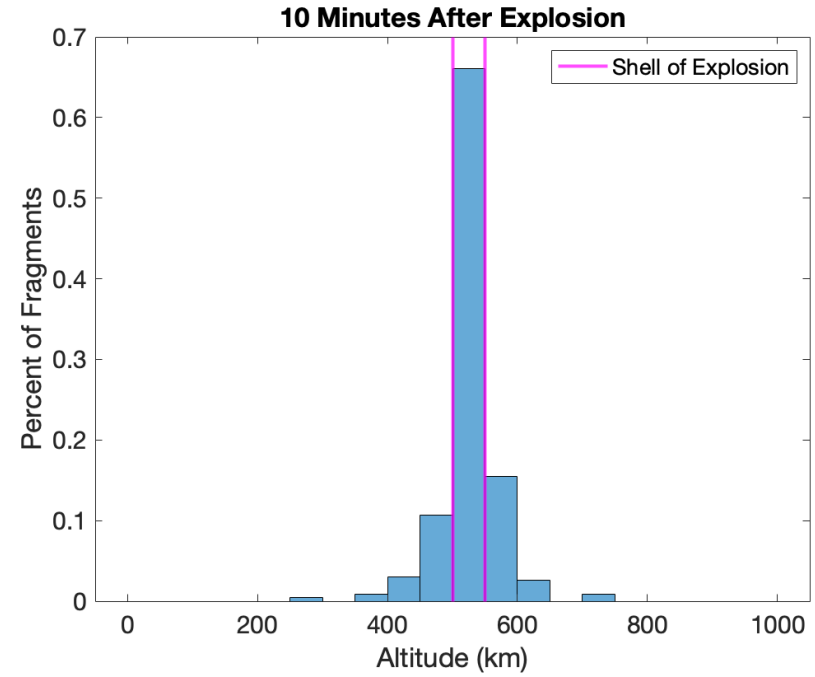

(a)

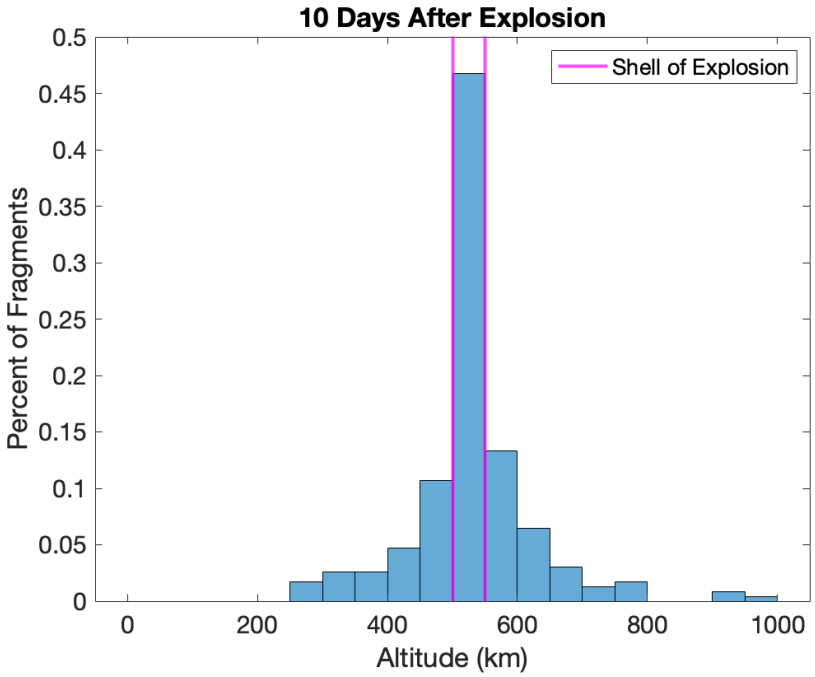

(b)

Figure 4-16: Simulation of debris evolution from rocket body explosion at various times.

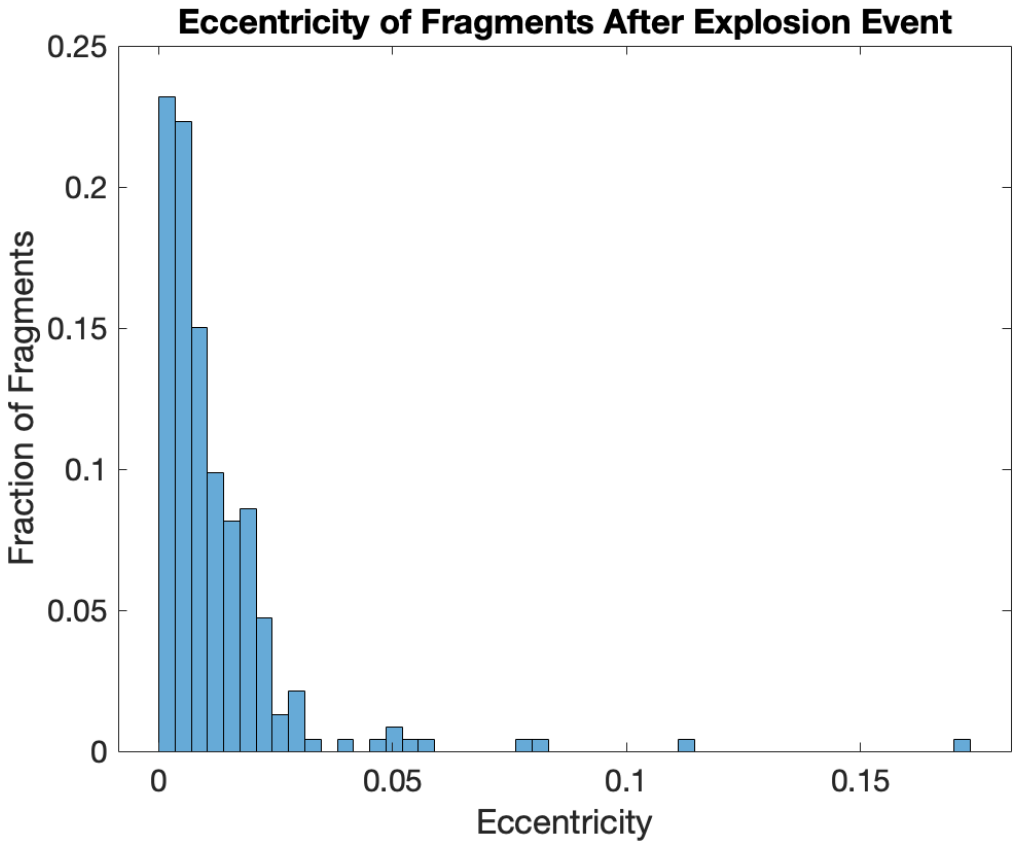

Figure 4-17: Eccentricity of fragments from rocket body explosion event.

various altitudes within the shell to analyze the effect of the shell edge placement. The dispersion of fragments would need to be computed for a specified time after the explosion before atmospheric drag greatly effects the trajectories.

4.5 Simulations: Validation with ESA's DELTA

Given some of the limitations of the MOCAT-SSEM model as explored in 4.4.2, it is important to validate the model against predictions of other models in the literature. MOCAT-SSEM computes the evolution of the orbital environment faster than higher-fidelity Monte-Carlo models. The source-sink model's predictions need to be validated against higher-fidelity models such as the Debris Environment Long Term Analysis (DELTA) model developed by the European Space Agency (ESA)[60]. Furthermore, the basic assumptions and functionalities of the source-sink model should align with the Monte Carlo model. To ensure the precision of the model predictions, nearly identical simulations were run using the MOCAT model and ESA's DELTA model and their outcomes were compared. A No-Further Launch (NFL) case and an extrapolated launch case are two distinct simulations used to compare MOCAT's predictions to ESA's DELTA predictions of the future orbital environment. The simulations using MOCAT-4B were run with and without the proposed explosion model in Section 4.2 and the improved PMD model introduced in Section 4.3 to see if the changes in the model created greater convergence in the predictions about the orbital environment's evolution over time.

4.5.1 Initial Population and Launch Rate

The initial population for each species was computed from the DISCOS database by binning the objects according to the categorization displayed in Figure 4-1. The initial population for the year 2022 is displayed in Figure 4-18. The launch rates used in the simulation runs for MOCAT-4B were created using a historical launch rate and planned constellations. The historical launch rate was calculated by taking the average of the last 5 years of launches from 2017 to 2021; this method of computing

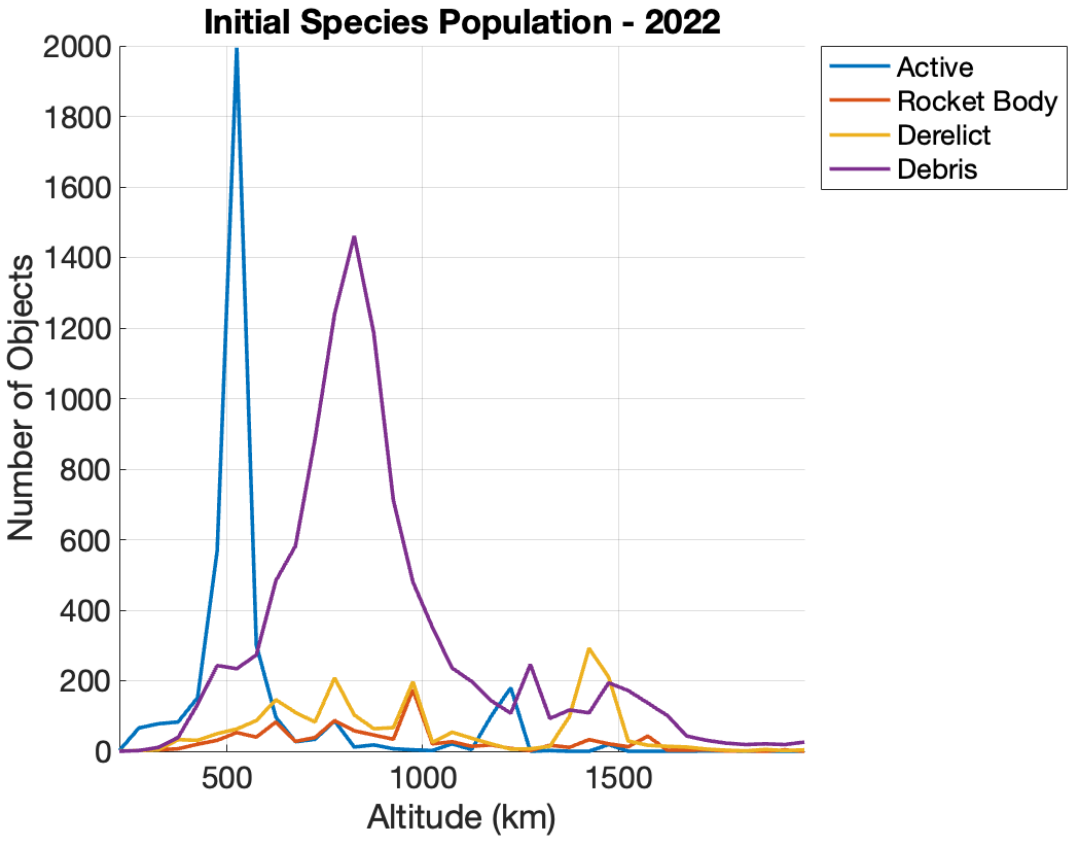

Figure 4-18: DISCOS 2022 initial population.

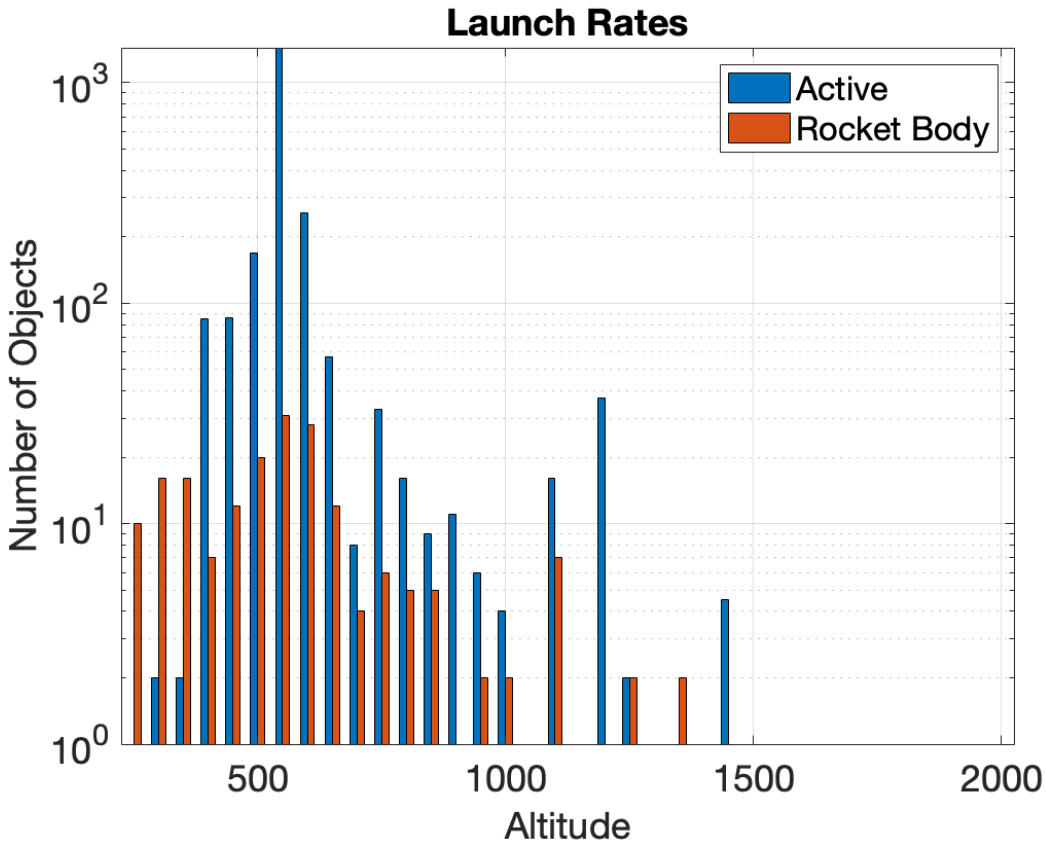

Figure 4-19: Launch traffic input for MOCAT-4B.

a launch rate is based on ESA's method of repeating the last 5 years of launches [17]. The constellations were added similarly to how constellations are added in ESA's DELTA model for an extrapolated launch case wherein only constellations that have launched a satellite in the past are included in the future launch traffic. Launch rates are only considered for active satellites and rocket bodies. There is no launch traffic for derelict satellites or debris. The launch traffic used for MOCAT-4B is shown in Figure 4-19.

4.5.2 Simulation Parameters

Simulation parameters can greatly affect the dynamics of species interactions and the predicted number of objects in orbit. Parameters were chosen to closely match ESA's DELTA model parameters. A few adjustments had to be made when im-

Table 4.3: Input Parameters for Simulation Comparisons with ESA's DELTA Simulations.

Parameter	NFL	Extrapolated Launch
Number of Shells	36	36
Shell Thickness	50 km	50 km
Min Altitude	200 km	200 km
Max Altitude	2000 km	2000 km
Lifetime	8 yrs	8 yrs
P	0.3	0.4
PMD_t	25 yrs	25 yrs

plementing ESA's DELTA model parameters since the capabilities of DELTA and MOCAT-SSEM are different. The PMD duration (PMD_t), probability of successful PMD (P), and collision avoidance maneuvers are specified separately for constellations and active payloads, whereas in the MOCAT-4B model, all active payloads, including satellite constellations, are modeled as active species members. Two sets of simulation parameters are used; one for the No-Further Launch (NFL) case and one for the Extrapolated Launch case. A list of all input parameters is given in Table 4.3. The Lifetime parameter is the number of years that a satellite is active before it becomes derelict. The minimum size of the trackable objects considered in both models is 0.1 m. These parameters were chosen to match those of the DELTA simulations, however, the extrapolated launch case for DELTA specifies a different probability of successful PMD for constellations compared to the rest of the objects. This value for constellations modeled in DELTA is $P = 0.9$. Since satellite constellations are not differentiated from other active satellites, the same probability of successful PMD was used for all active satellites in MOCAT-4B, namely $P = 0.4$. The following simulations made use of the updated species characteristics given in Section 4.1 as these were calculated from the same database used in the DELTA simulations.

4.5.3 MOCAT-4B NFL Case

The NFL case allows for a comparison between models without the influence of how to launch traffic is implemented in each model. The initial population is set as given

Table 4.4: Final Populations Predicted by Simulations.

Model	NFL	Extrapolated Launch
ESA DELTA	45,000	165,000
MOCAT-4B v1	17,000	935,000
MOCAT-4B v2	22,000	445,000

in Section 4.5.1. The launch traffic is set to 0 for all years of the simulation. The NFL simulations run using MOCAT-4B are displayed in Figure 4-20 with and without the explosion model and the improved PMD model. The evolution of each species follows the same trends in both Figures 4-20a and 4-20b, however, the final population after a 200-year simulation is larger with the implemented features. Although the new PMD model would cause a decrease in the number of rocket bodies over time, this has a minimal effect when no future launches take place. On the other hand, the implemented explosion traffic continues to generate new debris fragments leading to a larger total population over time. This simulation can be compared to ESA's DELTA simulation depicted in 4-21. The trends in the total population are the same for the DELTA simulations and the MOCAT-4B, however, MOCAT-4B predictions have a decrease in the total population for approximately 25 years before the population begins to increase again; this decrease is not present in the DELTA simulations. The evolution of the density of each species population per altitude shell with the improved MOCAT-4B model is displayed in Figure 4-22. It is evident that the active, derelict, and rocket body population density decreased over time whereas the debris population density increased. This effect is due to the explosion and PMD model which remove members of these species and create new debris fragments. The total density evolution is displayed in Figure 4-23 where it is evident that the overall density of the orbital environment increases over time due to the increase in debris fragments. The final total populations of resonant space objects with and without the new implementation compared to ESA's DELTA prediction is shown in Table 4.4. ESA's DELTA simulations for the NFL case is displayed in Figure 4-21.

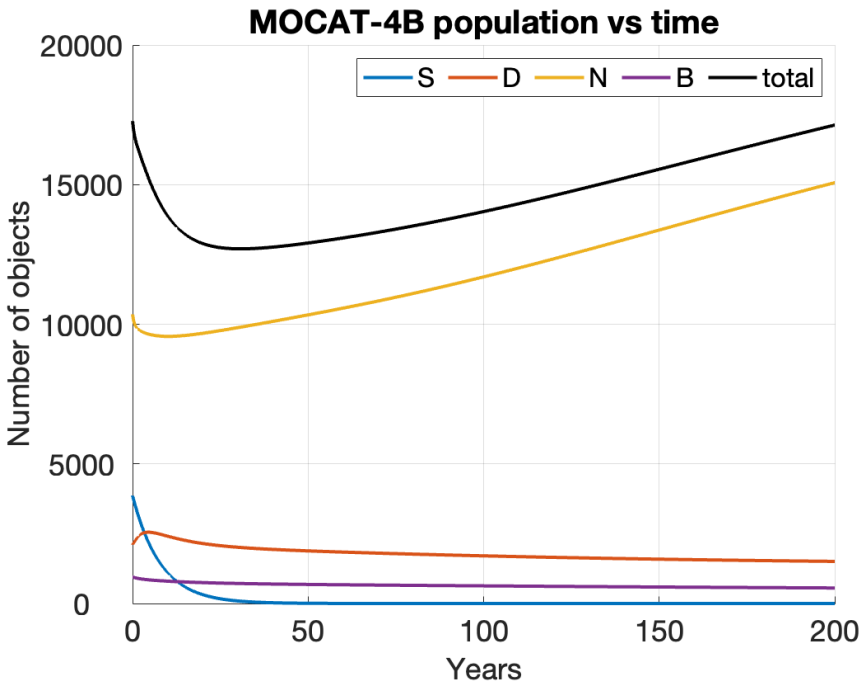

(a) No explosions and Old PMD model.

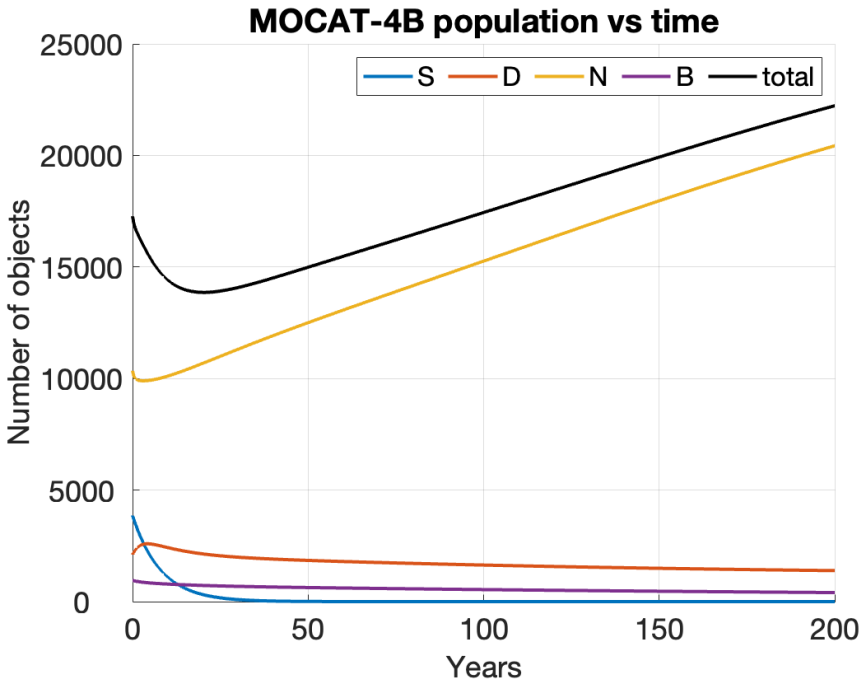

(b) With explosions and new PMD model.

Figure 4-20: NFL Simulations with MOCAT-4B

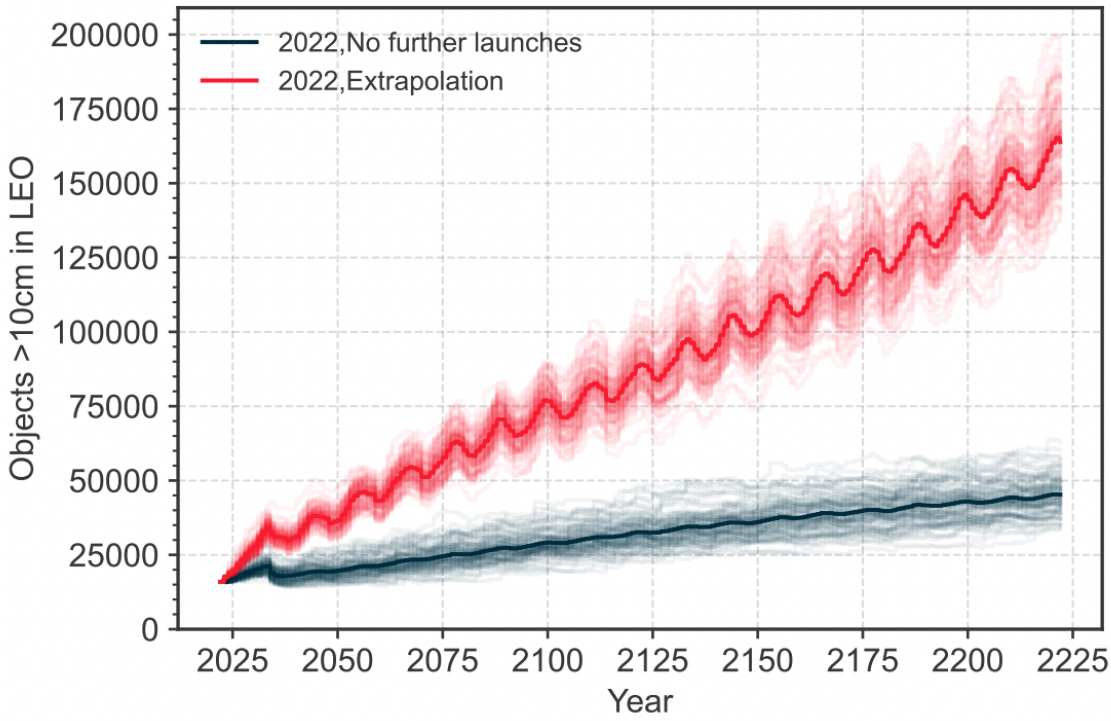

Figure 4-21: Simulations run by ESA using the DELTA model [17].

4.5.4 MOCAT-4B Extrapolated Launch Case

The extrapolated launch case allows for a comparison of model predictions wherein the population of resonant space objects is increasing over time due to continued launches. The greatest effect of an increased population in LEO is how this leads to an increase in fragmentation events since both the collision model and the newly implemented explosion model are directly proportional to the populations of species. The change in each species' population per altitude shell is displayed in Figure 4-25, which better depicts how the population evolution is altitude dependent. There is a build-up of derelict satellites in the $1200 - 1250$ km shell and a build-up of rocket bodies in the $1100 - 1150$ km shell. This build-up causes increased debris growth over time as these objects collide or explode and create new fragments that do not sink into lower altitudes because the atmosphere has a low density at these altitudes. This increase in fragments can be seen most clearly in Figure 4-26. This simulation can again be compared to ESA's DELTA simulation depicted in 4-21. The final total populations

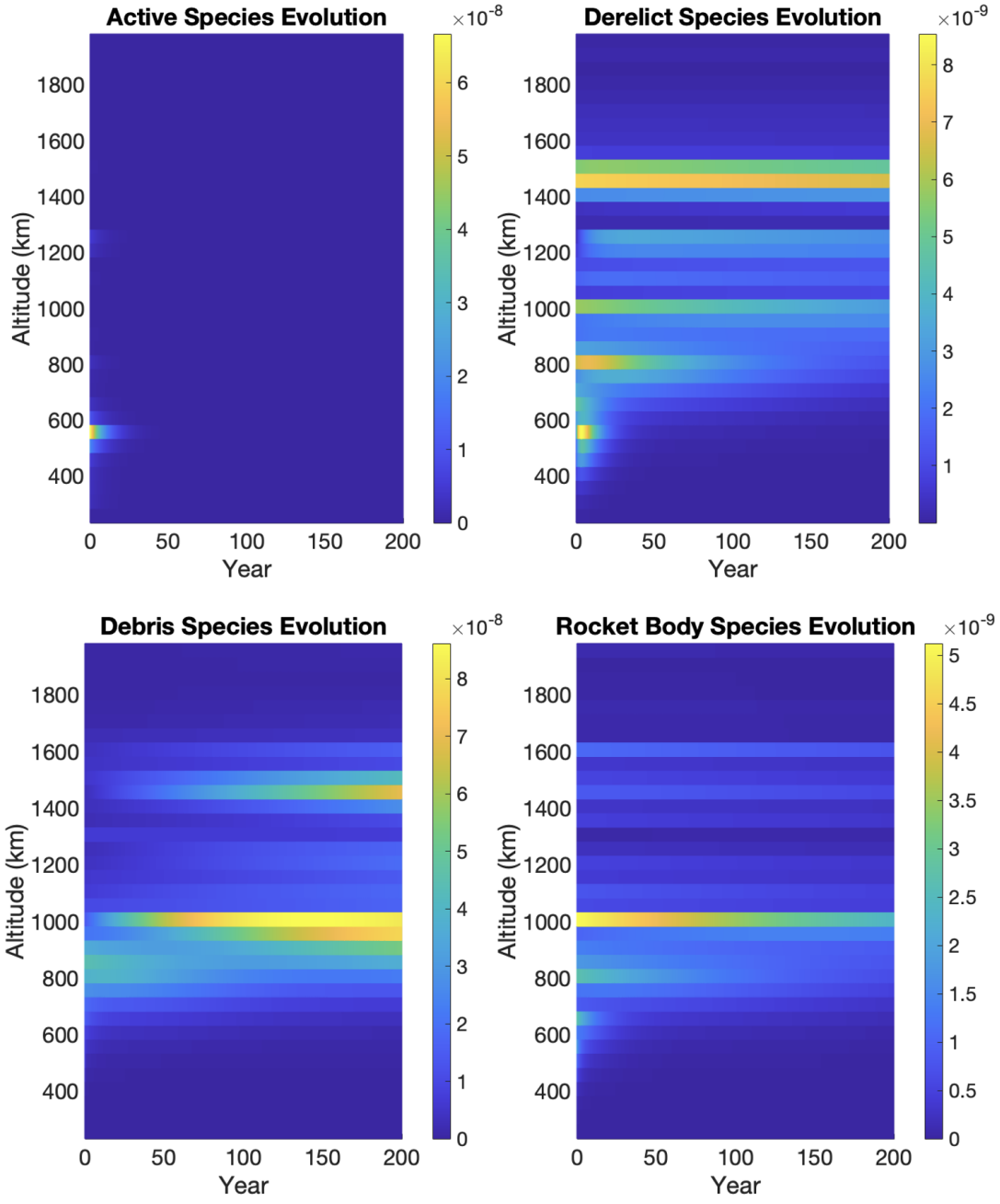

Figure 4-22: MOCAT-4B NFL simulation: Evolution of the density of objects per species per shell.

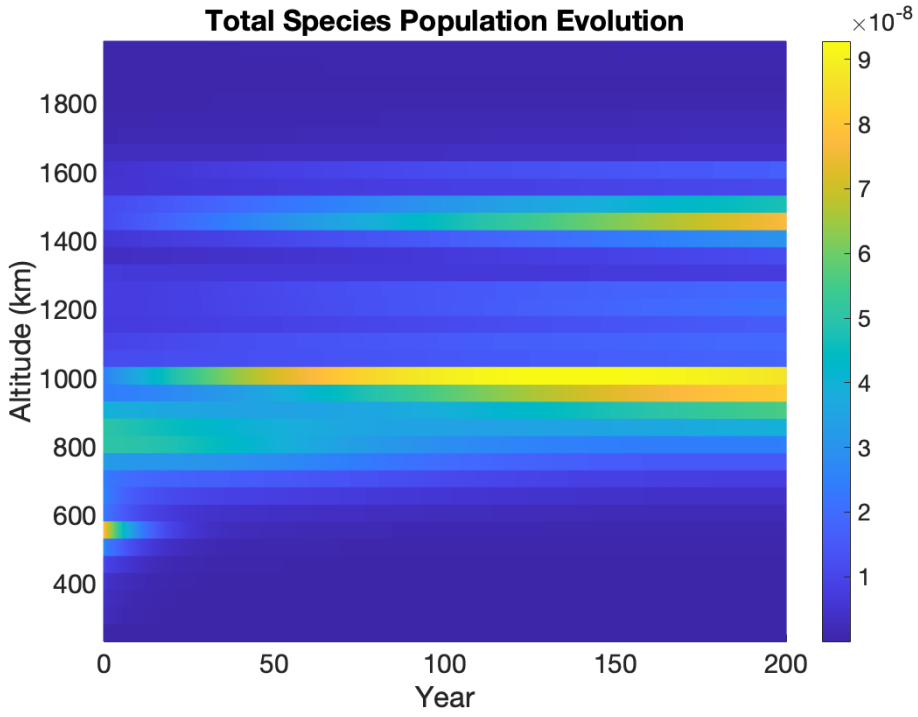

Figure 4-23: MOCAT-4B NFL simulation: Evolution of the density of the total population per shell.

of resonant space objects with and without the new implementation compared to ESA's DELTA prediction are shown in Table 4.4.

4.5.5 Discussion of Validation Simulations

In both cases, the improved model showed greater convergence with DELTA's predictions. The overall trends of each simulation run matched, and the final population of resonant space objects was found to be within the same order of magnitude for a 200-year simulation duration. In the NFL case, the implemented explosion model lead to a greater total population at the end of the 200-year simulation compared to the previous version of MOCAT-SSEM. The predicted total population was within the same order of magnitude albeit being lower than DELTA's predicted total population by $23,000$ objects. In the extrapolated launch case, the improved PMD model, specifically for rocket bodies, lead to a lower total population after 200 years compared to the previous version of MOCAT-SSEM. The predicted total population was approximately 2.7 times higher than DELTA's prediction of $165,000$ objects, however this is an improvement of the first version of MOCAT-4B which predicted 5.7 times higher than DELTA's model. Overall, the improvements to the MOCAT-4B model caused the model's predictions to be more convergent with DELTA's predictions. Further validation work could include more validation cases using different launch rates and model parameters.

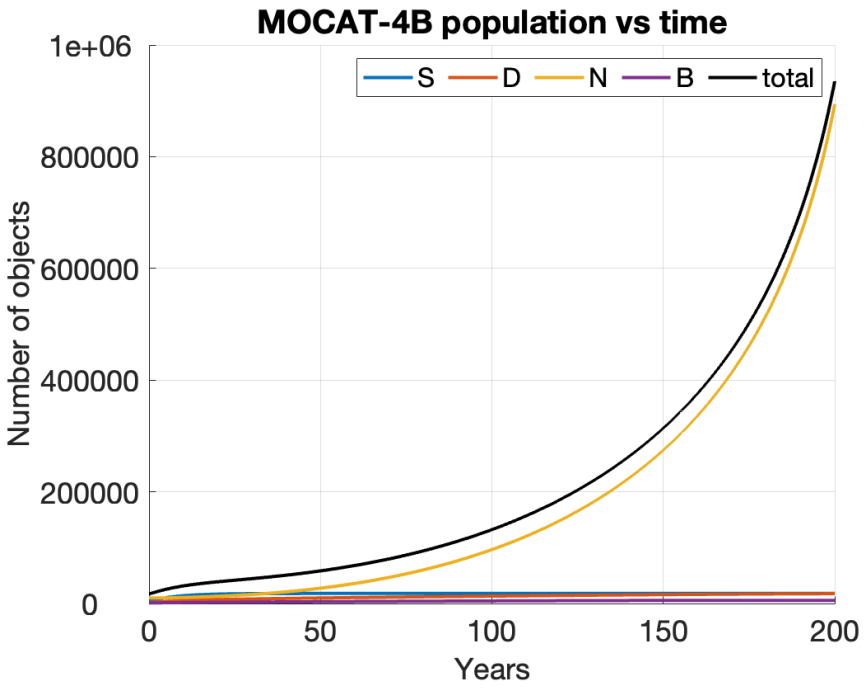

(a) No explosions and Old PMD model.

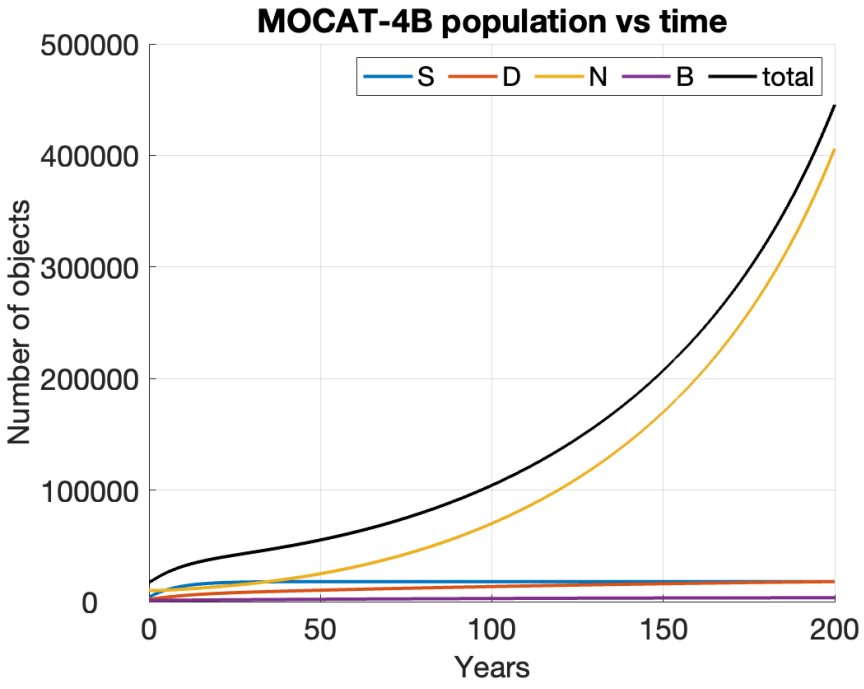

(b) With explosions and new PMD model.

Figure 4-24: Extrapolated Launch simulations with MOCAT-4B.

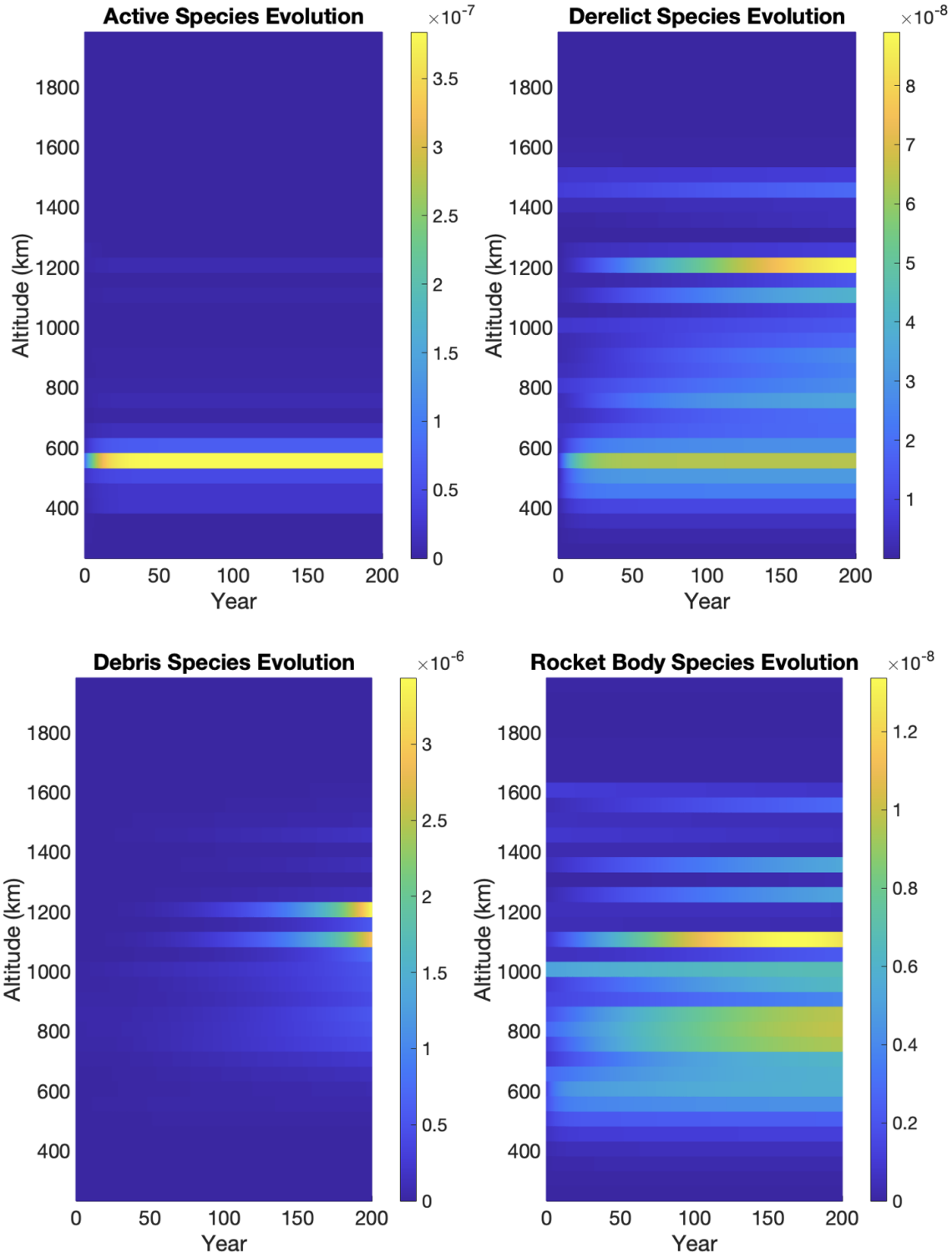

Figure 4-25: MOCAT-4B Extrapolated Launch simulation: Evolution of the density of objects per species per shell.

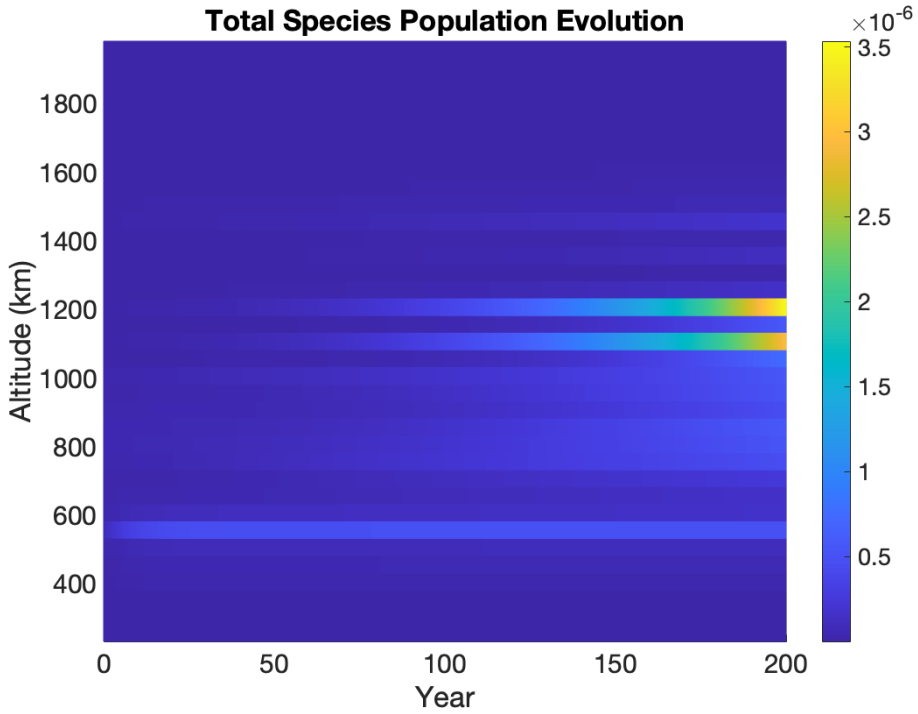

Figure 4-26: MOCAT-4B Extrapolated Launch simulation: Evolution of the density of the total population per shell.

Chapter 5

Cis-lunar Debris Evolution

Having studied the effect of accidental explosion events in LEO, it is of interest to apply the explosion analysis to other regions of space. Upcoming return missions to the Moon such as Artemis [7], call for an analysis of the effect of accidental fragmentation events in cis-lunar space. In this chapter, the dispersion and evolution of fragments from explosion events are studied in cis-lunar space for a particular mission and an assessment of the risk posed by such events to future missions is given.

5.1 Overview of Case-Study

Analyzing fragmentation events in cis-lunar space allows for an assessment of the short and long-term effects of debris in the Earth-Moon system. Since there are few space missions planned for cis-lunar space, the chance of collisions between spacecraft is low. However, accidental explosion events could be triggered by a spacecraft or rocket body that would generate a large amount of debris. It is insightful to analyze the evolution of debris fragments after such an event has occurred and study whether the fragments pose a threat to space missions.

In this chapter, a specific mission is chosen to analyze the effects of a possible explosion event occurring along the mission's trajectory. The chosen mission is Gateway, a space station in lunar orbit that will support human space exploration [47]. The lunar Gateway is made up of several modules as depicted in Figure 5-1. Fragmen-

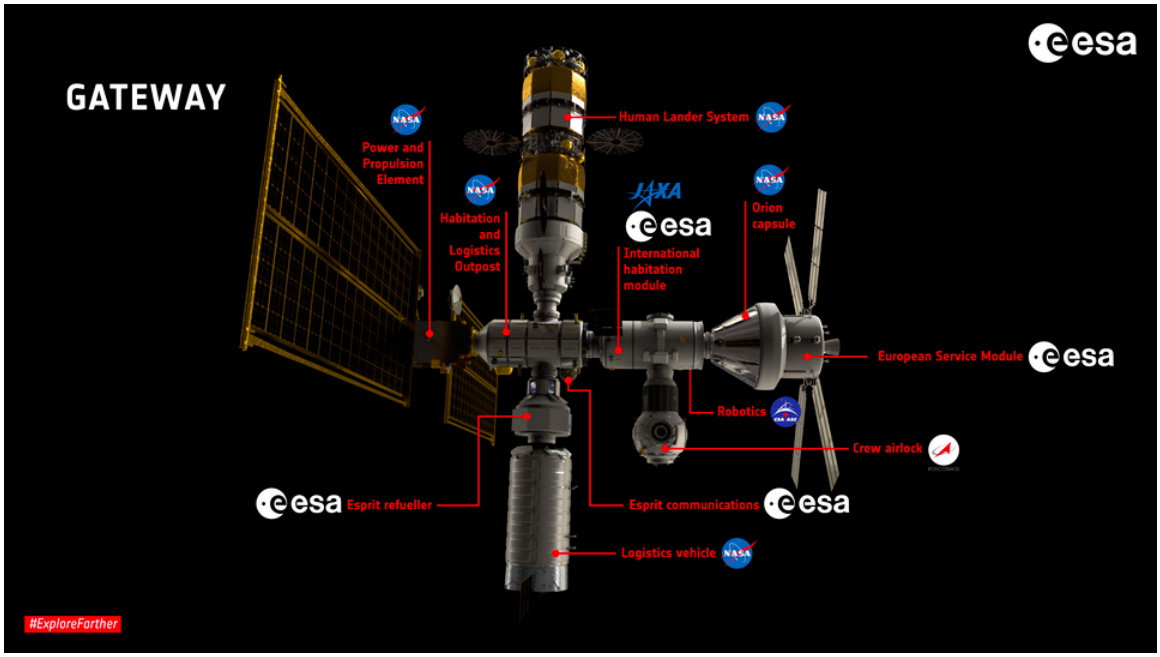

Figure 5-1: Modules of the Lunar Gateway [36].

tation events near Gateway could be extremely dangerous as it is expected to house up to 4 astronauts at a time. This space station is to be placed in a Near-Rectilinear Halo Orbit (NRHO) about the Moon with its closest approach being above the north pole of the Moon [9]. The orbit's perilune radius is 3,366 km and its apolune radius is 70,000 km [31]. This orbit is a member of the southern orbit families of the L2 halo orbits with a 9:2 lunar synodic resonance [64]. The 9:2 ratio signifies that for every 2 lunar months, there are 9 orbit revolutions [31]. The average period of the orbit is 6.56 days. The following sections will explore the evolution of space debris generated from an explosion event occurring along the Lunar Gateway's orbit.

5.2 CR3BP and Debris Analysis

5.2.1 Explosions in CR3BP

The trajectory of the simulated spacecraft is analyzed in the context of the circular restricted three-body problem (CR3BP) [51] and thus assumes the mass of the spacecraft in orbit is negligible compared to the mass of the Earth and the Moon. An

additional assumption of the CR3BP frame is that no other masses are considered in the model such as the Sun. The equations of motion describing the satellite's trajectory in the CR3BP rotating frame are [24]:

$$\begin{aligned} \ddot{x} - 2\dot{y} &= -\frac{\partial \tilde{U}}{\partial x} \\ \ddot{y} + 2\dot{x} &= -\frac{\partial \tilde{U}}{\partial y} \\ \ddot{z} &= -\frac{\partial \tilde{U}}{\partial z} \end{aligned} \tag{5.1}$$

The rotating frame is used to have the Earth and Moon remain fixed where the center of rotation is the barycenter, and here the frame is shifted so that the Moon is at the origin. The potential $\tilde{U}$ accounts for gravitational and centrifugal forces:

$$\tilde{U} = -\frac{1}{2}\left[(1-\mu)r_1^2 + \mu r_2^2\right] - \frac{1-\mu}{r_1} - \frac{\mu}{r_2} \tag{5.2}$$

with r_1 and r_2 being the distance from the Earth and Moon respectively, and $\mu = m_2/(m_1 + m_2)$ represents the ratio of the masses of the Earth (m_1) and Moon (m_1). The time used in this system of equations is normalized by the synodic time and the distances are normalized by the distance between the Earth and Moon. The synodic time is the amount of time in seconds that the Moon takes to orbit around the Earth. The simulation of fragmentation events along the reference orbit using the explosion model of Section 4.2, and in particular, the dispersion of fragments as given in Section 4.4.1 was added in the CR3BP frame. Figure 5-2 displays the reference NRHO on which fragmentation events will be considered[1].

The imparted velocity $\Delta\vec{v}$ from the fragmentation event is added to the velocity of the spacecraft in the CR3BP reference frame as:

$$\vec{v}_f = \vec{v}_i + \Delta\vec{v} \tag{5.3}$$

where $\vec{v} = [\dot{x}, \dot{y}, \dot{z}]$. A hypothetical scenario of a piece of debris with $\Delta v = [0.01, 0.01, 0.01]$

[1]The code used for computing the NRHO in the CR3BP frame was developed by Post-Doctoral Associate Pablo Machuca.

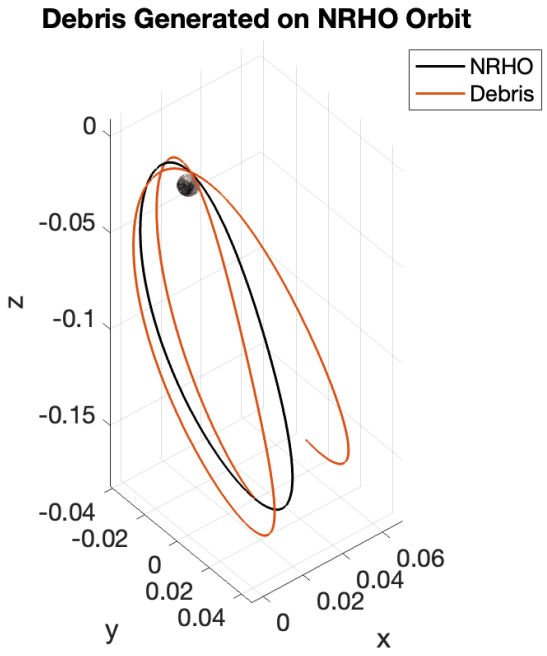

Figure 5-2: Simulated debris fragmenting off of a spacecraft in NRHO orbit where distances are normalized by the Earth-Moon distance.

in non-dimensional units in the CR3BP frame is ejected from NRHO at the southern point. The evolution of the debris over two NRHO periods is shown in Figure 5-2. The debris fragment crosses the NRHO twice which could cause a collision if the spacecraft is still traveling along its original trajectory. For different Δv and durations in orbit, the fragments will travel along different trajectories. The methods employed to analyze the trajectories of a cloud of debris are described next.

5.2.2 Methods for Assessing Debris Evolution

Here, the explosion of one of the modules of the Lunar Gateway is considered. The effect of the explosion on the other modules is not assessed as this is highly dependent on the safety mechanisms employed. Thus, only the evolution of the debris from the explosion of one module is computed. The reference size and mass of the exploding module are chosen to mimic the ESPRIT refueling module [20] which will carry fuel and is thus considered more likely to explode than other modules such as the

International Habitation Module. The size of the ESPRIT refueling module is 4.6 m in diameter, and 6.4 m in length, and holds a total mass of 10 tonnes when it is filled with fuel [56]. The cross-sectional area considered in the explosion model is a circle with a diameter of 4.6 m and the mass considered is $7,500$ kg to mimic a partially filled fuel tank.

To analyze the trajectories for an explosion creating numerous debris fragments, the trajectories of each are analyzed to see if the debris:

1. Impact the Moon
2. Enter the GEO region
3. Remain within $10,000$ km of the NRHO 9:2 southern orbit
4. Located more than 1.5μ from the barycenter.
5. Other

Recall μ is the distance from the Earth to the Moon. These five categories are used to represent the behaviors of the debris fragments at various instances of time. The first category impacts to the Moon, are of interest as they could cause a risk to future lunar missions and habitats. A fragment is considered to have impacted the Moon if its trajectory passes within the Moon's radius. The second category depicts whether the debris fragments could collide with satellites orbiting Earth in the GEO region or below. A fragment is considered to be a threat to GEO if it passes through the altitudes of 36,300 km since that is the approximate region of GEO satellite graveyard orbits. The third category allows for an estimate of how many debris fragments remain near the initial reference orbit that could cause collisions with a spacecraft in NRHO. A fragment is considered to be "near" the initial NRHO if it comes within $10,000$ km of the reference NRHO orbit. The fourth category is used to study how many debris fragments go beyond the Earth-Moon system. The fifth category encompasses fragments that are in regions in between those covered by the previous categories, such as beyond GEO but not outside of the region defined by

the fourth category. Fragments that fall into this category pose a potential threat to missions residing in these regions of cis-lunar space and may, for longer simulation times, change categories. Out of the 5 categories, category 4 is considered as the only favorable scenario since debris fragments that satisfy this category pose a minimal risk to space missions.

Trajectory Analysis

The trajectory of each fragment produced in the explosion is evaluated separately to see which category it satisfies during the simulation. To find whether a fragment satisfied criteria 1 or 2 in List 5.2.2, the position of closest approach was calculated between the fragment and the chosen reference point represented by (x_o, y_o, z_o). The closest approach distance was computed according to Algorithm 1[2]. Using Algorithm

Algorithm 1 Calculate Closest Approach

Require: Fragment trajectory positions (x_i, y_i, z_i), Reference Point (x_o, y_o, z_o)
Ensure: Minimum distance $d_{\min}$ and corresponding index idx
1: Initialize an empty list, *distances*
2: **for** each position i along the fragment's trajectory **do**
3: Calculate the Euclidean distance from the reference point to the position:
4: $distance = \sqrt{(x_o - x_i)^2 + (y_o - y_i)^2 + (z_o - z_i)^2}$
5: Append *distance* to *distances*
6: **end for**
7: Find the minimum value, $d_{\min}$, and corresponding index, idx, in *distances*

1 and taking (x_o, y_o, z_o) to be either the center of the Moon or of the Earth, the following logic was used to determine whether a fragment has impacted the Moon or entered the GEO region:

$$\begin{cases} \text{Impacted Moon,} & \text{if } d_{\text{min, Moon}} < R_{\text{Moon}}, \\ \text{Entered GEO region,} & \text{if } d_{\text{min, Earth}} < (R_{\text{Earth}} + 36,300\text{km}). \end{cases} \tag{5.4}$$

To find whether a fragment satisfied criteria 3 in List 5.2.2, the furthest position was calculated between the fragment and the reference NRHO by calculating the

[2]Code for finding the position of closest approach was developed by Post-Doctoral Associate Pablo Machuca at MIT.

distance between every point on the fragment's trajectory and every position along one revolution of the NRHO. Then the maximum of these distances was found. The furthest distance was computed according to Algorithm 2. The following condition

Algorithm 2 Calculate Furthest Distance

Require: Fragment trajectory positions (x_i, y_i, z_i), NRHO positions (x_j, y_j, z_j)
Ensure: Maximum distance $d_{\max}$ and corresponding index idx
1: Initialize an empty list, *distances*
2: **for** each position i along the fragment's trajectory **do**
3: **for** each position j along the NRHO **do**
4: Calculate the Euclidean distance from the NRHO position to the fragment position:
5: $distance = \sqrt{(x_j - x_i)^2 + (y_j - y_i)^2 + (z_j - z_i)^2}$
6: Append *distance* to *distances*
7: **end for**
8: **end for**
9: Find the maximum value, $d_{\max}$, and corresponding index, idx, in *distances*

was used to determine whether a fragment remained within 10,000 km of the NRHO:

$$\begin{cases} \text{Remained within 10,000 km of the NRHO,} & \text{if } d_{\max,\ \text{NRHO}} < 10000. \end{cases} \tag{5.5}$$

To determine whether a fragment satisfied criteria 4 in List 5.2.2, the set of positions of the fragment over the last period was compared with the barycenter. This was quantified as follows:

$$\begin{cases} \text{Located more than } 1.5\mu & \text{from the barycenter,} \\ & \text{if all points within the last period exceed a} \\ & \text{distance of } 1.5\mu \text{ from the barycenter.} \end{cases} \tag{5.6}$$

Finally, if the fragment's position does not satisfy any of the criteria described above, it is considered to have satisfied criteria 5 in List 5.2.2. The evolution of the debris fragments is considered for various durations. These durations are given as multiples of the reference NRHO period.

5.3 Fragmentation Analysis in NRHO

A fragmentation event is considered at the southern point of the NRHO. A cloud of debris is created and evolved for 2, 5, 10, and 20 NRHO periods. An example of the behavior of 4 randomly selected debris fragments is displayed in Figure 5-3. Figure 5-4 displays the percent of fragments that satisfy each of the criteria listed in 5.2.2. In this simulation, 1 debris fragment impacted the Moon within 2 periods of the explosion event. The other 3 fragments evolved in the region between the Moon and Earth for at least 2 periods, with one fragment remaining in this region for 20 periods whereas 2 fragments had trajectories that went beyond a distance of 1.5μ from the barycenter. This is an example of the evolution of 4 debris fragments; a simulation of all debris fragments from the explosion is explored next.

Since there is randomness in the exact number of fragments and direction of fragments produced in the explosion as explained in Section 4.2, 100 simulations were used in order to depict the mean evolution of debris fragments from the southern point of the reference NRHO. Figure 5-5 displays the mean number of fragments that satisfy each category as the system evolves for 2, 5, 10, and 20 NRHO periods. Figure 5-6 displays the standard deviation for the mean values. A mean of 237.18 debris fragments was produced in the explosions. Within the first 2 periods of the simulation, the largest fraction of debris resides in the 'other' regions not covered by the first 4 categories in 5.2.2. As time evolves a greater fraction of debris resides outside of the Earth-Moon system defined as the region within 1.5μ of the barycenter. The fraction of debris impacting the Moon over the course of the simulation only slightly increases after the first 2 periods. The largest fraction of debris near NRHO defined to be within 10,000 km of the reference orbit, is within the first 2 periods of the simulation. However, at later times, the fraction of debris residing near NRHO goes to 0, meaning all debris have left the vicinity of the reference orbit. Less than 1% of debris enters the GEO region over the entire simulation time. Overall, the dispersion of fragments overtime shifts from regions near the Moon, reference NRHO, or within 1.5μ of the barycenter, to the region outside of 1.5μ of the barycenter.

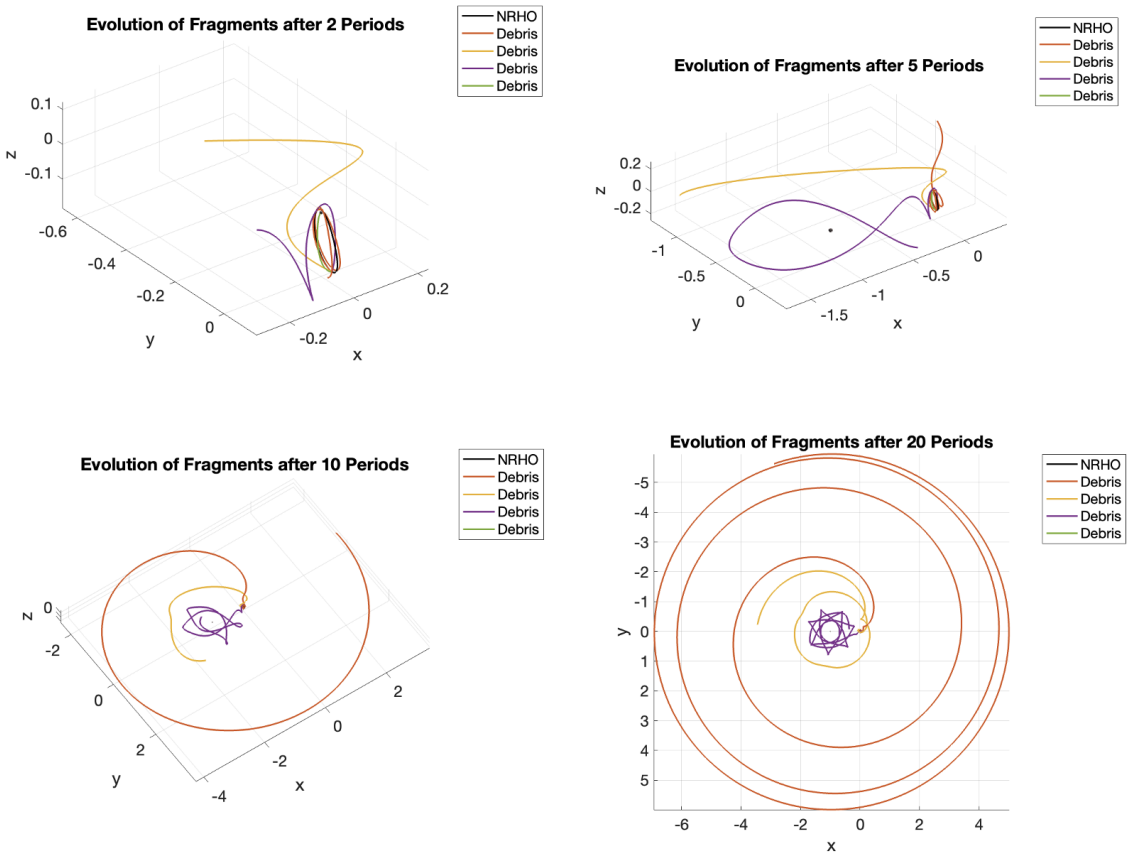

Figure 5-3: Simulated debris fragments for various times since the explosion with Moon positioned at (0,0,0) and the Earth at (-1,0,0).
The distances have been normalized by the distance between the Earth and Moon.

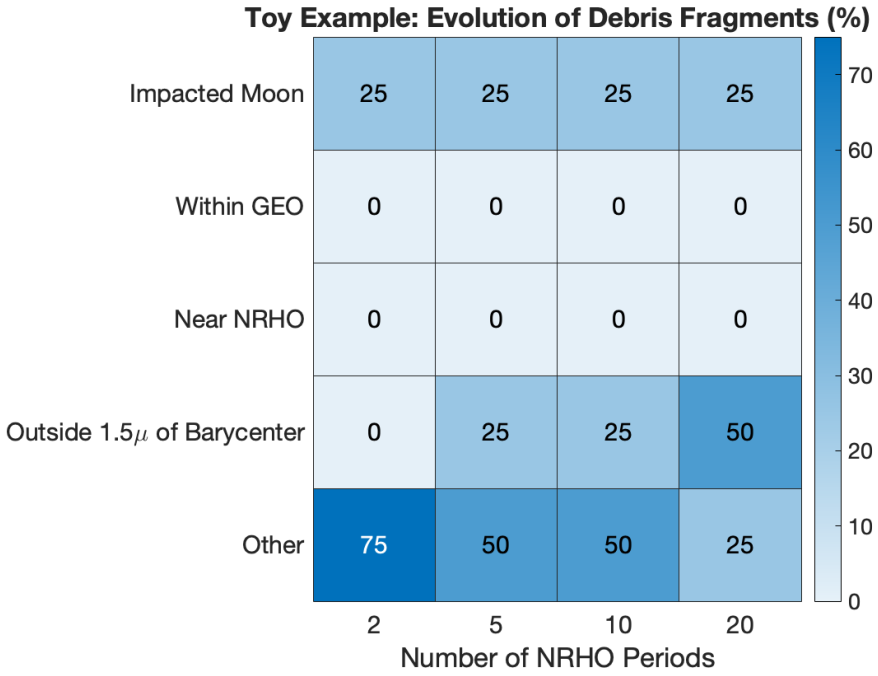

Figure 5-4: A toy example depicting the behavior of 4 debris fragments at different times given as a percent of the total number of fragments that satisfy the categories listed in 5.2.2.

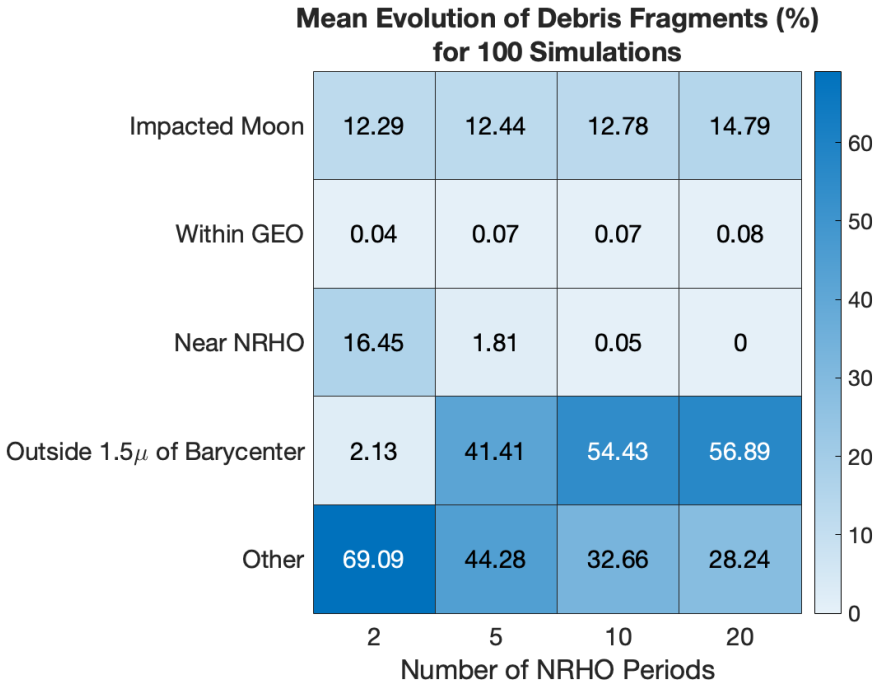

Figure 5-5: The mean behavior of debris fragments for 100 simulations.

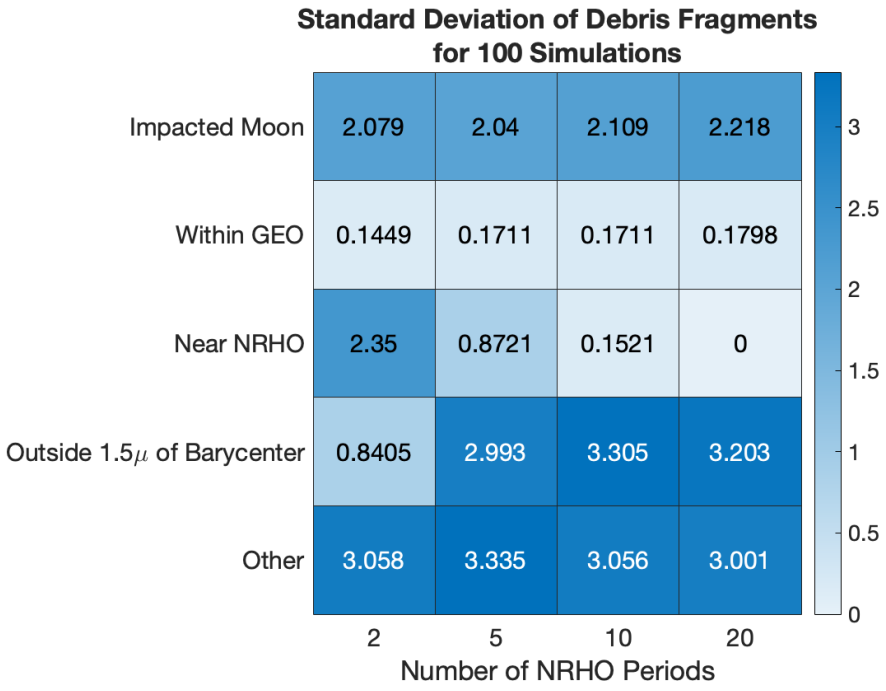

Figure 5-6: The standard deviation of the mean behavior of debris fragments for 100 simulations given in Figure 5-5.

5.4 Threats to Space Missions

From the analysis presented in Section 5.3, the vulnerability of various regions of the Earth-Moon system can be assessed. The risk posed by accidental fragmentation events occurring in an NRHO about the Moon has a very low probability of affecting GEO or altitudes below GEO since less than 1% of fragments enter this region. Thus, the threat to satellite operators in LEO, MEO and GEO is limited. Since a mean of 12.29% of fragments impacts the lunar surface after 2 periods and 14.79% after 20 periods, the threat to lunar missions is high without any mitigation techniques in place. The lunar missions at risk include the planned Artemis Base Camp at the lunar south pole [7] and the lunar orbiters such as the Lunar Reconnaissance Orbiter [6]. For the southern point explosion event considered here, a mean of 29.14 fragments impact the moon within the first 2 NRHO periods, which could potentially present a substantial threat to upcoming missions to the lunar surface. The largest number of lunar impacts occur within 2 periods of the explosion event and then slightly increases

over time, meaning the number of lunar impacts continues to increase for the entire simulation time. Thus, the greatest danger to missions near or on the lunar surface would be closely following the explosion event.

With the highest mean of fragments near NRHO being 16.45% and occurring within 2 periods of the explosion event, the risk to any other mission in NRHO orbit, or the risk to the other modules of Gateway, is highest immediately following the explosion event. The 'other' category encompasses any region within 1.5μ of the barycenter that is outside of GEO and outside the NRHO region. This region is vast and contains various space missions on individual trajectories which makes it difficult to assess the mean risk. However, since a large fraction of debris remain in this region even after 20 periods, the risk is non-negligible and would need a case by case analysis for close encounters with other missions in the Earth-Moon system that reside within 1.5μ of the barycenter. Overall, the analysis above was conducted for fragmentation events occurring at the southern point of the NRHO. The analysis could be extended to include explosion events occurring at other points on or near the NRHO to see where explosions pose the greatest threat to space missions. As only explosion events have been analyzed, the analysis could also be extended to include collision events. A thorough analysis of the behavior of debris for longer simulation times calls for an N-body simulator that accounts for the Sun-Earth-Moon system where the trajectories of the fragments can be analyzed beyond the Earth-Moon sphere of influence. In general, the analysis of fragmentation events in cis-lunar space allows for a greater understanding of the threats such events pose to cis-lunar missions.

Chapter 6

Conclusions and Future Work

This thesis conducted a space debris analysis of the effects of launch activities and fragmentation events in LEO, with a case study of fragmentation events in cis-lunar space. Both LEO and cis-lunar space will see an unprecedented number of launches in the coming years due to the advent of mega-constellations in LEO and the return missions to the Moon. This thesis gave an analysis of the changes in the debris population and its effects in LEO and cis-lunar space.

6.1 Main Findings

6.1.1 Findings from the Dynamical Systems Analysis of LEO

Through the study of various launch rate distributions using a source-sink evolutionary model, the stability of the LEO environment was assessed. Equilibrium solutions were found for 3 launch cases, however, the amounts of debris at equilibrium were much higher for the extrapolated launch rate found using ITU filings as compared to the historical launch rate. All launch traffic was found to lead to an increased density of debris objects even if the assumed probability of successful PMD of 95% is upheld by satellite operators. The evolution of LEO was studied per altitude shell and an accumulation of debris fragments was found to occur at altitudes above 600 km where atmospheric drag is reduced. It was discovered that the much higher launch

rate predicted at lower altitudes below 600 km did not lead to a higher debris population because of the sink of atmospheric drag. The basin of attraction about the equilibrium points was found to assess the maximum perturbation in the debris population allowed before Kessler syndrome was triggered. This maximum perturbation was found per altitude shell and for the entire 200-1000 km region of LEO. Lower altitude shells could accommodate larger perturbations in debris and thus had a higher debris capacity than higher altitude shells. Overall, the dynamical systems analysis of LEO using the MOCAT source-sink model gave insight into the stability of the LEO environment for various possible launch cases.

6.1.2 Findings from the Validation Analysis of the Source-Sink Model

A data analysis of current objects in LEO was conducted and the species characteristics were updated to better reflect the 2022 population of resonant space objects. The explosion rate per species was calibrated using historical fragmentation data of accidental explosions. No correlation with altitude was found for historic explosion events. The NASA Standard Breakup model's parameters were also calibrated using the fragmentation data analysis and the characteristic parameter used in the breakup model was determined for each species. Derelict satellites were found to produce the most fragments per explosion whereas rocket bodies were found to have the highest explosion rate per year. A PMD model for rocket bodies was implemented and the PMD model for active satellites was changed to lower species members to an altitude at which the object will de-orbit under atmospheric drag within the specified desired PMD duration. The dispersion of fragments following an explosion event was analyzed in the context of the shell assumption used in the source-sink models. The analysis showed that less than 50% of fragments remained in the shell of the original explosion 10 days after the event, showing the limitation of using shells in the model. Finally, 200-year-long simulations were run using the MOCAT source-sink model with and without the new improvements and compared to simulations

run on ESA's DELTA model. Overall, the MOCAT model showed a greater convergence with DELTA's predictions of the future orbital environment with improvements rather than without.

6.1.3 Findings from the Case Study of Fragmentation Events in Cis-Lunar Space.

The case study analysis of an explosion event along the lunar Gateway's orbit showed that the debris produced poses a risk to all regions of the Earth-Moon system. The lowest risk is posed to Earth-orbiting satellites at altitudes of GEO or below with less than 1% of fragments reaching this region in a 130-day-long simulation. The highest risk to lunar missions was found to be immediately following the event. The dispersion of fragments caused all fragments to leave the vicinity of the NRHO orbit within the 130-day-long simulation time. However, approximately 28% of fragments remained within 1.5 Earth-Moon distances of the barycenter of the Earth-Moon system at the end of the simulation time, signifying they pose a threat to space missions occupying cis-lunar space.

6.2 Future Work

Drawing from the findings made in this thesis, several potential directions of future research are identified:

- The fidelity in launch predictions made from ITU filings and other databases could be verified using historical launch data and comparing it with historical filings.

- The sensitivity to the use of shells in the source-sink model could be explored further to see the effect of the chosen number of shells, the shell width, and the shell edge placement as well as the effect of further discretizing the shells by inclination.

- A sensitivity to the number of species used to represent the reference population could be done to find the most accurate way of representing the orbital population by species categories.
- Further validation work could be done to align the source-sink model's predictions with predictions made by higher-fidelity models.
- The cis-lunar debris analysis could be expanded to include collision events and interactions between various cis-lunar missions beyond the NRHO case study done in this thesis.
- The analysis of debris trajectories in cis-lunar space could be expanded to include chaotic indicators that depict the stable and unstable regions in the Earth-Moon system.

Bibliography

[1] IADC Working Group 4. Support to the IADC space debris mitigation guidelines. *Inter-Agency Space Debris Coordination Committee*, Jun 2021.

[2] Liliia Alaieva. Starlink Performed 26 Thousand Avoidance Maneuvers in Two Years. *The Universe magazine Space Tech*, Jan 2023.

[3] Daria Andrievskaia, Ignacio Cáceres, Paolo Guardabasso, and Stéphanie Lizy-Destrez. Analysis of Lunar Impacts for Orbital Debris Mitigation. In *73rd International Astronautical Congress*, Sep 2022.

[4] Phillip Anz-Meador. Top Ten Satellite Breakups Reevaluated. *Orbital Debris Quarterly News, National Aeronautics and Space Administration*, 20(1), Apr 2016.

[5] Nathan R. Boone and Robert A. Bettinger. Debris Collision Risk Analysis Following Simulated Cislunar Spacecraft Explosions. *Journal of Spacecraft and Rockets*, 60(2):668–684, 2023.

[6] Gordon Chin, Scott Brylow, Marc Foote, James Garvin, Justin Kasper, John Keller, Maxim Litvak, Igor Mitrofanov, David Paige, Keith Raney, et al. Lunar Reconnaissance Orbiter Overview: Theá Instrument Suite and Mission. *Space Science Reviews*, 129:391–419, 2007.

[7] Steve Creech, John Guidi, and Darcy Elburn. Artemis: An Overview of NASA's Activities to Return Humans to the Moon. In *2022 IEEE Aerospace Conference (AERO)*, pages 1–7, 2022.

[8] Marius Crisan. Convergence Towards a Dynamic Theory of Linguistics and Semantics. In Marius Crisan, editor, *Convergence and Hybrid Information Technologies*, chapter 3. IntechOpen, Rijeka, 2010.

[9] Jason C. Crusan, R. Marshall Smith, Douglas A. Craig, Jose M. Caram, John Guidi, Michele Gates, Jonathan M. Krezel, and Nicole B. Herrmann. Deep space gateway concept: Extending human presence into cislunar space. In *2018 IEEE Aerospace Conference*, pages 1–10, 2018.

[10] Andrea D'Ambrosio, Miles Lifson, Daniel Jang, Celina Pasiecznik, and Richard Linares. Projected Orbital Demand and LEO Environmental Capacity. In *23rd*

Advanced Maui Optical and Space Surveillance Technologies, Maui, HI, 2022. Maui Economic Development Board.

[11] Andrea D'Ambrosio, Miles Lifson, and Richard Linares. The Capacity of Low Earth Orbit Computed using Source-sink Modeling, 2022.

[12] Christian Davenport. Thousands More Satellites Could Soon be Launched into Space. Can the Federal Government Keep Up? *The Washington Post*, Jul 2020.

[13] Leonard David. Effects of Worst Satellite Breakups in History Still Felt Today. *Space.com*, Jan 2013.

[14] Jakub Drmola and Tomas Hubik. Kessler syndrome: System dynamics model. *Space Policy*, 44-45:29–39, 2018.

[15] Andrea D'Ambrosio, Simone Servadio, Peng Mun Siew, and Richard Linares. Novel Source–Sink Model for Space Environment Evolution with Orbit Capacity Assessment. *Journal of Spacecraft and Rockets*, 0(0):1–15, 0.

[16] NASA Engineering and Safety Center. Annual Summary of 2022 Technical Activities, May 2022.

[17] ESA Space Debris Office. ESA's Space Environment Report 2022. Technical report, European Space Agency, 2022.

[18] United Nations Office for Outer Space Affairs. The History of Space Debris Creation. *ESA Space Safety*, Dec 2020.

[19] Carolin Frueh, Kathleen Howell, Kyle J. DeMars, and Surabhi Bhadauria. Cislunar Space Situational Awareness. In *31st AAS/AIAA Spaceflight Mechanics Meeting*, Charlotte, North Carolina (Virtual), 2021. AAS/AIAA.

[20] Sean Fuller, Emma Lehnhardt, Christina Zaid, and Kate Halloran. Gateway Program Status and Overview. *Journal of Space Safety Engineering*, 9(4):625–628, 2022.

[21] Paolo Guardabasso, Francesca Letizia, and Stéphanie Lizy-Destrez. Development of a Framework for Space Debris Mitigation in the Cislunar Space. In *44th COSPAR Scientific Assembly. Held 16-24 July*, volume 44, page 3169, July 2022.

[22] Paolo Guardabasso and Stéphanie Lizy-Destrez. Lunar Orbital Debris Mitigation: Characterisation of the Environment and Identification of Disposal Strategies. In *8th European Conference on Space Debris (Virtual)*, Apr 2021.

[23] Paolo Guardabasso, Despoina Skoulidou, Lorenzo Bucci, Francesca Letizia, and Stéphanie Lizy-Destrez. Cislunar Debris Mitigation: Development of a Methodology to Assess the Sustainability of Lunar Missions. In *72nd International Astronautical Congress (IAC)*, Oct 2021.

[24] Paolo Guardabasso, Despoina K. Skoulidou, Lorenzo Bucci, Francesca Letizia, Stijn Lemmens, Marie Ansart, Xavier Roser, Stéphanie Lizy-Destrez, and Grégoire Casalis. Analysis of Accidental Spacecraft Break-up Events in Cislunar Space. *Advances in Space Research*, 2023.

[25] Davide Gusmini, Andrea D Ambrosio, Simone Servadio, Pierluigi Di Lizia, and Richard Linares. The Effects of Orbit Raising and Decay in Orbital Capacity Models. In *33rd AAS/AIAA Space Flight Mechanics Meeting*, Austin, TX, 2023. AAS/AIAA.

[26] André Horstmann, Sebastian Hesselbach, and Carsten Wiedemann. *Enhancement of S/C Fragmentation and Environment Evolution Models*. Technische Universität Braunschweig Institute of Space Systems, Aug 2020.

[27] Daniel Jang, Andrea D'Ambrosio, Miles Lifson, Celina Pasiecznik, and Richard Linares. Stability of the LEO Environment as a Dynamical System. In *23rd Advanced Maui Optical and Space Surveillance Technologies*, Maui, HI, 2022. Maui Economic Development Board.

[28] Daniel Jang, Davide Gusmini, Peng Mun Siew, Andrea D'Ambrosio, Simone Servadio, Pablo Machuca, and Richard Linares. Monte Carlo Methods to Model the Evolution of the Low Earth Orbit Population. In *33rd AAS/AIAA Space Flight Mechanics Meeting*, Austin, TX, 01 2023. AAS/AIAA.

[29] Alan B. Jenkin, Marlon E. Sorge, Glenn E. Peterson, John P. McVey, and Bernard Y. Yoo. 100-Year Low Earth Orbit Debris Population Model. In *Astrodynamics Specialists Conference*, Girdwood, AK, 2011. AAS/AIAA.

[30] Nicholas L. Johnson, Paula Krisko, J.-C Liou, and Phillip Anz-Meador. NASA's new breakup model of evolve 4.0. *Advances in Space Research*, 28:1377–1384, 12 2001.

[31] Sandra K. Johnson, Dale J. Mortensen, Mark Andrew A. Chavez, and Chris Woodland. Gateway – a communications platform for lunar exploration. *38th International Communications Satellite Systems Conference (ICSSC 2021)*, 2021:9–16, 2021.

[32] Christopher Kebschull, Philipp Scheidemann, Sebastian Hesselbach, Jonas Radtke, Vitali Braun, H. Krag, and Enrico Stoll. Simulation of the Space Debris Environment in LEO Using a Simplified Approach. *Advances in Space Research*, 59(1):166–180, 2017.

[33] T.S. Kelso. Iridium 33/Cosmos 2251 Collision. *CelesTrak*, Jun 2012.

[34] Donald J Kessler and Burton G Cour-Palais. Collision Frequency of Artificial Satellites: The Creation of a Debris Belt. *Journal of Geophysical Research: Space Physics*, 83(A6):2637–2646, 1978.

[35] Heiner Klinkrad. *Space Debris: Models and Risk Analysis*. Springer, 01 2006.

[36] Herbert J. Kramer. Lunar Gateway of NASA's Artemis Program. *eoPortal*, Jul 2019.

[37] Paula H. Krisko. Proper Implementation of the 1998 NASA Breakup Model. *Orbital Debris Quarterly News*, 15(4):1–10, 2011.

[38] Hugh G. Lewis, Graham G. Swinerd, Rebecca J. Newland, and Arrun Saunders. The Fast Debris Evolution Model. *Advances in Space Research*, 44:568–578, 9 2009.

[39] Hugh G. Lewis, Adam E. White, Richard Crowther, and Hedley Stokes. Synergy of Debris Mitigation and Removal. *Acta Astronautica*, 81(1):62–68, 2012.

[40] Sophie Lewis. Space Junk Slams into International Space Station, Leaving Hole in Robotic Arm. *CBS News*, Jun 2021.

[41] Miles Lifson, Andrea D'Ambrosio, David Arnas, and Richard Linares. How many satellites can we fit in low earth orbit?: Capacity integrating risk-based and intrinsic methods. *Astrodynamics Specialist Conference*, Preprint.

[42] J.-C. Liou. Satellite Collision Leaves Significant Debris Clouds. *Orbital Debris Quarterly News, National Aeronautics and Space Administration*, 13(2), Apr 2009.

[43] J.-C. Liou. An Updated Assessment of the Orbital Debris Environment in LEO. *Orbital Debris Quarterly News, National Aeronautics and Space Administration*, 14(1&2), Jan 2010.

[44] J.-C Liou, D.T Hall, P.H Krisko, and J.N Opiela. LEGEND – a Three-Dimensional LEO-to-GEO Debris Evolutionary Model. *Advances in Space Research*, 34(5):981–986, 2004. Space Debris.

[45] J.-C Liou and Nicholas Johnson. A LEO Satellite Postmission Disposal Study Using LEGEND. *Acta Astronautica*, 57:324–329, 07 2005.

[46] ITU e-Submission of Satellite Network Filings 'As Received'. https://www.itu.int/ITU-R/space/asreceived/Publication/AsReceived.

[47] National Aeronautics and Space Administration. *NASA's Journey to Mars: Pioneering Next Steps in Space Exploration*. Government Printing Office, 2016.

[48] Celina Pasiecznik, Andrea D'Ambrosio, Daniel Jang, and Richard Linares. A Dynamical Systems Analysis of the Effects of the Launch Rate Distribution on the Stability of a Source-Sink Orbital Debris Model. In *73rd International Astronautical Congress*, Sep 2022.

[49] Orbital Debris Research and Development Interagency Working Group. *National Orbital Debris Research and Development Plan*. National Science and Technology Council (NSTC), Jan 2021.

[50] Rosa. Satellite Studying Earth's Diminishing Ice Swerves to Avoid Collision. *European Space Agency*, Jul 2018.

[51] Shane Ross, Wang Koon, Martin Lo, and Jerrold Marsden. *Dynamical Systems, the Three-Body Problem, and Space Mission Design*. Marsden Books, 10 2022.

[52] Alessandro Rossi, Elisa Maria Alessi, Giovanni Valsecchi, Hugh G. Lewis, Jonas Radtke, Claudio Bombardelli, and Benjamin Virgili. A Quantitative Evaluation of the Environmental Impact of the Mega Constellations. In *7th European Conference on Space Debris*, 04 2017.

[53] Alessandro Rossi, Alessandro Cordelli, Paolo Farinella, and Luciano Anselmo. Collisional Evolution of the Earth's Orbital Debris Cloud. *Journal of Geophysical Research: Planets*, 99(E11):23195–23210, 1994.

[54] Ian Sample. Mind That Satellite! The Mission to Clean up Dangerous Space Junk. *The Guardian*, Apr 2022.

[55] Gian Luigi Somma. *Adaptive Remediation of the Space Debris Environment Using Feedback Control*. PhD thesis, University of Southampton, 2019.

[56] Thales Alenia Space. ESPRIT Refueling Module. *ESA Human Spaceflight*, Sep 2022.

[57] David L. Talent. Analytic Model for Orbital Debris Environmental Management. *Journal of Spacecraft and Rockets*, 29(4):508–513, 1992.

[58] Valeria Trozzi, Mirko Trisolini, and Camilla Colombo. Analysis of Possible Definitions of the Space Environment Capacity to Pursue Long-Term Sustainability of Space Activities. In *72nd International Astronautical Congress*, 10 2021.

[59] UCS-Satellite-Database-5-1-2022. http://www.ucsusa.org/satellite_database.

[60] Benjamin Bastida Virgili. DELTA Debris Environment Long-Term Analysis. In *Proceedings of the 6th International Conference on Astrodynamics Tools and Techniques (ICATT)*, 2016.

[61] Roger Walker, C.E. Martin, Hedley Stokes, Jenny E. Wilkinson, and Heiner Klinkrad. Analysis of the Effectiveness of Space Debris Mitigation Measures Using the Delta Model. *Advances in Space Research*, 28(9):1437–1445, 2001.

[62] Brian Weeden. 2007 Chinese Anti Satellite Test Fact Sheet . *Secure World Foundation*, Nov 2010.

[63] James R. Wertz, David F. Everett, and Jeffery J. Puschell. *Space Mission Engineering : the New SMAD*. Space technology library ; v. 28. Microcosm Press, Hawthorne, Calif, 2011.

[64] Ryan J. Whitley, Diane C. Davis, Laura M. Burke, Brian P. McCarthy, Rolfe, John A. Power, Melissa L. Mcguire, and Kathleen C. Howell. Earth-Moon Near Rectilinear Halo and Butterfly Orbits for Lunar Surface Exploration. AAS/AIAA, 2018.

[65] Binbin Zhang, Zhaokui Wang, and Yulin Zhang. Discrete Evolution Model Based on Mean Spatial Density for Space Debris Environment. *Astrophysics and Space Science*, 364, 04 2019.